



Universiteit
Leiden
The Netherlands

Elasticity and plasticity : foams near jamming

Siemens, A.O.N.

Citation

Siemens, A. O. N. (2013, September 12). *Elasticity and plasticity : foams near jamming*. *Casimir PhD Series*. Retrieved from <https://hdl.handle.net/1887/21709>

Version: Not Applicable (or Unknown)

License: [Leiden University Non-exclusive license](#)

Downloaded from: <https://hdl.handle.net/1887/21709>

Note: To cite this publication please use the final published version (if applicable).

Cover Page



Universiteit Leiden



The handle <http://hdl.handle.net/1887/21709> holds various files of this Leiden University dissertation.

Author: Siemens, Alexander Oltmann Nicolaas

Title: Elasticity and plasticity : foams near jamming

Issue Date: 2013-09-12

Alexander O. N. Siemens

Elasticity and Plasticity:
Foams near Jamming

Copyright © Alexander O. N. Siemens

Cover design: my foray in IDL... Alexander O. N. Siemens

Printed by Gildeprint, The Netherlands

Elasticity and Plasticity: Foams near Jamming

PROEFSCHRIFT

ter verkrijging van
de graad van Doctor aan de Universiteit Leiden,
op gezag van Rector Magnificus
Prof. mr. C.J.J.M. Stolker,
volgens besluit van het College voor Promoties
te verdedigen op donderdag 12 september 2013
klokke 15:00 uur

door

Alexander O. N. Siemens
geboren te Washington D.C., Verenigde Staten van
Amerika
in 1985

Promotiecommissie:

Promotor: Prof. dr. M.L. van Hecke
Overige leden: Dr. E.I. Corwin (*University of Oregon, Eugene, USA*)
Dr. B.P. Tighe (*Technische Universiteit Delft*)
Prof. dr. E.R. Eliel
Prof. dr. ir. T.H. Oosterkamp

Casimir PhD Series, Delft-Leiden, 2013-21
ISBN 978-90-8593-162-1

Dit werk maakt deel uit van het onderzoeksprogramma van de Stichting voor Fundamenteel Onderzoek der Materie (FOM), welke financieel wordt gesteund door de Nederlandse Organisatie voor Wetenschappelijk Onderzoek (NWO).

An electronic version of this dissertation is available at the Leiden University Repository (<http://openaccess.leidenuniv.nl>).

“For all that has been – Thanks.
For all that shall be – Yes.”

Dag Hammarskjöld

To my family and friends

Contents

1	Motivation: Jamming of 2D Foams	1
2	Introduction	5
2.1	Jamming in a Simple Model	7
2.1.1	Model	7
2.1.2	The Jamming Point	8
2.2	Jammed Materials are Not Ordinary Solids	10
2.2.1	Contact Number	11
2.2.2	Elastic Moduli	13
2.2.2.1	Compression Modulus	14
2.2.2.2	Shear Modulus	15
2.3	Beyond Effective Medium Theory	16
2.3.1	Nonaffine Deformations	16
2.4	Experimental Review	18
3	2D Foams in a Wedge Geometry: Set-up	21
3.1	Experimental Set-up	22
3.1.1	Set-up	24
3.1.2	Foam	27
3.1.3	Temperature Control	30
3.1.4	Imaging	34
3.2	Leveling	37
3.2.1	Protocol to Level	40
3.2.2	Equilibrium Coordinates	44
3.3	Compression Protocols	46
3.3.1	Deflection Angle vs. Open Angle	46
3.3.2	Dynamics of Different Protocols	47

3.3.3	Stress vs Strain Control	48
3.3.4	Protocols	49
3.3.4.1	Flat Protocol	49
3.3.4.2	Corner Hole Protocol	51
3.3.4.3	Slice Hole Protocol	52
4	Jamming of a 2D Foam	53
4.1	Elastic Response in a Wedge	55
4.2	From Gravity to Boundary Jammed States	58
4.2.1	Determining $T(\tau_2)$	58
4.2.2	Determining the Foam Area	62
4.3	Results	63
4.3.1	Using A_F as Control Parameter	65
4.3.2	$G + K$: A Comparison	69
4.3.3	Residual Torque	71
4.3.4	High Tilt Compressions	73
4.4	Nonaffinity Near Jamming	76
4.4.1	Nonaffine Deformation	77
4.4.2	Variance in Compression Runs	80
4.4.3	Foam Motion Signal	81
4.4.4	Comparing Torque and Variance Signals	85
5	Rearrangement of Foams	87
5.1	Previous Work	89
5.2	Biaxial Set-up	90
5.2.1	Set-up	92
5.2.2	Shear and Strain	96
5.2.3	Protocols	99
5.2.3.1	Continuous Shear Protocol	101
5.2.3.2	Start/Stop Protocol	101
5.2.4	Affine Deformation and Variance	102
5.2.5	Stick-slip in the Set-up	104
5.3	Results	107
5.3.1	Continuous Shear	107
5.3.2	Start/stop Shear	113
5.4	Conclusions and Outlook	115
	Summary	117
	Samenvatting	121

Publication List	125
Curriculum Vitae	127
Acknowledgments	129
Bibliography	131

Motivation: Jamming of 2D Foams

Jamming aims to describe the transition from freely flowing to rigid phases of a wide range of soft materials including foams, emulsions, suspensions and granular media [1, 2]. Over the last decade, a surge of interest in jamming has led to much progress on the theoretical understanding of the jamming transition, with a strong focus on numerical simulations [1]. While various models have been studied in simulations, most work has focused on a simple model of soft, frictionless spheres, which is thought to be a good model for foams and emulsions.

The details of the jamming scenario for these models will be reviewed in Chapter 2. For foams (and emulsions), the essence of the jamming scenario is as follows. The crucial parameter is the packing density, which for foams is measured by its gas fraction, the amount of volume taken up by the bubbles in their bounded area. Foams close to the jamming point have a low gas fraction and are said to be “wet”, whereas foams that are compressed are “dry”, due to a larger gas fraction in this regime. In simulations, the jamming point corresponds to the packing density at which all bubbles/particles in the packing come into contact with one another. Below this critical point, the packing is loose, with no bubbles in contact. Above the critical point the bubbles, due to their soft characteristics, are deformed. A major goal of this thesis is to probe how this scenario plays out in realistic foams.

Experimentally, foams can be studied in two different settings: in 3D and in 2D. In 3D, foams are opaque and moreover, suffer from drainage, the effect that gravity sucks the fluid out of the top layers of the foam, making it hard to maintain 3D wet foams stable in a gravitational field (recently

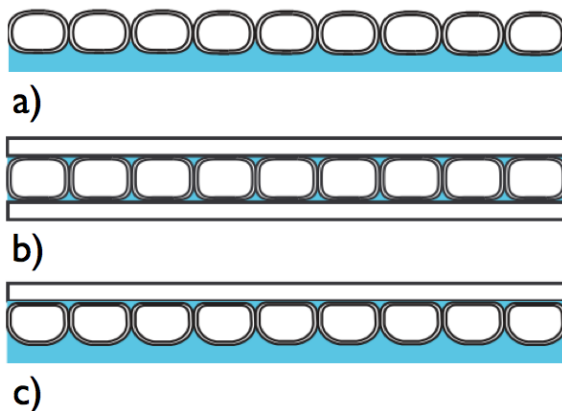


Figure 1.1 – Different bubble geometries used in two-dimensional rheology experiments: a) bubble raft, b) Hele-Shaw, c) bubble monolayer trapped between liquid surface and glass plate. Images courtesy of [6].

Isert et al. [3] managed to keep a 3D foam stable without drainage in a strong magnetic field). 2D foams do not suffer from such problems: they can be imaged easily and their packing fraction can be controlled well; in particular they can be taken close to jamming [4, 5].

These foams, monolayers of bubbles, are relatively easy to work with and recent experiments have used many different geometries, like bubble rafts [7] (no top plate bounding the packing from above, see Fig. 1.1 a)) and Hele-Shaw [8] (bubbles trapped between two glass plates, see Fig. 1.1 b)), as well as bubbles floating on a soap solution bounded from above by a glass plate [4, 5, 9, 10], see Fig. 1.1 c). This latter geometry will be used throughout this Thesis. In this configuration, the bubbles experience no appreciable attraction and interact through repulsive contact forces. There is no static friction in the system, and to avoid crystallization we use bidisperse bubbles.

In this Thesis, we probe two aspects of the mechanics of foams near the jamming transition. In Chapter 2, we introduce the concept of jamming and briefly review recent work on foams. In Chapters 3 and 4 we probe the elasticity response of foams near the jamming transition. We find that the presence of a weak symmetry breaking field, due to the residual gravity, alters the jamming scenario in an important manner; it prevents us from reaching a fully jammed state. Nevertheless, we are able to establish that near jamming, the bulk modulus is much larger than the shear modulus, which is one of the most striking theoretical predictions. In Chapter 5 we probe the plastic response of foams by submitting them to large shear

deformations. We recover that the well-known plastic “T1” events dominate plastic response far away from jamming. However, closer to jamming, these T1 events give way to less strongly localized rearrangements that have not been discussed in literature, suggesting that plasticity near jamming is governed by qualitatively different and new physics.

Introduction

Many everyday materials such as sand, toothpaste, mayonnaise and shaving foam exhibit an intriguing mix of liquid-like and solid-like behaviors, some familiar, some surprising but often poorly understood. These materials all have in common a consistency of disordered collections of macroscopic constituent particles: sand is a dense packing of solid grains (Fig. 2.1 a)), toothpaste is a dense packing of (colloidal) particles in fluid (Fig. 2.1 b)), mayonnaise is an emulsion consisting of a dense packing of (oil) droplets in an immiscible fluid (Fig. 2.1 c)), and shaving foam is a dense packing of gas bubbles in fluid (Fig. 2.1 d)).

Dense is the keyword here – these materials obtain finite rigidity once their constituent particles are brought into contact. Nevertheless, all these materials can be made to flow by the application of relatively small stresses – in fact their utility often stems from precisely this combination of liquid-like and solid-like behavior. By varying thermodynamic (temperature or density) and mechanical (applied stress) variables, one can bring about a transition from a freely flowing to a *jammed* state in these and many other disordered media. For instance an increase in density causes colloidal suspensions to turn glassy. Similarly, flowing foams can be made static by decreasing the applied stress to below the yield stress. In 1998, Liu and Nagel presented a novel way of organizing the physics underlying these phenomena through a jamming diagram (Fig. 2.1e)), and proposed to probe various transitions to rigidity [1].

This Chapter aims at giving a basic introduction to our current understanding of the following two questions: What is the nature of the jammed state? And what is the nature of the jamming transition? We will illustrate the main features of these systems by idealized pictures illustrating our current understanding rather than “real” experimental and numerical

data. For a more elaborate introduction, the reader is referred to two more detailed review papers and references therein [11, 12].

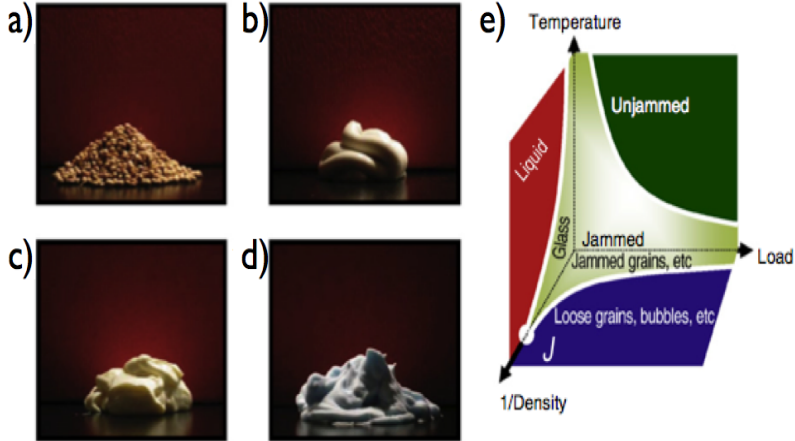


Figure 2.1 – (a-d) Examples of everyday disordered media in a jammed state. a) Granular media. b) Toothpaste. c) Mayonnaise. d) Shaving foam. e) Jamming diagram as proposed by Liu, Nagel and coworkers [1, 13]. The diagram illustrates that many disordered materials are in a jammed state at low temperature, low load and large density, but can yield and become unjammed when these parameters are varied. In this Chapter we will focus on the zero temperature, zero load axis. For frictionless soft spheres, there is a well-defined jamming transition indicated by point “J” on the inverse density axis, which exhibits similarities to an (unusual) critical phase transition.

We will deal only with zero temperature packings of frictionless soft spheres that interact through purely repulsive contact forces. “Soft” in this case means that the individual particles can be deformed under relevant loads – deformations are key. We review the geometrical and mechanical properties of these systems as a function of the distance to jamming.

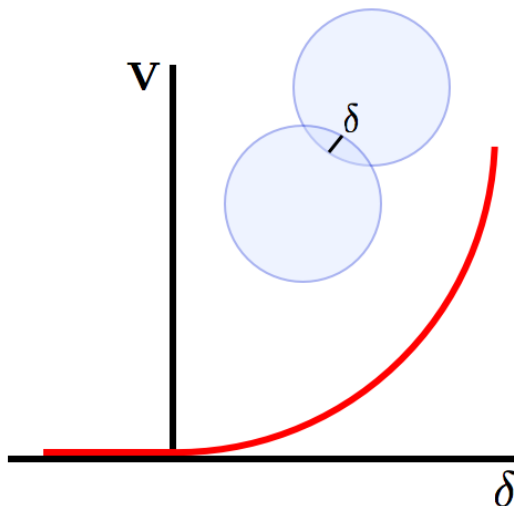


Figure 2.2 – The interaction potential V for pairs of interacting soft frictionless spheres is a simple function of the particles overlap, δ , only.

2.1 Jamming in a Simple Model

Over the last decade, tremendous progress has been made in our understanding of what might be considered the “Ising model” for jamming: static packings of soft, frictionless spheres that act through purely repulsive contact forces. The beauty of such systems is that they allow for a precise study of a jamming transition. In this section we introduce this model, discuss some aspects of its jamming transition and discuss its main parameters.

2.1.1 Model

The most studied and best understood model for jamming consists of soft spherical particles that only interact when in contact, with the interaction forces set by the amount of virtual overlap (similar to deformations for real particles or bubbles) between two particles in contact. Moreover, the contact forces are purely repulsive. No frictional forces, and no attraction is included.

Denoting the undeformed radii of particles in contact as R_i and R_j and the center-to-center distance as r_{ij} , it is convenient to define a dimensionless overlap parameter δ_{ij} as

$$\delta_{ij} := 1 - \frac{r_{ij}}{R_i + R_j}, \quad (2.1)$$

so that particles are in contact only if $\delta_{ij} \geq 0$. Since we only will study static properties here, there is no need for specifying a dissipative mechanism.

Power law interaction potentials take on the form (see Fig. 2):

$$\begin{aligned} V_{ij} &= \delta_{ij}^\alpha & \delta_{ij} &\geq 0, \\ V_{ij} &= 0 & \delta_{ij} &\leq 0. \end{aligned} \quad (2.2)$$

For harmonic interactions, $\alpha = 2$, while Hertzian interactions (the non-linear contact laws for elastic spheres in 3D) correspond to $\alpha = 5/2$. By varying the exponent α the nature and robustness of various scaling laws can be probed.

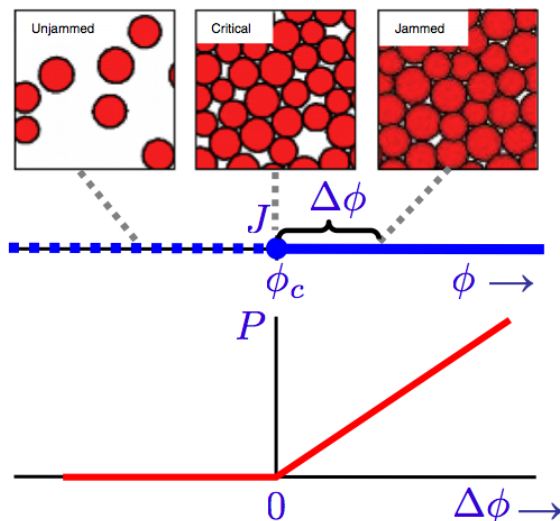


Figure 2.3 – Top: examples of repulsive soft particles below, at and above the jamming transition. The jamming point for frictionless soft spheres is referred to as point J . The packing density ϕ controls the transition here, and the jamming transition occurs at the critical value ϕ_c . The distance to jamming is given by the excess density $\Delta\phi$. Bottom: when the particles have simple harmonic interactions (when they overlap), the pressure grows linearly with excess density.

2.1.2 The Jamming Point

What is the jamming transition for this simple system? The main features are illustrated in Fig. 2.3. As the packing density of the particles, ϕ , is increased, the jamming transition occurs when essentially all particles start to touch but still are at zero pressure – this is called *point J*. Here ϕ_c , the critical packing fraction, is the point at which the particles start touching.

The distance to the jamming point can be measured as $\Delta\phi = \phi - \phi_c$, see Fig. 2.3 [13].

An alternative measure of the distance to jamming is the pressure in the system. If the particles are not in contact, the contact forces between the particles are zero, and so is the pressure. Once particles start to overlap, contact forces arise, and the pressure becomes non-zero, see Fig. 2.3. In fact, one can show that the pressure and the contact forces scale similarly – $P \sim \langle f \rangle$, where brackets denote the average over the system. For the simple interactions used here, and in the absence of gravity, there cannot be a finite force in part of the system, while other parts of the system are at zero pressure. Hence, for finite pressure, the vast majority of particles experience finite contact forces (typically a few percent of the particles are *rattlers*, particles that have only zero contact forces).

Once the pressure is non-zero, the system is jammed. With this we mean that, first, the system has finite elastic moduli, so that applying infinitesimally small forces to the system leads to a proportional and reversible deformation. Second, the system has a finite yielding threshold: if we force the system so much that irreversible deformations arise, the amount of force is *finite* [13].

There are two important things to note: First, for finite systems, the jamming density ϕ_c varies between realizations – this is why one measures the distance to jamming by $\Delta\phi$ and not with ϕ . A disadvantage of using the excess density is that one must first obtain a value for ϕ_c . For simulations this can be done by starting with a jammed system and deflating the particles until the system is not rigid anymore [13]. This step is not necessary when the pressure is a control parameter, since at point J, $P = 0$.

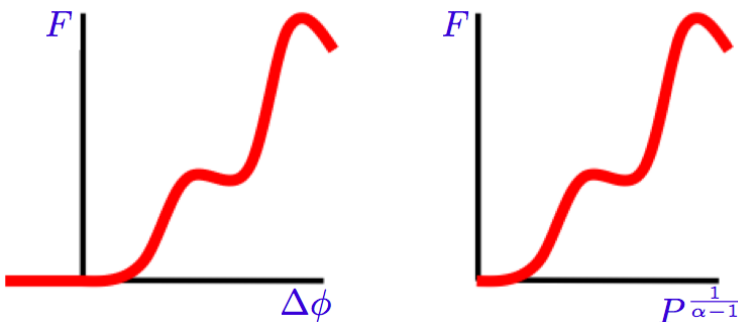


Figure 2.4 – Any function F of the excess packing density $\Delta\phi$ can be translated to a function of the pressure P – for power law interactions of the form Eq. 2.2, $P \sim (\Delta\phi)^{\alpha-1}$.

To relate $\Delta\phi$ and P , we note that the typical particle overlap δ scales as $\Delta\phi$. To relate the pressure and the typical particle overlap, we note that $P \sim f$, and that the force is just $f = -\nabla V_{ij}$. For power law interactions of the form Eq. 2.2 the potential is a function of the overlap, and hence we can relate $\Delta\phi$ and P as follows:

$$P \sim f = \frac{dV_{ij}}{d\delta} \sim \delta^{\alpha-1} \sim (\Delta\phi)^{\alpha-1}. \quad (2.3)$$

As is illustrated in Fig. 2.4, quantities measured as function of $\Delta\phi$ and as function of P can be directly translated.

Secondly, for infinite systems, ϕ_c tends to a well-defined value, directly related to *Random Close Packing* of hard (undeformed) spheres. Random close packing is a notoriously tricky concept, since it is not always clear what random means. An attempt to model RCP based on experimental systems has only recently found some success [14]. In three dimensions, the densest possible packing is the regular FCC packing (similar to how oranges are packed in your grocery store), which reaches a packing density of 74%. What is now the densest random packing? For example, packings consisting of large FCC clusters that are irregularly stacked can attain densities arbitrarily close to the FCC density but still be called random. However, in the absence of any appreciable order, the densest random packings have $\phi_{RCP} \approx 0.64$ (in three dimensions – in two dimensions $\phi_{RCP} \approx 0.84$). Probing the jamming transition with a specific protocol may be seen as defining the RCP density [13]. It is important to note here that monodisperse systems in 2D tend to crystallize easily. To avoid such crystallization, bidisperse or polydisperse systems are often used [4, 5, 15].

2.2 Jammed Materials are Not Ordinary Solids

Superficially, the jamming transition appears similar to a liquid-solid like transition such as freezing. Is the jammed phase simply a solid? In this section we will show that packings at or near jamming are very different from ordinary, *crystalline* solids. We will focus on the elastic and geometric properties of soft spheres near jamming. To highlight the anomalous behavior of jammed solids, we will first explicitly state what we think the simplest prediction for these properties would be. The simple predictions are essentially based on pictures where one ignores the disorder, so called “effective medium” pictures, which work well for ordered materials. One often assumes deformations of the material to be affine, i.e., the local deformations follow trivially from the global.

But such affine / effective medium predictions fail to describe disordered media, and the failure becomes increasingly pronounced when one approaches the jamming transition. Of course, this approach may appear like setting up a straw man, yet we feel it is a useful strategy to stress a surprising aspect of the jamming transition.

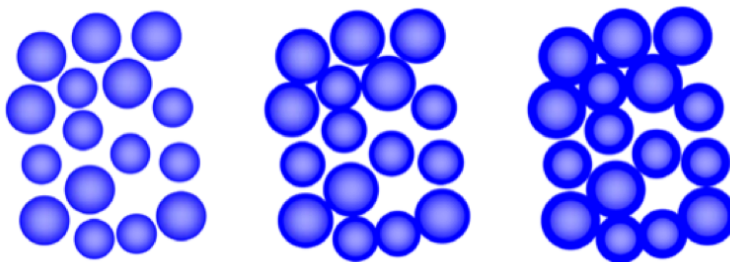


Figure 2.5 – An affine compression of a packing is equivalent to fixing the particles’ positions and then inflating their radii.

2.2.1 Contact Number

A key parameter of a packing is its contact number, z , defined as the average number of contacts per particle. To estimate z as function of packing fraction, we start with a low density situation where no particles touch. The simplest estimate of what happens when we compress such a packing is to assume that the local motion of the particles simply follows the globally applied deformation – for compression this is equivalent to inflating all particle radii while keeping their position fixed (Fig. 2.5). More precisely, this uniform compression is an example of an *affine* deformation. A strict definition of affine transformations states that three collinear particles remain collinear and that the ratio of their distances is preserved, and affine transformations are, apart from rotations and translations, composed of uniform shear and compression or dilatation.

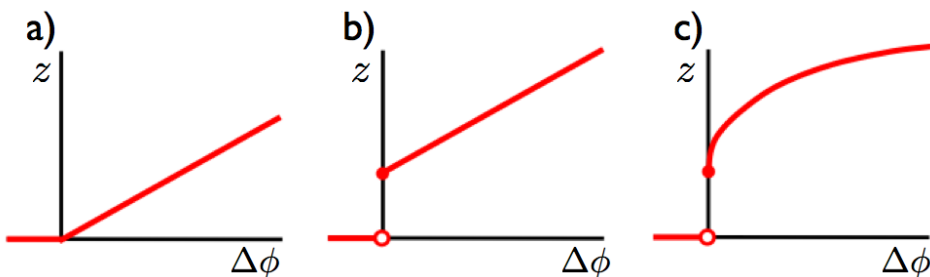


Figure 2.6 – The contact number as a function of the excess packing fraction. a) In the simplest model, the contact number grows linearly with the packing fraction. b) A more realistic model takes into account a minimal contact number (the so-called isostatic value) to begin with, a contact number that at jamming jumps from 0 to $2d$. c) In numerical simulations the contact number grows as the square root of the excess packing fraction above point J.

If the distribution of separations between the initial particles is regular, i.e. all separations occur with similar probability, the contact number grows smoothly from zero under affine compression (Fig. 2.6 a)). This simple model does not balance forces in the packing to make it stable, and as a consequence, the prediction for the growth of the contact number with packing density is far from the numerically observed growth (Fig. 2.6 c)).

Stable packings can only exist once the contact number is above a minimum value, the so-called isostatic value, z_{iso} [16, 17]. Suppose we have N soft frictionless spheres in d dimensions. The contact number equals z . The total amount of contacts in the packing is then $Nz/2$, since each contact is shared by two particles. For a packing to be stable, we require that it should not include floppy modes (which cost zero energy in lowest order, see Fig. 2.7 a)). It can be shown that this is equivalent to demanding that the $Nz/2$ contact forces balance on all particles. For every particle we have d force constraints (force balance in x-direction, y-direction and so forth), so force balance yields Nd constraints on $Nz/2$ force degrees of freedom. One generally expects solutions to such equations only when $z \geq 2d$. The isostatic contact number equals $z_{\text{iso}} = 2d$.

At point J, the pressure is zero, so the particles are undeformed. The distance between two particles is therefore exactly the sum of their radii, giving $Nz/2$ constraints for the Nd positional degrees of freedom. The only trivial solutions are when $z \leq 2d$. Combining these two inequalities yields that at jamming, the contact number for frictionless spheres equals precisely $2d$.

We are now able to make another guess at how z should scale with $\Delta\phi$. If we were to incorporate the balance of forces in our model, we would

imagine that at point J, z would jump from 0 to 4 and then grow linearly for $\Delta\phi \geq 0$, as in Fig. 2.6 b). So what happens in simulations?

In 1997, Durian found that the contact number for a 2D system approaches $z = 4$ near jamming and that $z-4$ scales non-trivially as the square root of the excess packing fraction above point J [13, 18], $\Delta z \sim \sqrt{(\Delta\phi)}$, as seen in Fig. 2.6 c). Most surprisingly, subsequent studies found that this relation is independent of the interaction potential and dimension.

Hence, the contact number already shows highly nontrivial behavior: first, it reaches a well-defined value at the jamming point, and secondly, it grows as a nontrivial power law above jamming. Most mechanical properties depend sensitively on z , and so we can already anticipate that the scaling of these will be surprising too.

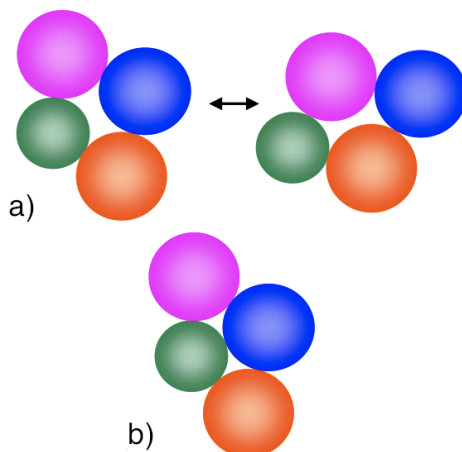


Figure 2.7 – a) For low contact numbers, these packing can be deformed without deforming the particles – this is a (simple) example of a floppy mode. b) For sufficiently large contact numbers, there are no zero energy deformations of this packing possible – apart from trivial translations and rotations. Of course, we could move particles away from one another without energy cost. To make the counting more rigorous, one should consider packings with well-defined boundary conditions.

2.2.2 Elastic Moduli

The elastic moduli of disordered packings show peculiar scaling with distance to the jamming point. When dealing with disordered media, the problem of how to take the disorder into account always arises. Ignoring disorder is an option, but then one can only describe ordered packings. A more subtle approach is provided by the Effective Medium Theory (EMT).

EMT assumes: (i) Macroscopic, averaged quantities can be obtained by a simple coarse graining procedure over the individual contacts. (ii) Applying a global deformation trivially translates to changes in the local deformation. For example, a 1% strain on the entire sample will deform all the contacts between particles by 1%. This second assumption is the “affine assumption” [19].

Before confronting the predictions from EMT with direct numerical simulations, we have to discuss briefly the elasticity of individual contacts in disordered packings. Under small deformations, a packing of soft, frictionless spheres is equivalent to a spring network, where each contact represents a spring. For a harmonic interaction potential, the spring constant is independent of the force; the spring constant of all contacts has the same value. For anharmonic potentials, such as the Hertzian and Hernian interactions discussed above, this is not true. When we start from an already compressed packing, and thus compressed contacts, and want to quantify the effect of additional small perturbations. The spring constant, k , is then given by

$$k = \frac{d^2V}{d\delta^2}, \quad (2.4)$$

where V is the potential, which typically is a power law function of the compression of the springs. Indeed we find for harmonic interactions ($V \sim \delta^2$), the spring constant is independent of the particles’ deformation, and that for general power law interactions ($V \sim \delta^\alpha$), the spring constant scales as $k \sim \delta^{\alpha-2} \sim (\Delta\phi)^{\alpha-2}$.

2.2.2.1 Compression Modulus

The compression modulus (or bulk modulus), K , determines the resistance of a disordered packing against homogenous compression. Under the affine assumption, for a global strain ϵ_{global} applied, this translates directly to the local strain ϵ_{local} felt by all particles. The changes in contact force then scale as $k\epsilon_{\text{local}} \sim k\epsilon_{\text{global}}$, which tells us the elastic modulus is of order k : the elastic moduli follow the typical stiffness of the contacts. Therefore, $K \sim (\Delta\phi)^{\alpha-2}$ [13, 20, 21].

Numerical simulations on disordered packings are consistent with this: the affine assumption works well for compression, although this is a lucky coincidence [21]. Of course the elastic moduli are zero in unjammed packings, and there is, for $\alpha \leq 2$, a discontinuous jump of K in simulations, see Fig. 2.8.

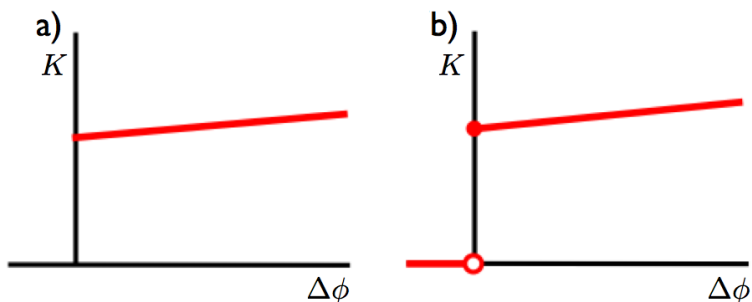


Figure 2.8 – The bulk modulus for packings with harmonic interactions, as a function of the excess packing fraction $\Delta\phi$ in the Effective Medium Theory picture a) and for simulations b). In both cases, slight variations in the modulus with $\Delta\phi$ are expected due to an increase of the density of contacts with compression, but this does not influence the scaling behavior near $\Delta\phi = 0$.

2.2.2.2 Shear Modulus

The shear modulus, G , determines the resistance of a disordered packing against pure shear. Following arguments similar to those for the compression case, EMT predicts that the shear modulus scales as $G \sim (\Delta\phi)^{\alpha-2}$ [13, 19, 20, 21].

Numerical simulations on disordered packings show a different scaling, however: the actual shear modulus scales as $G \sim (\Delta\phi)^{\alpha-3/2}$ [13, 19, 20, 21], see Fig. 2.9.

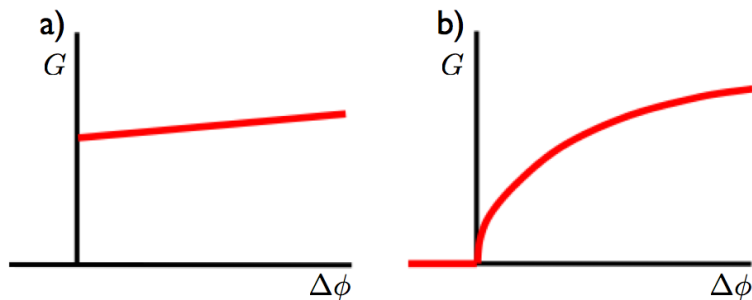


Figure 2.9 – The shear modulus for packings with harmonic interactions, as a function of the excess packing fraction $\Delta\phi$ in the Effective Medium Theory picture a) and for simulations b). For shear, the affine assumption breaks down spectacularly.

Hence, close to jamming, the system is much softer to shear deformations than to compressive deformations, and the ratio of G/K goes to zero,

independent of interaction potential. In fact, making use of the scaling of $\Delta z \sim \sqrt{\Delta\phi}$ one can write this ratio as $G/K \sim \Delta z$.

2.3 Beyond Effective Medium Theory

In the previous section we have seen that the contact number and the elastic properties signal the unique nature of materials near the jamming transition. In this section we briefly sketch *why* these materials behave so differently. We in particular stress the breakdown of the affine assumption.

2.3.1 Nonaffine Deformations

The anomalous scaling of the elastic moduli is related to the nonaffine nature of the deformations of weakly jammed packings, although the precise connection is rather subtle. We will discuss our current understanding below.

An instructive way to illustrate the role of these nonaffine deformations is first, to force the particle displacements to be affine and then let them relax, while measuring the changes in the elastic energy (governed by the elastic moduli) in both cases.

O’Hern and coworkers found that the elastic moduli associated with the affine deformations scale precisely as predicted by effective medium theory. However, the forced system can lower its elastic energy by additional non-affine motion of the particles. These nonaffine deformations are particularly effective for shear deformations, as they are found to change the scaling of the shear modulus [13].

It is tempting to conclude that the nonaffinity is stronger for shear deformations than for compressive deformations. However, subsequent studies have found that for both shear and compression the nonaffine deformations are large, and in fact diverge near jamming [20]. To characterize the local deformations, note that changes in elastic energy depend on the relative motion of pairs of contacting particles as

$$\Delta E = \frac{1}{2} \sum_{i,j} k_{ij} \left(u_{\parallel,ij}^2 - \frac{\delta_{ij}}{\alpha - 1} u_{\perp,ij}^2 \right), \quad (2.5)$$

here u_{\parallel} and u_{\perp} are relative motions of particles parallel and perpendicular to each other, respectively (see Fig. 2.10). Note that u does not refer to flow, but to small, quasi-static displacements in response to external forcing. The u_{\perp} arises from applying Pythagoras theorem, and using Eq. 2.4 to related k and δ , see [12].

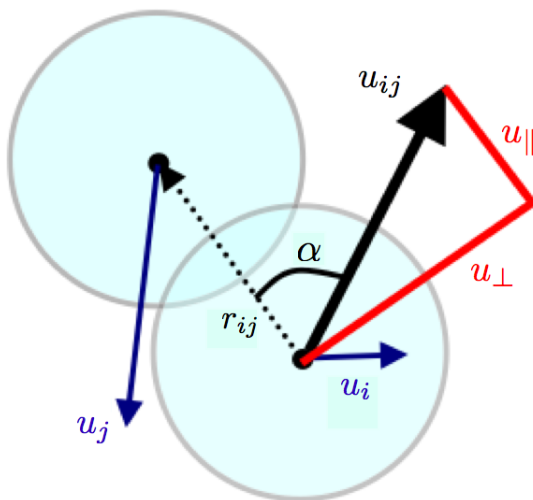


Figure 2.10 – Definition of the relative motion u_{ij} of two particles that each move by u_i and u_j respectively, and the corresponding u_{\parallel} and u_{\perp} .

We now need a parameter to capture the degree of nonaffinity, something that dictates how the system on a local scale responds to an imposed shear or compression as compared to an expected affine response. The probability distribution, $P(\alpha)$, does just this. Ellenbroek and coworkers introduced the displacement angle α_{ij} [20]. Here α_{ij} denotes the angle between \mathbf{u}_{ij} and \mathbf{r}_{ij} (see Fig. 2.10), or,

$$\tan \alpha_{ij} = \frac{u_{\perp,ij}}{u_{\parallel,ij}} . \quad (2.6)$$

Affine compression corresponds to a uniform shrinking of the bond vector between two particles, i.e. $u_{\perp,ij} = 0$ and $u_{\parallel,ij} = -\epsilon r_{ij} \leq 0$, where ϵ is the magnitude of the applied strain on the system. In this scenario, $P(\alpha)$ exhibits a delta-function peak at $\alpha = \pi$. For affine shear, the effect depends on the bond vectors orientation, and for isotropic random packings, $P(\alpha)$ is flat.

In numerical simulations one finds that for large pressures, $P(\alpha)$ is not too different from the affine prediction, but that closer to point J, $P(\alpha)$ develops a substantial peak around $\pi/2$. These correspond to contacts where $u_{\perp} \gg u_{\parallel}$ – in other words, to contacts, where the particles in essence slide past each other. Surprisingly, this peak develops and appears to diverge both for shear and compressive deformations [21, 22].

In addition one can investigate the scaling of u_{\parallel} and u_{\perp} as well. The typical values of u_{\parallel} under a deformation are directly connected to the cor-

responding elastic modulus: for compression, u_{\parallel} is essentially independent of the distance to jamming ($u_{\parallel} \sim \epsilon$), while for shear, $u_{\parallel} \sim \epsilon \Delta\phi^{1/4}$, where ϵ is the magnitude of the strain [21, 22].

The scaling for u_{\perp} , the amount by which particles in contact slide past each other, is more subtle. Numerically, one observes that for shear deformations, $u_{\perp} \sim \epsilon \delta^{-1/4}$. The two terms $\propto u_{\parallel}$ and $\propto u_{\perp}$ become comparable here, and the amount of sideways sliding under a shear deformation diverges near jamming [20, 21, 22]. For compression there is no simple scaling. Knowing that $\Delta z \sim \sqrt{\Delta\phi}$, the above expressions for u_{\parallel} and u_{\perp} , and guessing that in this case the two terms in Eq. 2.6 would balance, one might have expected $u_{\perp} \sim \epsilon \delta^{-1/2}$. However, the data suggests a weaker divergence, close to $\Delta\phi^{-0.3}$. Nevertheless, both under shear and compression, the sliding, sideways motion of contacting particles dominates and *diverges* near jamming.

The preceding findings illustrate the strange nature of linear response close to the jamming transition.

2.4 Experimental Review

We have seen that soft frictionless spheres near the jamming transition exhibit a wealth of nontrivial and unexpected behavior, that the response is strongly nonaffine and the elastic moduli are anomalous. However, the approach we have taken above is strictly theoretical and it is helpful to get a good overview of elasticity experiments on jamming to the present date as well.

Experiments on 3D foam and emulsions were performed in the 1980's, focusing on cone-plate and Taylor-Couette geometries [23, 24, 25, 26, 27, 28, 29, 30]. First estimates of the scaling of the shear modulus with respect to the packing fraction were obtained by Princen and Kiss [28] using polydisperse oil-in-water emulsions. This work was followed in the 1990's by Mason et al. [30], who suggested the variation versus the packing fraction for monodisperse emulsions. They found a linear dependence: $G \sim \phi(\phi - \phi_c)$, where $\phi_c \approx 0.64$ is the critical packing fraction in three-dimensional, monodisperse packings. Mason et al. found that the osmotic pressure scaled similar to the shear modulus with ϕ , which means that the bulk modulus, being the derivative of the pressure, has to differ significantly from the shear modulus at ϕ_c , although the data is noisy. They also did not observe that the ratio G/K goes to zero at the jamming point. Mason did, however, also stress the importance of the nonaffine motion in their emulsions, if they were sheared close to the critical point. He hypothesized

that these motions arose from localized relaxations of the droplet positions. This was later confirmed by O'Hern et al. in simulations [13].

In all these studies, however, a real relation between bulk rheology and the behavior at the single particle level was never established. What actually happens on the bubble-bubble scale under a continuous shear strain, for example? For small applied strain, the bubbles are deformed minutely, yet still want to restore their equilibrium surface area. They respond elastically, the way a solid would [31]. If the strain is increased further, the foam relaxes through bubble rearrangements [23]. With a large enough strain the system starts to flow irreversibly and there are continuous rearrangements [24, 32]. This type of behavior is of course dependent on how far from the critical point the system is. In dry foams, far from ϕ_c , [33, 34, 35] found that rearrangements in the form of so-called T1 events, where two nearest-neighbor particles become next-nearest neighbors, (discussed in greater detail in Chapter 5) negate the build-up of stress. No experimental studies have focused on plasticity in wet foams close to ϕ_c as of yet.

The structure of these elastic systems was also carefully examined close to the jamming point. Imaging of 3D packings of foams and emulsions to look at static structures needs some sophisticated imaging techniques to peer through the opaque samples, such as DWS [36], x-ray tomography [37] and confocal microscopy [14, 38, 39]. In 2D, Bolton [40] found that the critical packing fraction for a system of disordered discs was $\phi_c = 0.842$ and that two-dimensional, disordered systems [41] do not exhibit a linear increase of G near ϕ_c in 2D, contrary to results for 3D systems used by Mason, although the osmotic pressure did increase quadratically near ϕ_c .

The study of flow in bubble packings was studied extensively by [4, 5], where the packing fraction is controlled precisely. In this work, Katgert et al. showed how great control of a two-dimensional foam can yield interesting behavior of the shear modulus. By controlling the packing fraction, they were able to show the square-root scaling of the packing fraction with the contact number with correct prefactors, as well as velocity profiles of bubbles in a packing under shear.

A different approach to what has been seen so far was taken by Cheng [15], who used the swelling of confined tapioca particles to go through the jamming transition to observe the nonaffine behavior there. In this seminal work, Cheng found the classic signature of the jamming transition by observing the tell-tale first (and second) peak in the pair-correlation function. Furthermore, by looking at the displacement fields, he found that a static length scale in the system reached the system size at ϕ_c . Further

work probing the jamming transition, using hydrogel particles, which are polymers that swell when introduced to salty water, is being performed by the van Hecke group, as well as the Behringer group.

2D Foams in a Wedge Geometry: Set-up

In this Chapter we describe the experimental setup that we have developed for probing the jamming transition in 2D foams. We use a bidisperse 2D foam packing consisting of bubbles sitting under a glass plate, like in [4, 5, 9, 10]; the glass plate helps to stabilize the foam, and eliminates the capillary attractions that arise for freely floating bubbles, thus allowing us to probe very wet foams and approach the jamming transition closely.

In our set-up, we confine our foam into a wedge geometry, which consists of two fixed and one freely rotating wall, forming a “pizza-slice” geometry. The rotating wall is connected to a rheometer, which allows us to control the imposed strain on the foam. In particular, it allows us to both compress and shear the foam. At the same time, this rheometer also allows us to probe the resulting torques, which directly translate into the pressure in the foam. We also image the foam from above, using a standard CCD camera, thus tracking the rearrangements and motion in the bulk.

There should be no doubt that this is a challenging experiment. 2D foams are really soft and, particularly when close to unjamming, very fragile. We therefore have to resolve very small forces, which motivates our use of a rheometer to measure these. Moreover, these fragile foams have a sluggish response, necessitating long experiments, which in turn require a good long term stability of the experiment; in particular, we have to stabilize the temperature, and make sure that coalescence and coarsening, intrinsic to foams, are minimized.

This chapter gives a detailed description of the experimental set-up that we developed. In Sec. 3.1 we first explain the rheometer geometry, how we make the foam, control the temperature and image the set-up. In Sec. 3.2,

we show how we adjust the tilt of the glass plate, and experiments on drifting bubbles, which give us important information of how the packing will behave under certain tilts we will impose to collect our data. Finally, in Sec. 3.3, we describe the protocols with which we compress the foam packing, and how the system behaves with varying compression and sit times.

3.1 Experimental Set-up

In this section we describe the set-up that we constructed to probe the jamming transition in two-dimensional foams. The main idea is illustrated in Fig. 3.1: a two-dimensional foam, consisting of a single layer of bubbles, floating on a surfactant solution and trapped below a glass plate, is kept in a wedge shaped area. Two side walls of the wedge are fixed, the third is mounted on a central axis, and acts as a wiper. By rotating the central axis, we can compress or decompress the foam. The axis is coupled to a rheometer, allowing accurate mechanical measurements of the foam. In parallel to these mechanical measurements, we image the foam from above, allowing us to follow and characterize the motion of the bubbles under compression.

The foam bubbles we use are between $2 - 4 \text{ mm}$ in diameter and even for compressions between about 10^{-7} m and 10^{-4} m , the bubbles have a effective spring constant of 0.02 Nm^{-1} and 0.075 Nm^{-1} , respectively [42]. This means they are very soft, and that the forces involved in compressing our two-dimensional foams are tiny. We therefore control the rotating of the wiper by a rheometer, allowing us to measure torques as small as $0.5 \mu\text{Nm}$ with an angular resolution better than $1 \mu\text{rad}$. By rotating the wiper we can thus both compress and measure the elastic response of the foam.

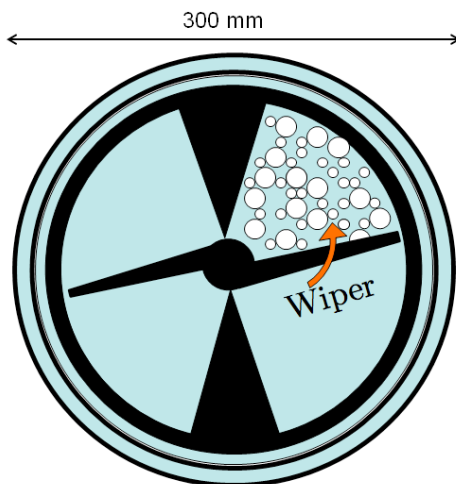


Figure 3.1 – A top view schematic of the compression dish with black aluminum frame. The wiper is the third and only moveable wall of the wedge-shaped area the bubbles are confined to under the glass plate. A shaft connects the rheometer (sitting out of the plane) and the wiper, which imposes strain steps to compress the foam.

Since we wish to approach the jamming transition in these two-dimensional foams as close as possible, there are numerous experimental issues that need to be resolved, including stability of the foam, temperature control, and leveling. The outline of this section is as follows. We will first describe the set-up's components and how they are put together to create the wedge in which the foam is kept in Sec. 3.1.1. In Sec. 3.1.2 we describe the process of making the soap solution and how the bubbles are made. Additionally, we describe the way in which the foam is loaded into the experiment. In Sec. 3.1.3 we explain how the set-up is kept at a constant temperature during the course of an experiment. Then, in Sec. 3.1.4 we describe how we image the foam packing from above. Additionally, we highlight imaging techniques applied before analysis can be done.

3.1.1 Set-up

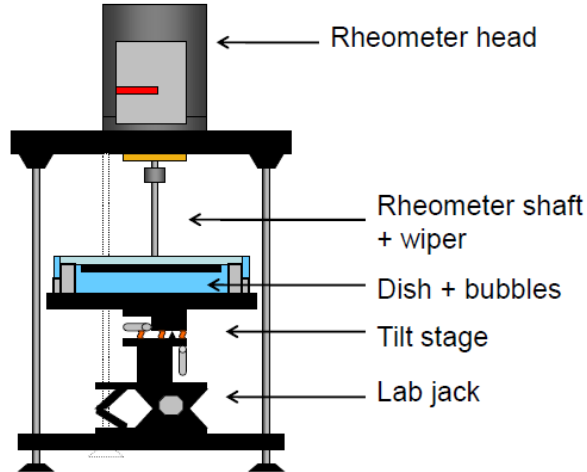


Figure 3.2 – A side view of the bulk compression experiment. The rheometer shaft is attached to a wiper which can compress the bubbles under the glass plate. Leveling can be done with the tilt platform. A close-up of the dish which contains the foam solution and bubbles is presented in Fig. 3.3.

The set-up, Fig. 3.2, is composed of the main “dish”, which holds the foam solution, the glass plate and the bubbles. The dish is circular, 300 mm in diameter with an inner diameter of 250 mm and 40 mm deep, cut from a block of PMMA, see Fig. 3.3(D). An anodized piece of aluminum creates the boundaries of the sample cell and sits submerged in the cut-out area of the dish, as seen in Fig. 3.3(C) and Fig.3.1. An anodized “wiper” comprises the compressing face of a wedge shaped area the bubbles are trapped in and is attached to the rheometer by a shaft, which sits out of plane of the set-up, Fig. 3.4. We use an Anton Paar DSR 301 rheometer, which can be used in stress controlled mode and by a feedback mechanism, in strain controlled mode.

The wiper is 107.5 mm long and has an effective edge length of 97 mm to enclose the foam. There is a gap of 1 mm between the tip of the wiper and the anodized aluminum frame, which is small enough to ensure that no bubbles can escape the wedge area under compression.

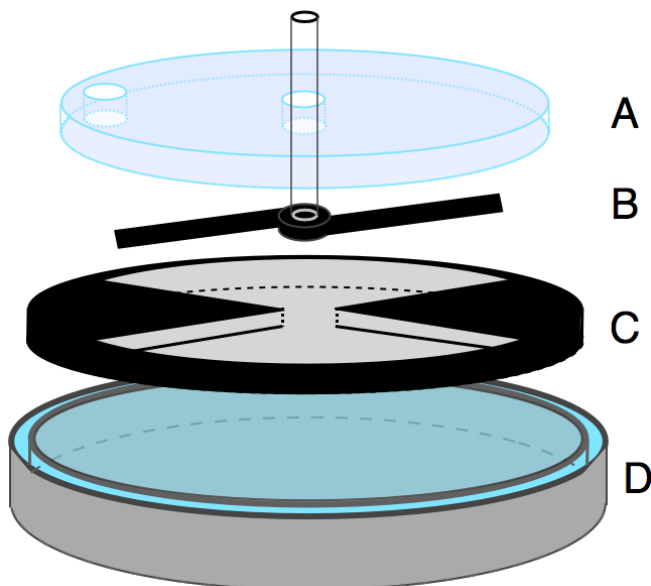


Figure 3.3 – Schematic of the dish and other components. From top to bottom: the glass plate (A) with the anodized wiper (B), the anodized aluminum frame which creates the boundary of where the foam sits (C) and the PMMA dish that holds the soap solution (D). The bubbles sit under the glass plate, confined by the aluminum frame (C). The wiper’s shaft is connected to a rheometer, which rotates the wiper, as is shown in Fig. 3.1. The dish (D) contains the soap solution and has an outside reservoir (shown as a blue-colored ring) from which solution can be extracted to enable the loading of bubbles through the perimeter hole on the glass plate, as described in Sec. 3.1.2.

The dish sits on a tilt platform that can be lowered to allow the sample to be replaced, as described in Sec. 3.1.2 and Sec. 3.2. The tilt platform is comprised of a Newport M-37 Tilt and Rotation platform mounted on a Newport 281 High Load Lab Jack.

Additionally, the experiment is isolated from vibrations of the ground, by being placed on an optical table.

The glass plate under which the bubbles sit is made from 10 *mm* thick plain window glass and is 260 *mm* in diameter. This window glass was first ground and then polished by a manufacturer, accurate to about 0.02 *mm* / 300 *mm* (14 arcsec), see Fig. 3.5 a). We use this specially milled glass plate since normal glass panes are not flat enough and lead to drift of the bubbles sitting under it because of the “sagging” of the glass plate, as well as holes in the packing, as can be seen in Fig. 3.5b). The flatness is required so that the bubbles do not get “pinned” in place by impurities on the glass

surface. In Sec. 3.2.1 we test whether the polished plate is indeed flat. We find that it is very flat and that there is hardly any pinning left.

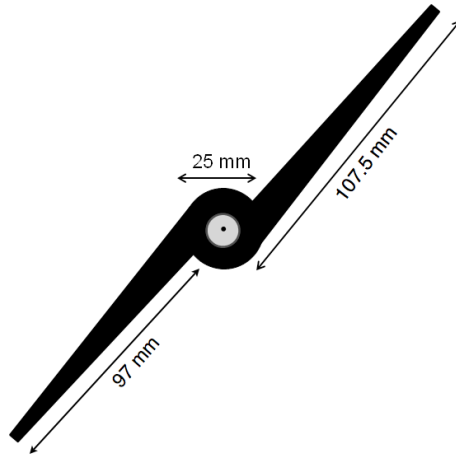


Figure 3.4 – Top view schematic of the anodized, aluminum wiper. The effective edge of length 97 mm compresses the bubbles under the glass plate. The wiper creates the third wall of the wedge-shaped area the bubbles are confined to under the glass plate. A shaft connects the wiper to the rheometer, which sits out of the page.

The plate has two holes of 17 mm diameter, one around the edge and one in the center through which the wiper shaft is placed. The plate is placed on top of the aluminum frame and thus encloses the entire foam, as seen in Fig. 3.3. Once all pieces are placed together, the foam solution is poured into the dish. During this process, air bubbles become trapped under the glass plate and are removed by rotating the plate in such a way that the hole at the perimeter provides the escape.

Once all excess air bubbles are removed, a bidisperse foam can be loaded into the cell.

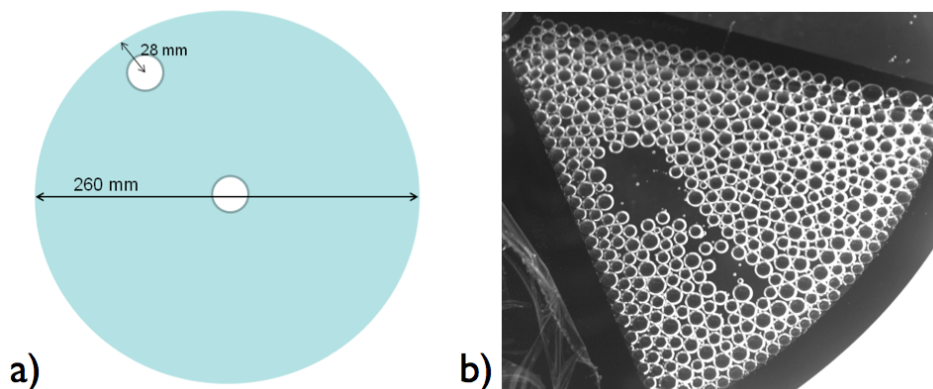


Figure 3.5 – a) A schematic of the glass plate. The plate is made from 10 mm window glass, yet one side under which the bubbles sit is machine polished to achieve a flatness of roughly 14 arcsec. The holes have a diameter of 17 mm. In b) we see how a packing is effected due to unevenness of a non-polished glass plate (before it was ground and polished): the glass plate “sags”, causing the packing to drift away from these areas.

3.1.2 Foam

To approach the jamming transition by compression we must ensure that the sample does not crystallize. Especially in two-dimensional systems, this will occur readily in monodisperse systems. We therefore follow a well-known protocol used in numerical simulations [13] and use bubbles of two different sizes. The bubbles are about 2 and 4 mm in diameter, measured by image analysis.

The foam solution is made according to the recipe in [43]. It is created in a two step process: first, a solution with total surfactant concentration of 10% consisting of 6.6 wt% anionic surfactant sodium lauryl ester sulphate (SLES) and 3.4 wt% zwitterionic surfactant cocamidopropyl betaine (CAPB) is added to 540 mL demineralized water and stirred on a stir plate without heat. This is stirred until the SLES is completely dissolved, since it has a very viscous, wax-like texture. At the same time a stock mixture of 6.84 L of demineralized water and 4.56 L glycerol solution is made and shaken violently by hand to ensure that the glycerol has mixed properly with the water. The two solutions are mixed together by carefully pouring the high concentration surfactant mixture into the water/glycerol mix, since any shaking causes a lot of foaming. The water/glycerol phase dilutes the surfactant solution 20 times. Batches of 12 L are made at a time in this way, and about 1.5 L is used for any given experiment.

The final soapy solution is comprised of 0.33 wt% SLES and 0.17 wt%

CAPB and has a glycerol concentration of 38 *wt%*. The density of the solution is measured by pouring a known amount into a beaker on a scale. We find $\rho = 1094 \pm 2 \text{ kg m}^{-3}$.

We measure the dynamic viscosity η of the bulk solution with a Cannon Ubbelohde viscometer and find $\eta = 3.87 \pm 0.01 \text{ mPa}\cdot\text{s}$. The surface tension, σ , was measured using the pendent drop method: a droplet of solution is suspended from an 18G (0.84 *mm* inner diameter) syringe and the curvature is measured, according to [44]. From this the surface tension is extracted. We find $\sigma = 26.5 \pm 0.3 \text{ mN}\cdot\text{m}^{-1}$.

The foam is made separately in a petri dish by blowing N_2 gas at a constant rate through a needle submerged 20 *mm* deep in the solution. The base pressure of the gas is 3.5 *bar*, but decreased and tuned to useable levels using valves. To control the two different bubble sizes, we use two different gauge needles, 21G and 25G (0.51 *mm* and 0.26 *mm* inner diameters, respectively). We create about 50% big bubbles and 50% smaller bubbles by number.

The foam is then ladled with a spoon into the hole at the perimeter of the glass plate, which can be seen in Fig. 3.5. By extracting solution around the open, outer ring of the dish, see Fig. 3.3, an under pressure is created, which allows the bubbles to be “sucked” under the glass plate. The level of the solution never drops below the bottom of the glass plate. During this process, many small, unwanted bubbles are created, as seen in Fig. 3.6 a). The small bubbles cause problems during an experimental run in that they create slip-planes along which rearrangements can happen in a sample that would be otherwise in equilibrium. Additionally, these “satellite” bubbles under high compression coalesce with other bubbles in the packing, further bringing the packing out of its equilibrium state. They are removed by use of a bent syringe, which is fed in through the hole along the perimeter of the glass plate. This is also an effective means of ensuring, by eye, one last time that the packing does not have any crystalline patches or an overabundance of big or small bubbles before we enclose the set-up, see Sec. 3.1.3. Part of a “clean” packing without unwanted satellite bubbles or crystalline patches is shown in Fig. 3.6 b).

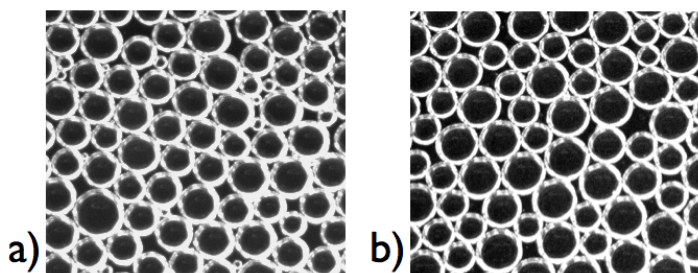


Figure 3.6 – a) A zoom in of a packing of bubbles showing many small, unwanted “satellite” bubbles created when loading the compression cell. These small bubbles can sit in the Plateau borders of larger bubbles and in the course of an experiment be the sources of slip-planes, which lead to rearrangements when there would normally have been none. Additionally, if the compression is high enough, these small bubbles can coalesce with others, further disrupting a packing in equilibrium. b) Part of a clean packing without satellite bubbles. The small bubbles are removed with a bent syringe needle.

Newly loaded samples are stable for about one to two days, meaning the likelihood of coalescence events, even under high compression, is rather low. However, after this time the foams rapidly lose their usefulness, since coalescence dominates their behavior. Coalescence means two bubbles which are pushed together merge into one big bubble due to the rupture of the film separating them. These merging events can be observed in the torque signal of the rheometer, mostly at low compressions, since the change in area causes the wiper to measure a torque different than before. In Fig. 3.7 we see how the torque measured by a coalescence event changes. There is a sharp spike due to the actual event before the system relaxes to a new equilibrium.

It is easy to identify two bubbles merging as shown in Fig. 3.7. When two bubbles of the same radius R merge, the area increases by a factor of $2^{2/3}$. The subsequent rearrangements in the sample and drop in torque signal can be explained by a voronoi-type argument: it is the change in the number of neighbors before and after the coalescence event that determines the change in torque signal. As shown in Fig. 3.7, the peak in the torque signal is due to the actual creation of the larger bubble, but the noticeable drop in the torque signal comes from the number of neighbors changing with the new bubbles. The system must rearrange itself to keep a stable configuration. This chain of events can lead to the packing not being stable for many hundreds of seconds, effecting even the next compression step from reaching an equilibrium. Coalescence events are certainly identifiable, yet also rare in our bubble packings.

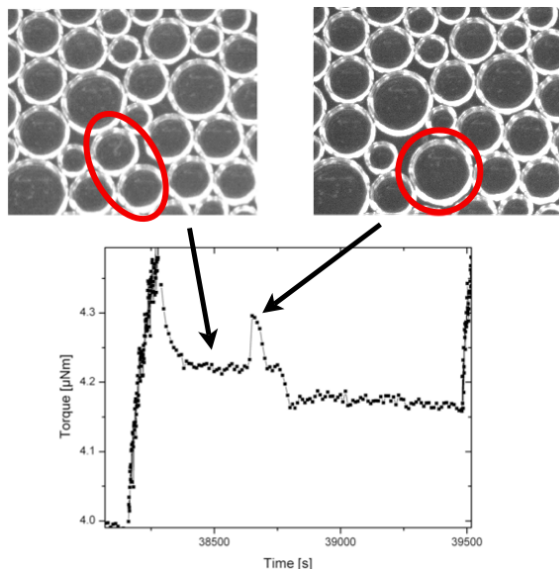


Figure 3.7 – A coalescence event in the bulk of the packing and the corresponding change in the torque signal measured by the rheometer. The two consecutive images (top, left to right) show a coalescence event highlighted by the red circle. Two bubbles merge to become one due to rupture. Such events become more common the older the sample is. Note how after the event the relaxation profile (bottom) equilibrates to a lower torque than it was originally going to. This is due to the system rearranging itself to compensate for the newly created bubble.

At higher compressions the coalescence events are not picked up in the signal. However, we do know they occur occasionally by image analysis.

3.1.3 Temperature Control

Over the course of an experiment, which lasts several hours, the ambient temperature in the experimenting room varies depending on the outside weather. Direct sunlight coming through the windows in the summer or strong cooling over a winter night are main concerns. The fluctuation of the lab temperature can be as much as 5°C over the course of a day. Since the bubbles are made of N_2 gas, they are not impervious to these temperature fluctuations and will expand or contract depending on the ambient temperature.

By Charles's law

$$\frac{V_1}{T_1} = \frac{V_2}{T_2} \quad (3.1)$$

where V_1 is the volume of the bubble, T_1 the starting temperature, T_2 the

new temperature and V_2 the new volume of the bubble due to the variation in temperature. If the temperature changes by 5 K , as the lab temperature does on a hot, sunny summer day, $\Delta V = 1.6\%$.

However, to study the jamming transition, we need a precise control over the packing fraction, which necessitates accurate temperature control.

To help do this, the whole experiment sits inside a white polystyrene box of $100\text{ cm} \times 80\text{ cm} \times 80\text{ cm}$. Its walls are 10 cm thick. The box is suspended from the ceiling of the lab and can be hoisted up and down over the experiment to enclose it completely. Fig. 3.8 b) shows the experiment enclosed by the polystyrene box. Additionally, a 3 cm thick piece of polystyrene is used to isolate the set-up as much as possible from the steel plate that makes up the optical table top on which the set-up rests, see Fig. 3.8 a). The polystyrene is EPS 100-SE and was chosen because of its low conductivity of $\sim 0.036\text{ Wm}^{-1}\text{K}^{-1}$. This way we insure that over longer periods of heating the better part of the heat created stays inside the box.

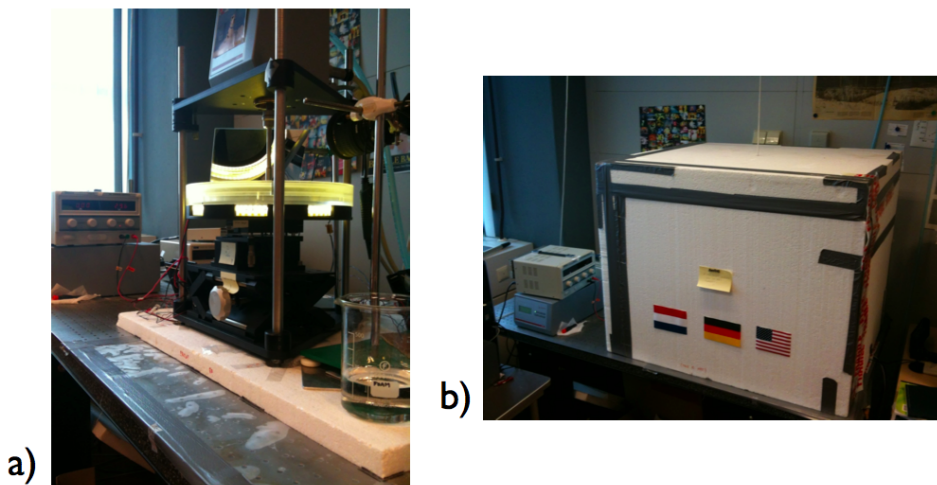


Figure 3.8 – The experimental set-up. In a), the 3 cm thick piece of polystyrene the set-up sits over is shown. This piece helps to thermally isolate the set-up from the metal table it sits on. In b), one can see the entire polystyrene box that is hoisted over the set-up to help maintain a constant temperature. The walls of the box are 10 cm thick.

To heat the inside of the box we use two 5 W heating elements connected in series, driven at 30 V . The heaters are connected to a Solid State Relay so that they can be switched on and off by a 5 V signal controlled by a computer. Additionally, two large fans of diameter 10 cm are placed inside

the box to circulate the air. One extra, smaller fan is placed in such a way that it blows over the LED lights (see Sec. 3.1.4) beneath the dish to ensure no heat is trapped under the set-up. It is imperative that no heat is trapped directly under the dish, since convection currents in the soap solution occur as a result of the heat. This in return effects the stability of the foam packing.

We control the temperature inside the box by way of a Product, Integral, Differential (PID) feedback loop. A PT-100 resistor ($100\ \Omega$ resistance at $0\ ^\circ\text{C}$, ideally) at $10\ \text{V}$, $20\ \text{mA}$, wired in a Wheatstone bridge circuit is used to read in a voltage, V_B , measured across the two channels of the bridge, see Fig. 3.9. This measured voltage (the “process variable”) corresponds to the measured air temperature inside the box.

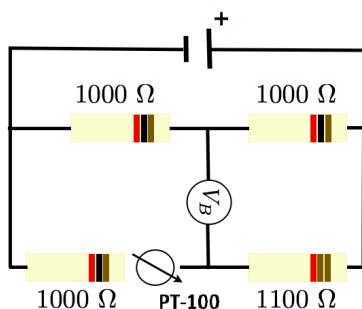


Figure 3.9 – The Wheatstone bridge used for reading the bridge voltage in the circuit, V_B . This bridge voltage is called the process variable and is used in a LabVIEW code to measure the temperature inside the box. When the temperature changes, the PT resistor changes its resistance, changing the process variable.

This process variable is fed over a switchboard to a National Instruments PCI-6221 card to a LabVIEW code. The code then converts the voltage signal and determines the duty cycle of the heaters by way of the Solid State Relay so that a set-point temperature can be reached.

We set the set-point temperature close to $27.5\ ^\circ\text{C}$, above the ambient room temperature, since we can only heat the set-up. The precise temperature reached has to do with calibration of the PID loop and is not important, as long as it is above the ambient room temperature and is stable over long periods of time. The only temperature loss is due to the walls, which is very slow. The LabVIEW program ensures that if the temperature exceeds the set-point, the heaters are turned off and the system waits until the process variable sinks. However, the settings of the heaters that are controlled from the program are not strictly on/off. By use of the feedback, the program constantly reads the process variable and de-

termines a duty cycle: how much voltage the heaters need at any time to reach the set-point. The amount of time on or off is constantly updated until the set-point temperature is reached. By tuning the PID gain parameters, the program can approach the set-point faster or slower, with more or less overshoot or undershoot. We have managed to tune the parameters so that there is hardly any overshoot or undershoot, as seen in Fig. 3.10 a).

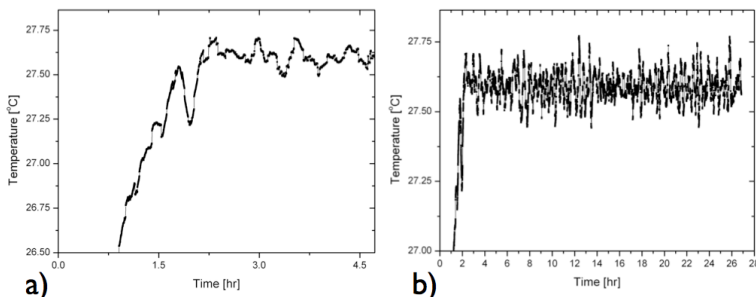


Figure 3.10 – a) The process variable as a function of the time when heating the box. The set point is around 27.5 °C and the temperature quickly climbs to this value before fluctuating around it. The temperature reaches its set point without any major undershoot or overshoot. b) The temperature as a function of time for a full experimental run. The set point temperature is roughly 27.5 C. Here the temperature control ran for 27 hours without any major fluctuations from the set point, showing how well the temperature can be controlled by way of the PID loop.

It takes over an hour to bring the temperature inside of the box to the set-point of 27.5 C. During the long heat-up time, all components inside the box must also reach the set-point. Before this no measurement can be made on the foam. The temperature will then start to fluctuate around the set point temperature. The oscillations in Fig. 3.10 b) come from the PID constantly updating itself to fluctuations of the ambient temperature of the lab outside the box. If the temperature changes slowly, for instance when the evening cools down, the PID can account for these changes in the lab temperature.

The stability of the temperature is constant over long times, not varying by more than ± 30 mK around the set-point, as is shown in Fig. 3.10 b). We can now see that, using Eq. 3.1, with the temperature varying no more than ± 30 mK, $\Delta V = 0.01\%$. This volume change is small enough that it can be ignored. It allows us to carry out our experiments sufficiently close to the jamming transition without having to worry about variations of the bubble volume over time.

One problem that arises when having such a “high” temperature inside

the box with air always circulating, is evaporation. Older experiments left the outer ring of the dish open to the air, as depicted in Fig. 3.3. Over the course of long experiments, the solution would evaporate from these parts and the level would sink. We would lose up to 30 *mL* of solution this way per day. Not only do we lose solution, we also change the concentration of the surfactant in the solution. The lighter fluid, in this case the water, evaporates away, leaving behind more glycerol. This can lead to changes in the behavior of the foam. To address this problem, we place a petri dish with 100 *mL* de-ionized water inside the box to keep the air humid. In addition, we place a circular rubber sheet over the exposed area on the perimeter of the pan. This way evaporation is reduced to a less than measurable amount.

3.1.4 Imaging

To observe the dynamics of our system under compression we film the set-up from above. The torque signal output by the rheometer can now be matched with rearrangements as well as coalescence events. The proper lighting of the foam is also crucial, since only with the light striking the Plateau borders at the right angle do the bubbles appear as discs when viewed from above.

The foam is lit from below at a slight angle by a strip of flexible LED (Silikon LED Flexstrip from SLV Elektronik GmbH) lights that sit directly under the dish, as seen in Fig. 3.11. The strip is bent into a circular shape and thus lights the entire dish from below. Imaging is done using a CCD camera (Basler A622f with 1280×1024 pixel resolution), equipped with a Sigma EXDG telephoto zoom lens. The leveling platform on which the dish sits is black, to enhance contrast, as in Fig. 3.11. The camera is triggered from a LabVIEW code and the frame rate is fixed at 0.1 *Hz* or 0.033 *Hz*, depending on the compression protocol. The camera points along the x-axis onto a tilted mirror to film the set-up.

Due to the way the camera is filming the experiment we need to correct the images. The camera and mirror set-up do not image the bubbles exactly from above due to how they are placed inside the polystyrene box. From the front of the image to the back of the set-up is designated the y-axis, as shown in Fig. 3.16 b).

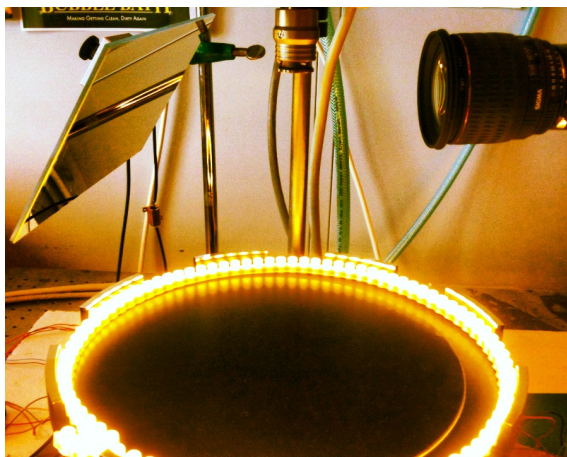


Figure 3.11 – The camera (right) and mirror (left) placement above the tilt platform where the LED light strip lights the dish (not shown) from below. The lights are placed at a slight angle underneath the place where the foam packing will ultimately sit. The leveling platform is black to enhance contrast. Due to the tilt of the mirror over the dish and the alignment of the camera the images are skewed and will be corrected.

Similarly, the x -axis runs from left to right. The image is taken at a slight angle to normal, leading to the images being skewed. This means that a bubble seemingly becomes larger when it moves “closer” to the front of the image and shrinks when it moves towards the back. Parallel lines do not appear parallel, but splayed. To add to this, the direction of the x - and y -axis is not aligned with the image, since the camera does not point “exactly” along the x -axis.

We use a calibration image to correct the images as follows. The calibration image has a coordinate axis drawn on it that is aligned with the actual axis of the set-up. From this template grid, we map the correct coordinates on to any image of the bubble packing obtained by the camera using two IDL routines, POLYWARP and POLY_2D.

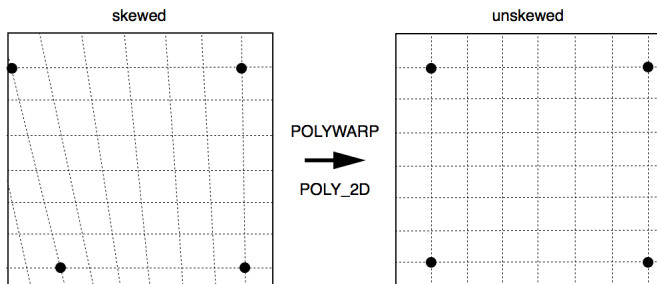


Figure 3.12 – Cartoon of how POLYWARP and POLY_2D correct an image that is skewed. The black grid points are a guide to how the picture is corrected after the transformation.

POLYWARP determines rotation coefficients by performing polynomial spatial warping using tie points on the template grid to map to new coordinates on the rotated, skewed image, as illustrated in Fig. 3.12.

POLYWARP determines the polynomial coefficients $kx_{i,j}$ and $ky_{i,j}$ needed for image transformations from the polynomial functions:

$$x_i = \sum_{i,j} kx_{i,j} x_0^j y_0^i$$

$$y_i = \sum_{i,j} ky_{i,j} x_0^j y_0^i$$

The coefficients $kx_{i,j}$ and $ky_{i,j}$ are the inputs to the POLY_2D routine. The coordinates x_i and y_i are chosen from an image and correspond to some set of points (x_0, y_0) , set in advance from a calibration grid. Fig. 3.13 a) shows a calibration grid image from which (x_0, y_0) and (x_i, y_i) are extracted.

Next, we use POLY_2D, which performs the actual geometrical warping of the image with the rotation coefficients from POLYWARP above. The warping coordinates (x', y') are determined as

$$x' = \sum_{i=0}^N \sum_{j=0}^N kx_{i,j} x^j y^i$$

$$y' = \sum_{i=0}^N \sum_{j=0}^N ky_{i,j} x^j y^i$$

Fig. 3.13b) shows the calibration grid image corrected after the POLY_2D routine has performed the warping, using the coefficient inputs $kx_{i,j}$ and $ky_{i,j}$, determined by POLYWARP.

Since some pixels in the rotated image need to be padded due to the transformation, the POLY_2D routine performs an additional bilinear interpolation to decrease pixel noise. We could do this up to arbitrary order but use only linear order. Higher order means using more reference points, which is not necessary for our experiment. This method of image correction is used on all data sets before image analysis is preformed.

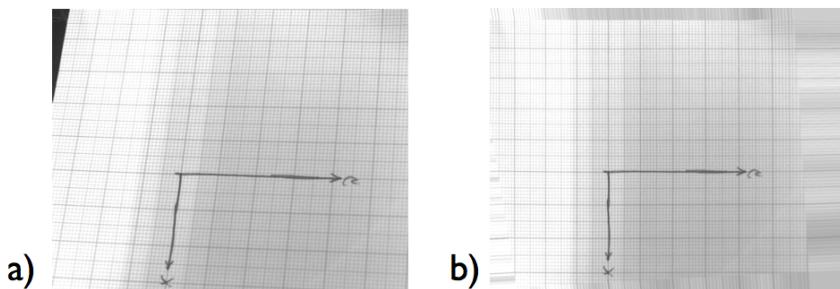


Figure 3.13 – The calibration grid before, a), and after, b), the transformation done using two IDL routines, POLYWARP and POLY_2D. Shown is ruled, 1 mm paper. Note how in a) parallel lines are splayed due to the skew of the camera’s imaging. In b), one observes that the borders of the new image are stretched due to the transformation process. Only the inner part of the image showing the grid is of interest.

3.2 Leveling

While running the compression experiments, a leveling of the system presents itself as a very important issue. We have already tried to solve this by use of a polished glass plate. The leveling is fundamentally important in running any set of experiments since the motion of the bubble packing is very sensitive to the tilt of the glass plate with respect to gravity.

From jamming theory we have an idea of what our ideal scenario would be: the packing, under compression, should behave as a loose collection of bubbles in Fig. 3.14 a). That is, the bubbles initially sit under the glass plate, which in this scenario is mathematically perfectly flat, and are not touching. As we increase the packing fraction by decreasing the area they occupy, as we are doing in our compression experiments, they come together, touch and then pack together and deform. By this process one cleanly goes through the J-point, and measuring the elastic response would be an easy task.

However, this ideal scenario is a far cry from the actual situation when we preform experiments. It is impossible to (i) have a perfectly flat glass

plate and leveled system and (ii) create a packing of bubbles that sits in an initial configuration where no bubbles are touching.

We face the following problem: any experiment starts with a tilt that is not perfectly level. As a result, all bubbles in a packing are fully in contact. This means that the system starts out with a built-in stress due to the buoyancy of the bubbles pushing the packing into some configuration, due to tilt. The experiment is subject to continuous off-tilt of the glass plate in compressing our packing through the J-point. However, as outlined in points (i) and (ii) above, this is a Sisyphean task.

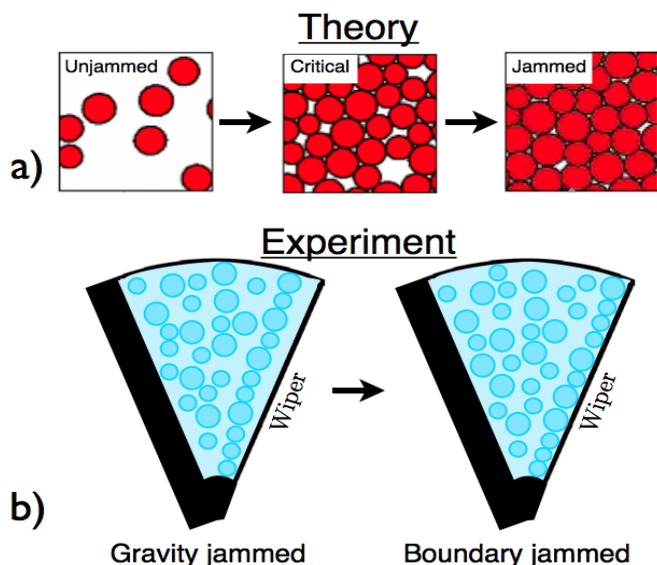


Figure 3.14 – A comparison of theory and experimental approaches to foams. In a), a packing of bubbles goes through the jamming transition from an unjammed to a jammed state. In our experiments, as depicted in b), we start in a “gravity jammed” configuration with a hole between the packing and the wiper and compress until we are in the “boundary jammed” regime. Here the wiper has now closed the hole and is fully compressing the foam.

To counter these problems, we use the reality – that we can never perfectly level the system – to our advantage by purposely biasing the tilt. The bubbles now sit, due to our imposed tilt, in the wedge-shaped area. Furthermore, to draw parallels to the ideal scenario of going through the jamming transition, we tilt the bubbles into a configuration where a hole is created between the packing and the wiper, as in Fig.3.15. During compression, this hole is closed and the packing is said to undergo a transition from a “gravity jammed” (still weakly jammed due to the buoyancy gradient) to

a “boundary jammed” state, as shown in Fig. 3.14b). We expect the torque signal to mark a clear difference between these two regimes, since in the gravity jammed scenario, the wiper is not fully compressing the system and thus not measuring the actual bulk modulus of the packing. Once the hole is closed and the packing is fully enclosed, the boundary jammed regime, we are measuring the compressibility of the foam.

Thus we have now a real world analog to the ideal, theoretical case of compressing a soft system. The results of using this approach are outlined in detail in Sec. 4.3.

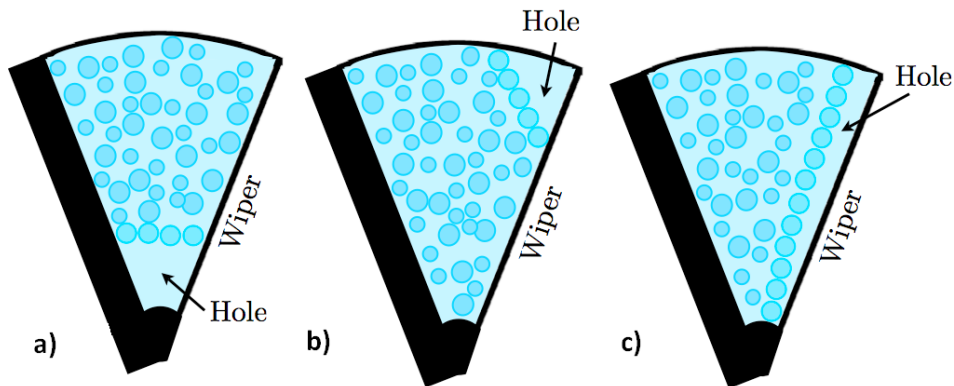


Figure 3.15 – A cartoon of a number of different hole configurations used. Initial experiments with a biased tilt creating a hole in the packing were done, leading to versions a) and b). These experiments were improved upon once we saw that a cleaner signal was obtained by using hole configuration c), a hole running the length of the wiper axis.

The main dish holding the foam solution sits on top of a specially created leveling stage described in Sec. 3.1.1. The tilt platform uses two screws to adjust the tilt in the x - and y -direction. The screw is subtended into 50 “ticks”. One full rotation is 0.5 mm . Thus, each tick changes the travel of the screw by $1/100\text{ mm}$. The screws sit a distance of 89 mm apart, which means that one full rotation tilts the platform by 5.61 mrad . Therefore, $1\text{ tick} = 0.11\text{ mrad}$. A schematic of the tilt platform is illustrated in Fig. 3.16 a).

Since the tilt can now be set very finely, we use a master orientation which tells us where the bubbles will move when we adjust the tilt screws. The convention uses the way the whole set-up sits on the optical table: from the front of the table to the back, going through the experiment if sitting in front of it, runs the y -axis. Again, sitting in front of the experiment, going left to right is the x -axis, as in Fig. 3.16 b). The screws can obviously

be turned clockwise or counter, so a convention needed to be created to distinguish the tilt. Turning either the x-axis or y-axis tilt screw to the left (clockwise if viewed from above) moves the side of the set-up closest to you *down*. A counter clockwise rotation would tilt the experiment *up*, as seen in Fig. 3.16 a).

Now that the orientation is established, we determine how bubbles move when changing the tilt *up* or *down*. In order to do that, we want to level the system as much as possible and determine the deviation from being flat. In Sec. 3.2.1 we check how flat the glass plate is, whether there is any pinning due to roughness and if the bubbles move smoothly in one direction, and that there is no deviations to a straight line due to sagging of the glass plate. We compare our estimates to a theoretical prediction established by Bretherton and others [45, 46, 47, 48] in Sec. 3.2.2.

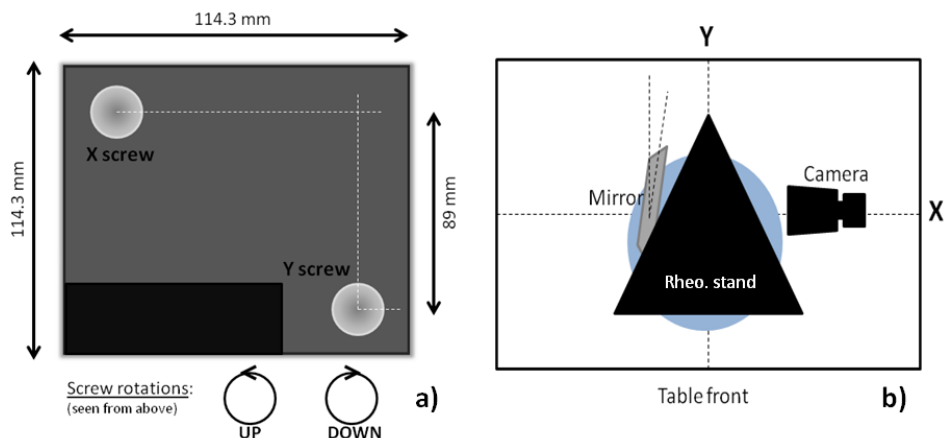


Figure 3.16 – Schematics of the screw platform used for leveling the system, as well as the table top where the set-up sits on. a) A top view schematic of the tilt platform screw layout. A counter clockwise turn (seen from above) of either the X or Y screw turns the platform *up*. Clockwise turns it *down*. The dish with the bubbles is mounted on top of the tilt platform. b) Top view of the table. The tilt platform schematic and its actual orientation as seen when sitting in front of the set-up.

3.2.1 Protocol to Level

We create a protocol with which we probe different tilts on a single bubble under the glass plate. By looking at the motion we can then determine the direction of the bubble, if it moves in a straight line or deviates due to unevenness of the glass, and its velocity. We systematically change the

angle to create a velocity vector field of the bubble. The point where the velocity approaches zero gives us the best estimate where the tilt is minimal.

We start the experiment with a single bubble under the glass plate. This bubble is roughly 5 mm in diameter, larger than the largest bubble we use in our bidisperse packings for the bulk compression experiments. The larger the bubble, the more sensitive it is to changes in the tilt. The bubble is not allowed to touch the boundaries of the cell, since we are interested in its free movement due to the tilt.

To start, some initial tilt settings for the axis were chosen around which we change the tilt. These are:

$$X : 6.5\text{ mm} + 20/50\text{ mm}$$

$$Y : 7.5\text{ mm} + 49/50\text{ mm}$$

Here the notation $XX/50\text{ mm}$ means that the tilt is at the XX 'th tick out of 50 of the screw. These values are the fine-tuned adjustments we make to the tilt of the set-up.

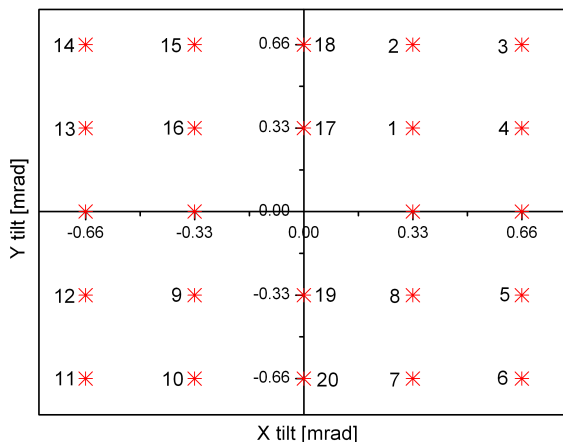


Figure 3.17 – A grid showing the tilt coordinates probed as red stars. The center of the grid is the arbitrarily chosen initial tilt position. Moving along the positive x - or y -axis is *up*. Going into the negative ranges of the axis is *down* when turning the tilt screws. The numbers next to each star show in which order we changed the tilt. All points along the x -axis were done separately. This protocol produced Fig. 3.19.

We proceed by systematically changing the tilt according to a grid, see Fig. 3.17. Here we probe the tilt in steps of three ticks (0.33 mrad) in either x - or y -direction. Three ticks are chosen since this causes the bubble to move enough in the 10 minutes we record the movement with the camera.

Once the time is up, we change the tilt to the next position on the grid and start filming again.

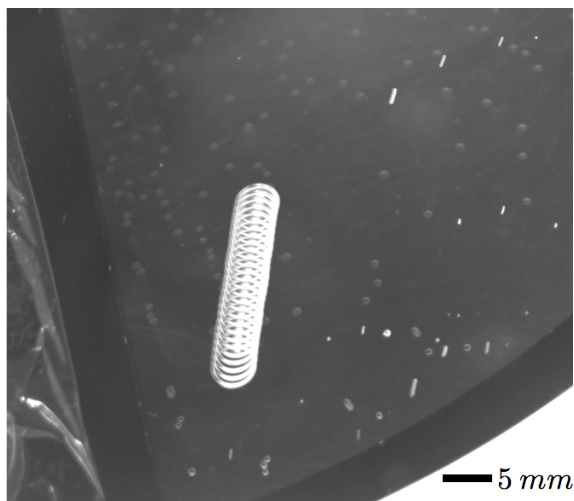


Figure 3.18 – A superposition of images to show a bubble moving in a straight line under the glass plate. The bubble is roughly 5 mm in diameter. The whole track movement is 1780 sec long, 80 sec between each white ring seen in the figure.

We ensure that the bubble does in fact move in a straight line, that the glass plate is without unevenness or local rough patches due to the grinding and polishing process described in Sec. 3.1.1, unlike what could be seen in Fig. 3.5 b). By analyzing the tracks (a track being the bubble movement due to an imposed tilt) of the bubble through the video images, we can convince ourselves that the bubble always moves in a straight line from the beginning of the imposed tilt until we change the tilt, as in Fig. 3.18.

Once all points on the grid have been covered we use ImageJ to piece together the tracks the bubble has traced out under the glass plate to measure the velocity. This can be seen in Fig. 3.19 and Fig. 3.20. We notice that several smaller bubbles in the set-up become pinned and do not trace out the full track, the way the big bubble does. The fact that most of the satellite bubbles do follow the same track shows us that the plate is very smooth.

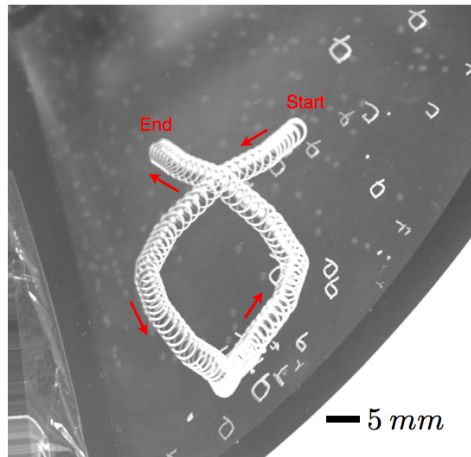


Figure 3.19 – A superposition of the first 16 points in the grid of Fig. 3.17. The time between each ring is 100 seconds. The bubble is roughly 5 mm in diameter. The image has been corrected for skew. By chance this ribbon-like bubble path was created. The start is the top right position, the end is the top left position.

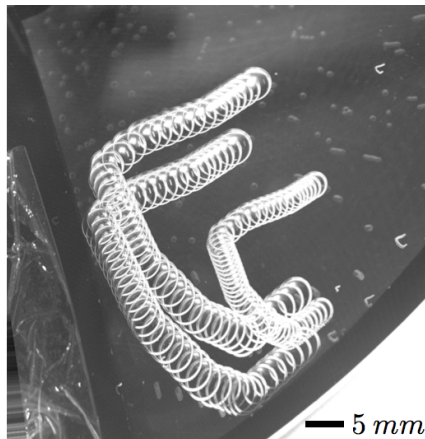


Figure 3.20 – A superposition of three bubbles under the glass plate. The time between each ring is 10 seconds. The two larger bubbles at the top are roughly 5 mm in diameter. The image has been corrected for skew. The start of the imposed tilt is at the top. The bubbles end up at the bottom. The smoothness of the glass plate is again highlighted by the much smaller bubbles also following the tilt motion of the glass plate.

3.2.2 Equilibrium Coordinates

We take the first and last image for any straight section of a track at a fixed tilt and find the center-point coordinate of the bubble. Knowing the time for each track and the coordinates, we can calculate the x- and y-velocity components for all points in Fig. 3.17, (v_x, v_y) . The result is shown in Fig. 3.21. The arrows show the magnitude and direction of the velocity of the bubble drift. The value of the velocity for each tilt as a function of the tilt is plotted in Fig. 3.22. In this case, the length of the arrows is increased by $100\times$ to show their direction.

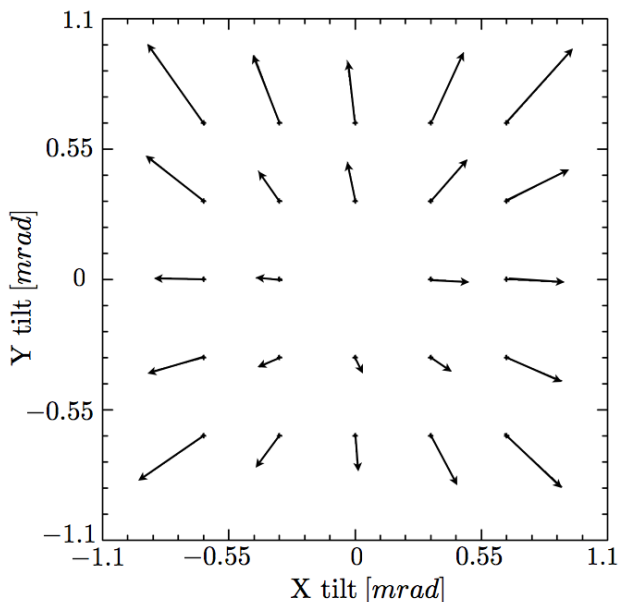


Figure 3.21 – The velocity profile of the bubble at different tilt positions given by Fig. 3.17. As expected, the velocity is larger when the tilt is greater.

From the figure we note that our initial tilt settings are fairly good estimates of where zero tilt is, since all velocity vectors seem to originate at our initial setting. They are, however, not quite emanating from $(0, 0)$. We want to determine their origin position, (x_0, y_0) , as the tilt coordinates should be for a completely level system.

We define the directional vector from our to-be-determined origin where the tilt is zero, \hat{r} , to the coordinates that correspond to points picked for each tilt in Fig. 3.17. Here

$$\hat{r} = \frac{\begin{pmatrix} x-x_0 \\ y-y_0 \end{pmatrix}}{\sqrt{(x-x_0)^2 + (y-y_0)^2}} \quad (3.2)$$

where the denominator is the length of the vector from (x_0, y_0) to (x, y) and can be seen as an angle between the origin and (x, y) .

The drag force (per unit length) on a bubble under a glass plate is related to its velocity by Bretherton's law as set forth in [47] $F = 4.70\sigma(Ca^*)^{\frac{2}{3}}$, where $(Ca^*) = \frac{\eta v}{\sigma}$ is the bubble-wall capillary number. Equating this with the buoyancy force a bubble of radius R feels under an inclined plane of tilt angle θ , $F = \frac{4}{3}\pi R^3 \rho g \times \sin \theta$, we can get the velocity of the bubble as a function of the tilt of our glass plate. Note that the force in the buoyancy equation is linearly proportional to the angle of tilt. If we now dot the velocity vector for every tilt, $\vec{v} = (v_x, v_y)$ in to \hat{r} , and plot this versus the angle, we can vary our estimated coordinates of (x_0, y_0) to collapse all the data as much as possible.

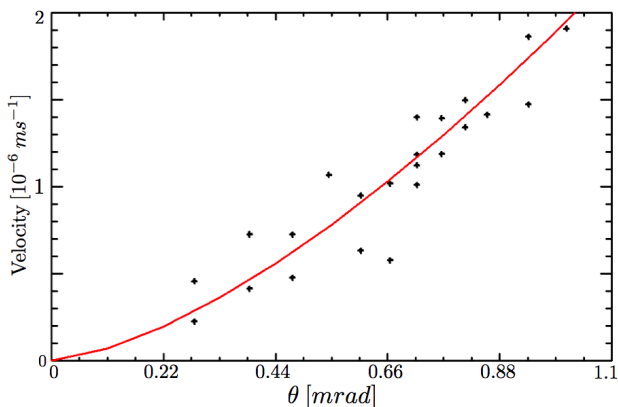


Figure 3.22 – The velocity of a bubble moving under the glass plate versus the tilt. The line of best fit is in red.

If we calculate numerically the relation between the velocity as a function of the tilt, as described above, we get

$$v = 0.065 \text{ ms}^{-1} \times \theta^{1.5} \tag{3.3}$$

The line of best fit in Fig. 3.22 is $v = 0.07 \text{ ms}^{-1} \times \theta^{1.5}$, in excellent agreement. By only knowing the buoyant force and the velocity of a bubble under our glass plate, Fig. 3.22 shows that our bubbles are behaving like the ideal case proposed by Bretherton [45] of a bubble sitting under a flat plate.

3.3 Compression Protocols

In this section we describe the compression protocols we use to probe the jamming transition in our two-dimensional foam packing. The main idea is to compress the foam, trapped in the wedge of our set-up, by small, incremental strain steps and to measure its elastic response. The steps can be anywhere between $0.5 - 12 \text{ mrad}$, which for typical wedge openings in the order of 1 rad corresponds to strains between 5×10^{-4} and 10^{-2} . As we will see in Fig. 3.26, the stress responds on a timescale of several minutes, and we choose relaxation times of the system between these steps from $400 - 1200$ seconds. We will show which combinations of step size and relaxation time give a well equilibrated response and thus allow us to measure the elastic moduli of the foam.

In Sec. 3.3.1, we show the difference between the angle measured by the rheometer and the open angle, measured by image analysis. Sec. 3.3.2 discusses the dynamics of the system and how by controlling the compression and sit times of the experiment, we ensure that the system is equilibrated. In Sec. 3.3.3 we give a detailed description of the different compression protocols used.

3.3.1 Deflection Angle vs. Open Angle

For all experiments, the open angle of the wedge and the deflection angle imposed by the wiper on the packing are of great importance. However, there are differences in obtaining and also in using these two in the data analysis.

The deflection angle, θ , is the angle that the rheometer tells the wiper to move and change between protocols, as shown in Sec. 3.3.3. The starting point is arbitrarily set by the rheometer, meaning wherever the wiper sits at the start of any experiment is the designated reference point. Each subsequent step is measured from that reference point. For the protocols outlined below, only this deflection angle is used to compress the foam.

The open angle of the wedge geometry, θ_0 , is measured using ImageJ. By using the images of the foam after each compression step, we measure the angle between the static wall and the wiper. This allows us to calculate the area of the wedge during the entire run, which will be of use in the next chapter.

3.3.2 Dynamics of Different Protocols

These steps are characterized by three quantities: the change in angle between steps, $\Delta\theta$, the change time between steps, t_c , and the sit time at an angle, t_s . In all protocols, the wiper sits at one imposed angle before moving to the next one at a finite rate, as shown in Fig. 3.23. The change in angle, $\Delta\theta$, and t_c are the same for all protocols outlined below, only t_s is changed between different protocols. In our experiments, we use the rheometer in strain controlled mode, and during the step-wise compression, the torque from the bubbles on the wiper is measured.

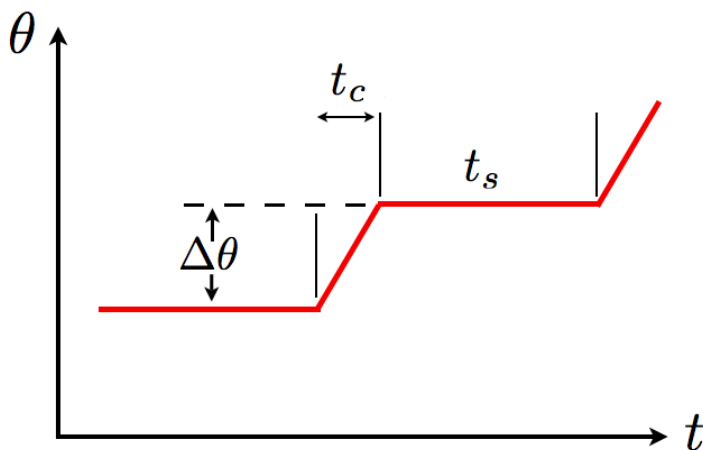


Figure 3.23 – Sketch of the deflection angle versus time. The wiper moves linearly by a change in angle $\Delta\theta$ over time t_c to the new angle, where it sits for time t_s .

We choose $t_c = 120$ seconds. The corresponding finite rate of change in angle prevents dynamic effects to dominate, such as the creation of little satellite bubbles in Fig. 3.6 a). Moreover, this rate is slow enough for the system to quasi statically move to be compressed; shorter t_c disturbs the packing too much and in that case it takes the system far longer to reach an equilibrium during the sit time.

To allow the system to equilibrate after each compression step, we keep the wiper fixed for a duration t_s . Typical equilibration times, seen from the torque signal, range from several minutes for low compressions, like in Fig. 3.24 a), to tens of seconds for higher compressions, as in Fig. 3.24 b).

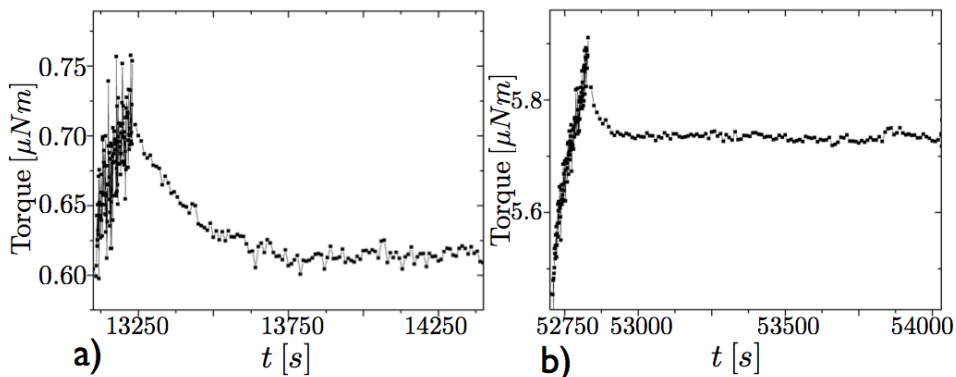


Figure 3.24 – a) At lower torques, equilibration times can be several minutes. b) At higher compressions, equilibration happens much faster, over several tens of seconds.

For low compressions, rearrangements become more frequent, and depending on protocol, we take t_s anywhere from 400 to 1200 seconds, allowing the system to equilibrate.

3.3.3 Stress vs Strain Control

The wiper, which makes up the third edge of the wedge in which the foam packing sits, see Fig. 3.1, is attached to a shaft which is rotated by a rheometer. As mentioned in Sec. 3.1.1, the rheometer can be used in strain and stress controlled mode. We only use strain controlled mode, since the system relaxes faster than when using stress controlled protocols. Fig. 3.25 shows the difference between equilibration times for strain and stress controlled protocols. The difference between the two modes is astonishing: packings compressed using the strain controlled mode of the rheometer equilibrate within minutes (or even faster if very compressed), see Sec. 3.3.2 above, whereas for stress controlled mode, as in Fig. 3.25 b), the packings sometimes do not equilibrate at all.

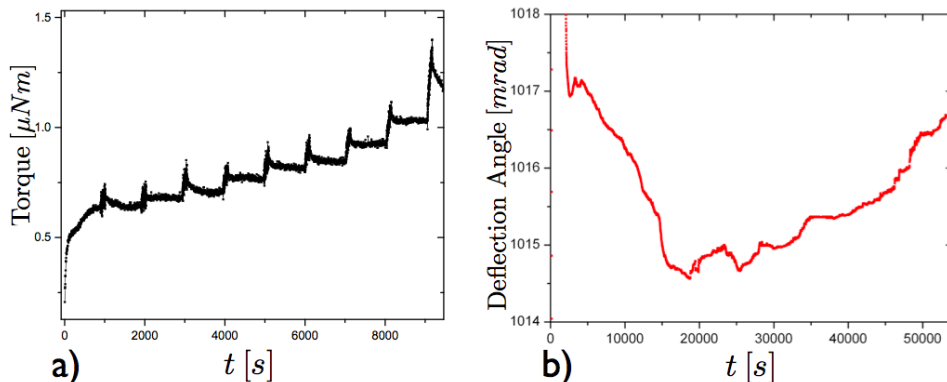


Figure 3.25 – a) A zoom-in of a well equilibrated compression protocol using the strain controlled mode of the rheometer. b) A signal of the wiper compressing a sample in stress controlled mode over 15 hours. The rheometer measures the change in angle when a constant torque is imposed. Note how the system never equilibrates over the course of the imposed stress.

3.3.4 Protocols

We have explored three different strategies for leveling the system. Initially, we aimed at leveling the top plate to the best of our abilities: we call this the “flat” protocol. Then, we added a tiny but controlled tilt to the system, and oriented the tilt such that a hole formed in the foam close to a corner of the system: the “corner-hole” protocol. Finally, we settled on a protocol where the tilt is oriented such that gravity is approximately perpendicular to the wipers orientation, leading to a long stretched-out hole near the wiper: “slice-hole” protocol. Most data presented in the following chapter are obtained in the slice-hole protocol.

3.3.4.1 Flat Protocol

The first problem one encounters in experiments on 2D foams below a top plate is the strong sensitivity on the residual tilt of this plate. The most natural approach is thus to level this top plate as well as possible, thereby reducing to the minimum the effect of buoyancy, which leads to drift of free bubbles. However, once one approaches the (un)jamming transition, a hole spontaneously forms somewhere near the boundaries. The hole’s precise location is set by the orientation of the residual tilt. This hinders the interpretation of the jamming behavior in our foams. Nevertheless, for more strongly compressed foams such problems do not arise, and below, we describe the outcome of some of these explorations.

In Fig. 3.26 we used the flat protocol and probed almost two decades in torque, carefully staying away from the very low compression regime. Once the cell was loaded with bubbles, we lightly compressed the packing with a low torque of about $2 - 3 \mu Nm$ to make sure all bubbles were in the wedge-shaped area. We turned off the torque and let the system relax and set the deflection angle of the wiper to constant, once we visually determined the packing to be stable and the torque signal to be sufficiently low. At this point we started the compression. The imposed deflection angle went (in *mrad*):

$$0, 0.5, 1, 2, 3, 4, 5, 6, 7$$

and then in steps of root two. After each step of root two, which we call the compression step, there was a “measurement” step, which is 1 mrad more compressed, see Fig. 3.26.

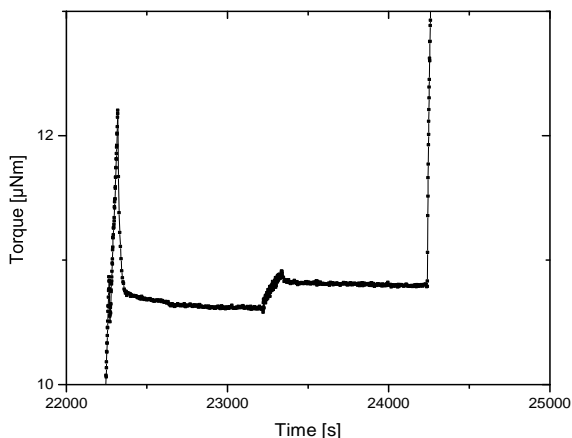


Figure 3.26 – A compression step followed by its measurement step, which is 1 mrad more compressed, used in the “flat protocol”. The sit time for each step is 900 seconds.

The final deflection angle was 190 mrad from the start point. The sit time at every angle was 900 seconds and the wiper changed angle linearly to the new angle in 120 seconds. The total strain range for this experiment was 24%, which for this system corresponded to a range of torque probed between $\lesssim 0.5 \mu Nm$ to $75 \mu Nm$. Fig. 3.26 shows full equilibration.

Although successful, we abandoned this flat protocol because it did not allow us to get very close to jamming. For the lowest torques, a hole would open up in the foam packing, and the interpretation of the results

was somewhat opaque; in particular, it was now unclear where precisely the jamming transition takes place.

3.3.4.2 Corner Hole Protocol

To control the location where the hole appeared when uncompressing the foam, we tuned the top plate so that it deviated from the horizontal by an angle of order 0.33 mrad , and orientated this residual tilt so that the hole in the foam opened up in a corner of the foam, see Fig. 3.15 b).

While this protocol allowed us to control the location of the hole, its location was such that a relatively large change in the wipers location was necessary to open or close the hole. Moreover, we observed that there was bridging in the foam right before the hole closed. The bubbles would move to close the hole. Before it could be enclosed completely by the wiper, the remaining bubbles at this point created a bridge, leading to higher than normal torque signals until the bridge disappeared due to a rearrangement only many steps later.

In Fig. 3.27 we show an example of such a run, performed for compression steps of 1 mrad and sit time 400 seconds. We compressed a system with this type of hole for four different tilts of the glass plate, each time increasing the tilt by 3 ticks (0.33 mrad), tilting the glass plate a total of 1.32 mrad . The bridge can be seen in Fig. 3.27.

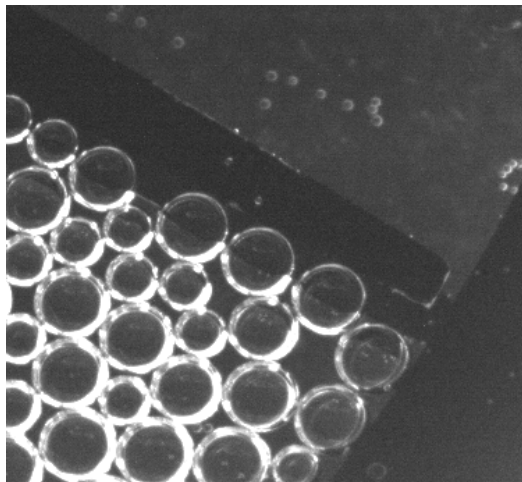


Figure 3.27 – A pentagon arrangement of bubbles at the tip of the wiper during the “corner hole” protocol. This bridging happened repeatedly and with too many bubbles being in contact with the wiper at the start of an experiment led to us to abandon this protocol for the “slice hole” protocol.

We were thus not compressing the system fully, just measuring the response of the bridge. Also, the shorter sit time we used for this protocol showed that we were not letting the system relax long enough: the trend of the signal showed many times that the foam had not reached a relaxed state.

3.3.4.3 Slice Hole Protocol

This protocol also uses a controlled tilt, now orientated so that the wiper lies parallel to the packing when a hole is formed; the slice hole ensures that there is no initial contact between the packing and the wiper. Ideally, the wiper closes the hole and makes contact with the sample at the same time along the length of the wiper; in practice we have limited control over the precise orientation of the tilt (as the absolute tilt angle is already very small), but we can orientate the tilt sufficiently well so that bridging is essentially absent. An example of the final configuration of the hole is shown in Fig. 3.15c). This protocol yielded the clearest difference in torque signal between the gravity and the boundary jammed regions, and will be used in the following chapter.

Jamming of a 2D Foam

In this Chapter, we probe which aspects of the jamming transition can be observed in 2D foams. We do this by measuring the torque and occupied area as function of the opening angle of the wedge geometry, and image the organization in the foam. At the jamming point the material is singularly fragile, and the tiniest effects, unavoidable in experiment, may affect the behavior observed. In particular, prior simulations on the jamming of soft particles [12] have focused on *(i)* absence of bulk forcing (like gravity) *(ii)* large systems with periodic boundary conditions, and *(iii)* strictly linear response. Our experimental system deviates from these idealizations in important aspects.

First and foremost, any symmetry-breaking field, such as a residual gravitational pull, will strongly disturb the unjammed state. What consequences does this have for the nature of the transition that we can observe in experiments? In our 2D experiments, *any* tilt of the top plate will lead to drift of the bubbles, which will continue until they reach a boundary. It is impossible to create an initial packing configuration where no bubble touches its neighbor. Therefore, the classical picture of the unjammed state of separated particles is not reachable in experiment. The tilt in our system is unavoidable, and we cannot go "through" the jamming transition as in Fig. 2.3 in Sec. 2.1. However, a carefully study of the effect of a weak tilt reveals that we can observe a transition between an extremely weak, gravity jammed state, and a more strongly compressed boundary jammed state.

Secondly, our systems are not infinite and have real boundaries. These play an important role in confining the foam, and stopping the drifting motion of the bubbles due to the residual tilt. As we will see, they also may lead to the formation of arches: local configurations of bubbles that

can carry a load, despite the presence of a hole in the foam nearby.

Thirdly, we cannot guarantee linear response. Can we extract meaningful response data from our system near the transition? Most of the theoretical work on jamming has focused on linear response, this being either calculated in strict linear order (by linearizing the equations of motion and using objects like the dynamical matrix to calculate the response of a jammed system to external, infinitesimal forcing), or by using tiny deformations. Deformations in the order of 10^{-8} are not unheard of, yet these are completely inaccessible in our experiments. Recent work [49, 50] shows that the range of validity of linear response vanishes near the jamming point, or for large systems. Both are intuitive: near jamming, the system “falls apart” so the smallest forcing may drive the system towards nonlinear, irreversible events. And the larger the system, the greater the probability that somewhere, the system is about to fail locally, again leading to nonlinear, irreversible events. We therefore should be very cautious in interpreting our experimental data, in particular close to the critical point.

The data we will present here shows that the experimental issues do not overwhelm our signal; temperature drift is small, coalescence events sparse and easily identifiable in our data. Moreover, our measurements are sensitive enough to access essentially linear response. The most important issues have to do with the tilt and the presence of boundaries.

It is helpful to define the wedge area here before continuing. Using the open angle, θ_0 , obtained through image analysis (see Sec. 3.3.1), the area of the wedge geometry over the course of any given experiment is then just $A_W = \frac{\theta_0}{2} r^2$, where r is the length of the wiper.

As we will detail below, for densely packed systems (small A_W), the torque T systematically grows when A_W is lowered, while for very loose systems (large A_W), the torque T becomes essentially constant at a small value. However, this is *not* yet evidence for the classical, sharp (un)jamming transition. When we try to unjam the system by gradually increasing the area available for the foam (by increasing the open angle θ_0 , or conversely, the wedge area), instead of losing contact, the bubbles will simply drift to one part of the system, creating a “hole” at one side of the bubble packing – we say that the system then goes from a boundary jammed to a gravity jammed state, as was introduced in Sec. 3.2. As a consequence, we will find that $T(A_W)$ often does not show a sharp transition, and even if it does, it may not coincide with the “closing of the hole” in the foam.

To further understand what is going on, we also measured the area occupied in the wedge by the hole, A_H (introduced more formally in Sec. 4.2.2) and the foam, where $A_F = A_W - A_H$. When we then plot $T(A_F)$, we

do find a clear and sharp transition, providing strong evidence that the bulk modulus discontinuously jumps from a finite value to zero when going through the (un)jamming transition.

While we do not have direct access to the shear modulus, we do find that if we deform the foam where A_W is large and there is a large hole in the foam, this does not cost any measurable energy. In such a case, the foam area remains constant, so that the deformations are shear-like. The system is then still very weakly jammed (by gravity), but the absence of a significant response suggests that the shear modulus is close to zero. This suggests that when approaching the transition from boundary to gravity jammed, the ratio G/K is very small.

This chapter is organized as follows. In Sec. 4.1 we discuss the elastic response in a wedge, and show that the elastic constant we can measure is equal to $G + K$. In Sec. 4.2 we extract the values of the torque to which the system equilibrates after each wiper step. We also introduce how we measure A_W , A_H and finally A_F . Lastly, in Sec. 4.3, we study in detail the relation between T and A_F and find clear evidence of a sharp transition between boundary jammed and gravity jammed states. Experiments with higher tilts are also investigated, as is the affine response of the foam under high compression in the boundary jammed regime in Sec. 4.4.

4.1 Elastic Response in a Wedge

To interpret our experimental data, we need to consider the elastic response of a linear bulk material in a wedge geometry first, and in this section we derive this response from a purely theoretical perspective. Since the set-up uses a rather un-classical way to compress an elastic system (arguably a more classical case would be a square under compression), we need to understand what kind of forces are acting on the foam in the wedge. After obtaining the general result, we then translate it to our specific experimental geometry.

It is easiest to consider the stresses and strains in the compression set-up using polar coordinates (r, θ) .

The stress strain relations then are as follows [51]:

$$\begin{aligned}\gamma_{rr} &= \frac{1}{E}(\tau_{rr} - \nu\tau_{\theta\theta}), \\ \gamma_{\theta\theta} &= \frac{1}{E}(\tau_{\theta\theta} - \nu\tau_{rr}),\end{aligned}\tag{4.1}$$

where ν is Poisson's ratio and E the Young's modulus of our foam. We have also introduced the stress components τ_{rr} and $\tau_{\theta\theta}$ acting in the radial and θ -direction, respectively. All off-diagonal components of the strain matrix, $\gamma_{r\theta}$ and $\gamma_{\theta r}$, are 0.

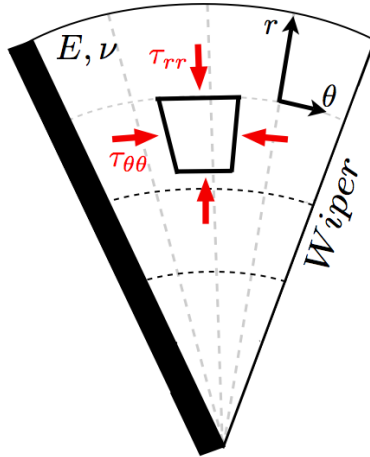


Figure 4.1 – The strain and stress for an elastic material with Young's modulus E and Poisson's ratio ν acting on an area element in the wedge.

Assuming a homogeneous deformation (which is a good assumption at large enough scales), we find that $\gamma_{rr} = 0$. Hence

$$\begin{aligned} \gamma_{rr} = 0 &= \frac{1}{E}(\tau_{rr} - \nu\tau_{\theta\theta}) \\ \Rightarrow \tau_{rr} &= \nu\tau_{\theta\theta} \end{aligned} \tag{4.2}$$

$$\begin{aligned} \gamma_{\theta\theta} &= \frac{1}{E}(\tau_{\theta\theta} - \nu\tau_{rr}) \\ \Rightarrow \gamma_{\theta\theta} &= \frac{1 - \nu^2}{E}(\tau_{\theta\theta}). \end{aligned} \tag{4.3}$$

We find the following identity:

$$\frac{\tau_{\theta\theta}}{\gamma_{\theta\theta}} = \frac{E}{1 - \nu^2} \tag{4.4}$$

We now use the well known relations between ν and E on the one hand, and the shear (G) and bulk (K) modulus in 2D [52]:

$$G = \frac{E}{2(1 + \nu)}$$

and

$$K = \frac{E}{2(1 - \nu)}$$

We notice that, by using a linear combination of the two moduli, we get from Eq. 4.4

$$\frac{\tau_{\theta\theta}}{\gamma_{\theta\theta}} = \frac{E}{1 - \nu^2} = \frac{E}{2(1 + \nu)} + \frac{E}{2(1 - \nu)} = G + K \quad (4.5)$$

This equation tells us that we are not only purely compressing our foam sample, but that there is a shear component in our geometry as well. This is typical for the sort of uniaxial compression we do, and for this specific geometry, Eq. 4.5 gives the precise relation. For further reference, we will refer to the combination $G + K$ as the *wedge modulus*, W .

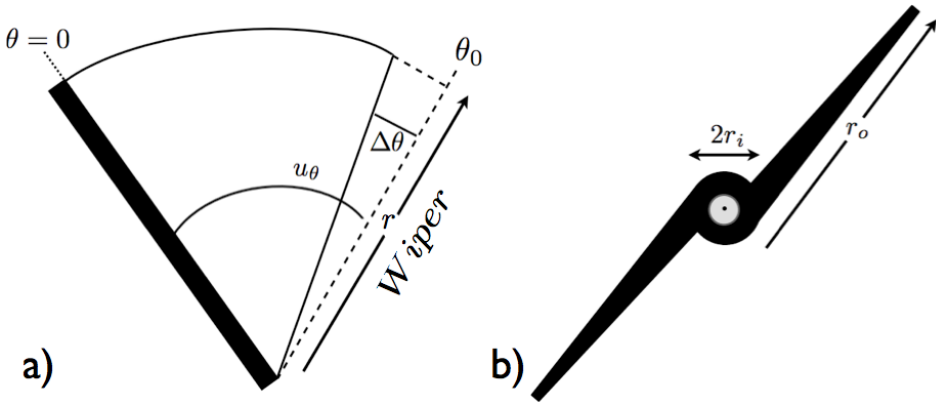


Figure 4.2 – a) Schematic of a small compression $\Delta\theta$ from some start angle, like is defined in Fig.3.23. The angular displacement, u_θ is shown along the open angle θ_0 . In b) a schematic of the wiper dimensions is shown.

We now need to relate our experimental accessible quantities to the wedge modulus W . To do so, we will calculate the stress and strain, $\tau_{\theta\theta}$ and $\gamma_{\theta\theta}$, given the torque, geometrical parameters r_i , r_o and θ_0 and the change in angle $\Delta\theta$, see Fig. 4.2, where we consider an infinitesimal compression $\Delta\theta$ of our compression geometry. The angular displacement component is (the radial component being 0):

$$u_\theta(r, \theta) = -r\Delta\theta\frac{\theta}{\theta_0} \quad (4.6)$$

From elasticity theory we consider the definition for $\gamma_{\theta\theta}$ according to [52],

$$\gamma_{\theta\theta}(r, \theta) = \frac{1}{r} \frac{\partial u_{\theta}}{\partial \theta} = \frac{-\Delta\theta}{\theta_0} \quad (4.7)$$

The wiper in the set-up has an effective length, $(r_o - r_i)$, where r_o is the outer radius of the wiper, from center of rotation to the tip, and r_i is the inner radius by its fulcrum, as seen in Fig. 4.2 b). The normal stress $\tau_{\theta\theta}$ due to the compression of the wiper can easily be related to the torque as

$$T = \int_{r_i}^{r_o} -\tau_{\theta\theta} r dr = -\frac{1}{2} \tau_{\theta\theta} (r_o^2 - r_i^2) \quad (4.8)$$

Rearranging Eq. 4.8 and making use of Eq. 4.7, we get

$$\frac{\tau_{\theta\theta}}{\gamma_{\theta\theta}} = \frac{2\Delta T \theta_0}{\Delta\theta (r_o^2 - r_i^2)} = G + K = W, \quad (4.9)$$

which gives the wedge modulus for our geometry and where $r_o = 1.75 \text{ cm}$ and $r_i = 10.75 \text{ cm}$. We note here that this relation assumes that the strain fields are of the forms given by Eq. 4.7, which is only true in the boundary jammed regime.

4.2 From Gravity to Boundary Jammed States

In order to probe the nature of the jamming transition, we will first probe the variation of the torque T as function of the wedge area, A_W . As we have already discussed above, the appearance of holes in the foam necessitates us to also measure the area of the hole, through image analysis.

In Sec. 4.2.1 we show how we extract the torque value to which the system equilibrates after each step of the wiper. Additionally, we define the wedge, hole and foam areas for our experiments in Sec. 4.2.2, and how we measure these experimentally, before applying them in the next section.

4.2.1 Determining $T(\tau_2)$

Here we show how we extract the torque value to which the system equilibrates after a deflection angle step in θ has been done – this is not trivial as the foam slowly relaxes.

Controlling the steps in deflection angle with the protocol discussed in Sec. 3.3.3, a typical torque signal as function of time for an entire run is

shown in Fig. 4.3 a). Clearly, once the wiper has moved to compress the foam sample (recall the time to move into a new angle is $t_c = 120$ seconds and the sit time is $t_s = 1200$ seconds), the torque overshoots and then relaxes to its ultimate equilibrium value, as seen in Fig. 4.3.

We believe that the overshoot partially comes from the wiper initially pushing against the drag of the bubbles with the top plate.

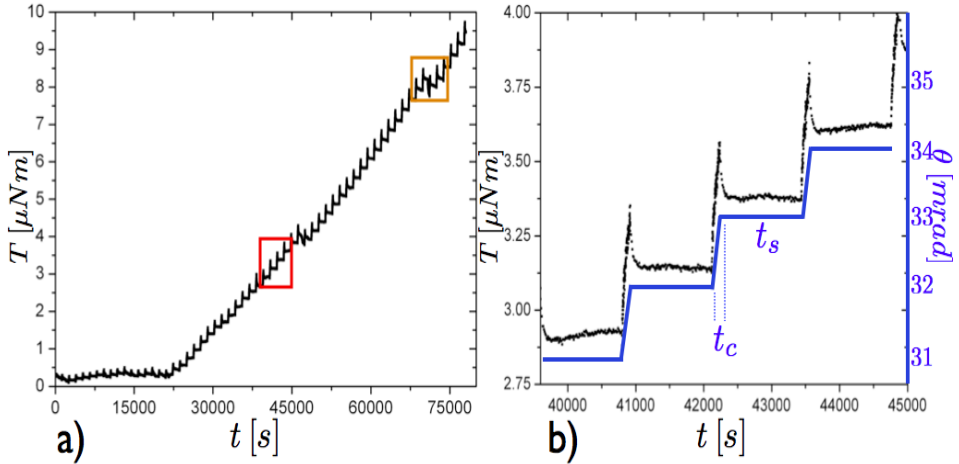


Figure 4.3 – a) A typical torque vs. time profile output by the rheometer using the slice hole protocol. b) A zoom of the same signal (red box in a)) highlights the overshoot and equilibration after compression steps θ , which are sketched in blue.

The relaxation of the signal can be complicated. This can already be seen in Fig. 4.3. Sometimes, the torque signal becomes essentially flat after the initial overshoot, but often we observe a slow drift. We say that the sample is drifting if it does not seem to equilibrate. In some cases, rearrangements occur. Moreover, as seen in Sec. 3.1.2, the packing can have coalescence events, especially under high compression, or if the sample is old, which adds to the drift. In Fig. 4.4 a coalescence event is the culprit.

These occasional “glitches” create scatter in the data and prevent the system from coming to an equilibrium during t_s . These data points are usually included anyway in the analysis because they are scarce and not always easy to identify in an objective manner.

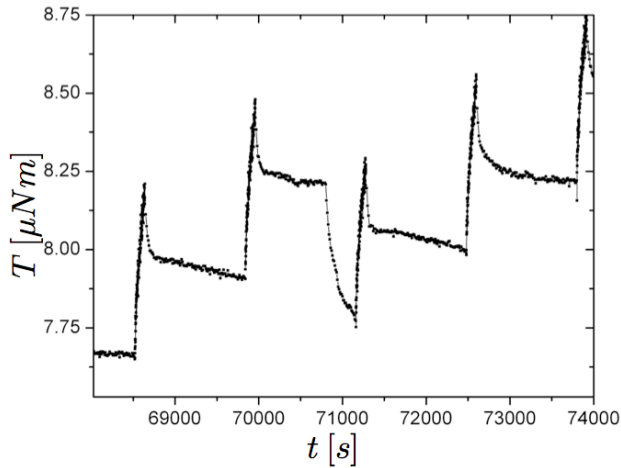


Figure 4.4 – A coalescence event causes a “glitch” in the data, which is taken from the orange box in Fig. 4.3 a). Glitches create scatter in the data.

All these complex effects necessitate a careful handling of the $T(t)$ data. The first step in analyzing the torque profile, $T(t)$, is to extract the best estimate for the value to which the packing equilibrates after the compression step. To capture both the plateau and the drift in $T(t)$, we perform linear fits to $T(t)$. We disregard the first 12% of data points in the fit to avoid having to fit a combination of an exponential and linear curve to the profile. We choose 12% since in this amount of time, the majority of relaxation occurs after the wiper has compressed the sample to the new angle. We are most interested in the relaxed, plateau portion of the torque signal (as can be seen in Fig. 4.3b)), since it tells us whether that particular step has reached an equilibrium after the compression. We define torque values at the start-point of the fits as τ_1 and at the end-point as τ_2 . These definitions will be used later.

We use the least-square curve fitting routine in IDL called MPFIT-EXPR. This routine needs a set of inputs in the form of starting points in the parameter space. Additionally, it needs a model type equation, to which these parameters can be fit. We use a simple linear fit of the torque with an offset such as $T = a + bt$, where a is the offset, b is the slope and t is the time. With an estimate of starting point values, MPFITEXPR makes a linear fit to the relaxation profile and gives the torque value at the initial and final point of the fit curve, as well as the slope over the step time, see Fig. 4.5.

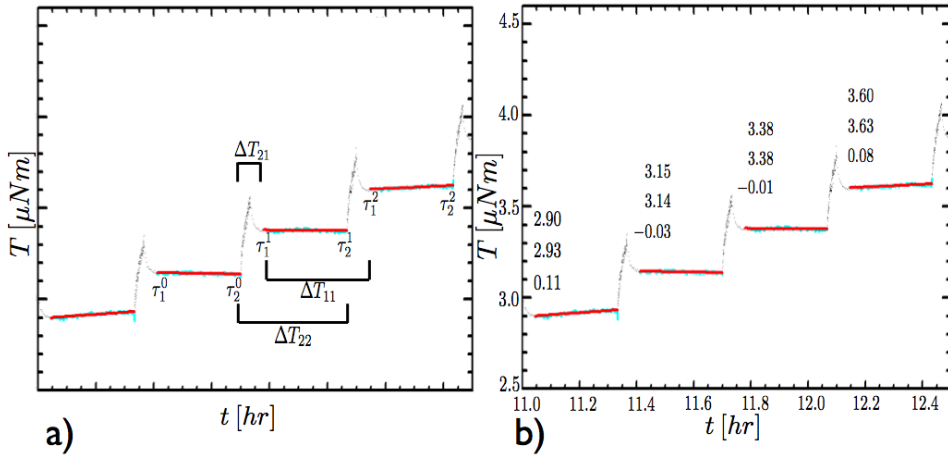


Figure 4.5 – a) Definitions of ways to calculate the change in torque between compression steps. The fit’s start and end points, τ_1^i and τ_2^i respectively, are used to extract ΔT for a series of compression steps. $i \in [0, 50]$ is the number of the compression step. b) A set of linear fits with the same data as used in a) made in IDL by using the MPFITEXPR routine. Shown above each fit, from top to bottom, is the data point at the start of the fit and the last point of the fit (in $[\mu Nm]$), and finally the slope of the fit-segment (in $[\mu Nm/hr]$).

The slope value, b , provides valuable information on whether that step is well equilibrated. The closer the value to 0, the flatter the relaxation profile and thus the more equilibrated that step.

We extract the change in torque between steps by making a linear fit to the relaxation profile. We compare the last point of the fit, τ_2 , in one step to the first point of the fit, τ_1 , in the next compression step. This gives us the change in torque, ΔT_{21} , defined in Fig. 4.5 a). But why choose ΔT_{21} and not ΔT_{11} or ΔT_{22} ?

Choosing ΔT_{21} gives less noise than the other choices because we suppress the drift. If we chose ΔT_{11} , the entire profile of τ_1^1 to τ_2^1 could be drifting, and thus comparing τ_1^1 to τ_1^2 would incorporate this drift. Similarly, with ΔT_{22} we would incorporate the drift, since we would be taking τ_2^1 to τ_2^2 , which could include the possibly not-equilibrated step of τ_1^2 to τ_2^2 . It becomes clear that even if there is drift during a step, ΔT_{21} just compares the last point of the fit to the first point and excludes any effects due to drift.

The purpose of the end-point torque values from the fits, discussed in Sec. 4.2.1, $T(\tau_2)$, will become clear in Sec. 4.3.

4.2.2 Determining the Foam Area

In parallel to the torque measurement, we also measure the size of the hole at the end of the sit time, t_s , right before the next step in θ_0 is applied. Each experimental run has a different-sized hole.

We image the packing from above (see Sec. 3.1.4) at 0.033 Hz , starting the filming right when the experiment starts. For each image at the end of t_s , we use ImageJ to outline the edge of the foam, like in Fig. 4.6.

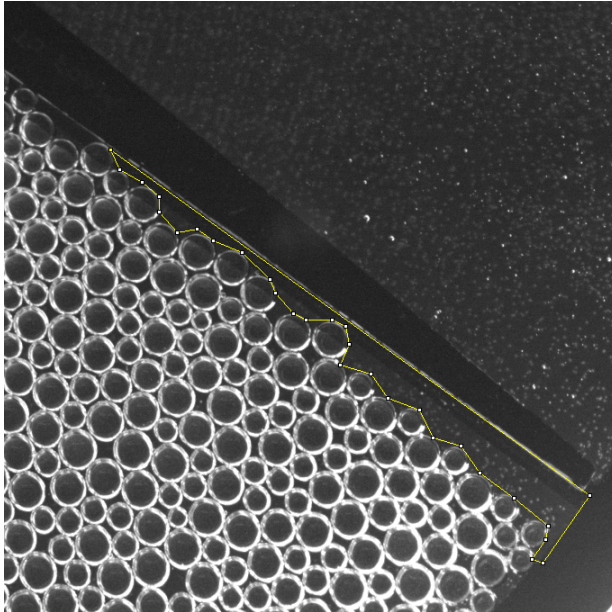


Figure 4.6 – An ImageJ snapshot showing how we draw the outline (yellow) of the hole to calculate the area of the hole.

The idea is that the hole size should go to zero once the sidewall touches the bubbles everywhere, hence we should not count the little areas in between bubbles as “hole”. The measurement of hole area, A_H , is done until the hole is closed, at which point we say, by definition, that $A_H = 0$. The curve (yellow) shown in Fig. 4.6 connects the “tops” of the bubbles, and the hole area will thus vanish when all the bubbles contact the sidewall. In Fig. 4.7 we show an example of the evolution of the hole area with θ_0 . Even though there is some subjective judgment in these measurements, we believe the data shows that the hole areas thus obtained are sufficiently accurate.

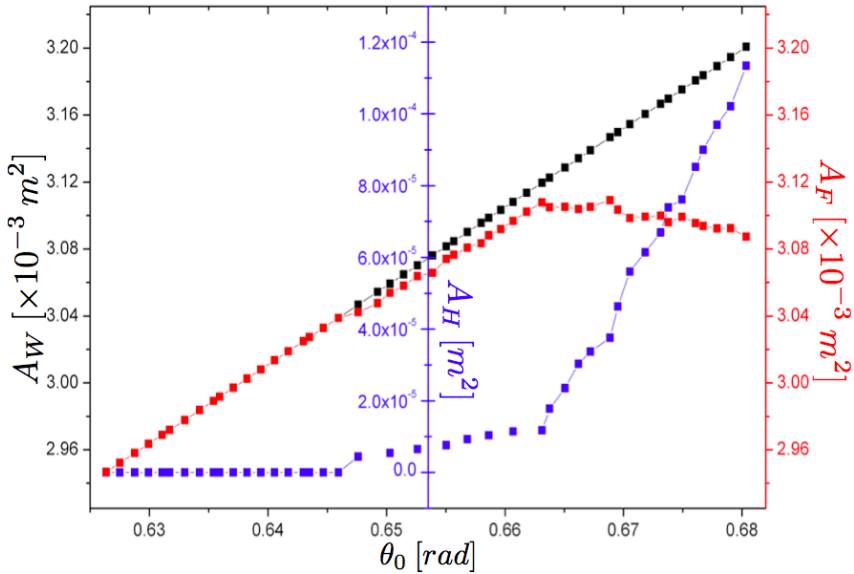


Figure 4.7 – The deflection angle, hole area and foam area, A_W , A_H , A_F , respectively, as a function of wedge area.

The evolution of the wedge area, A_W , versus the deflection angle, θ_0 , is obviously linear as shown in Fig. 4.7. In subsequent sections, we will use A_W instead of θ_0 . Fig. 4.7 shows that A_H slowly decreases as θ_0 is decreased until it vanishes once the angle has become sufficiently small. We finally introduce the foam area as $A_F = A_W - A_H$.

4.3 Results

With the experimental procedure explained above, we can now analyze the equilibrated values of the torque, $T(\tau_2)$ (which will be abbreviated to just T), and the corresponding values of A_H and A_F . In Fig. 4.8 we show the evolution of T , A_H and A_F as a function of A_W , for a run with $t_c = 120$ seconds, $t_s = 1200$ seconds and a controlled tilt of 0.66 mrad such that we are in the “slice hole” protocol.

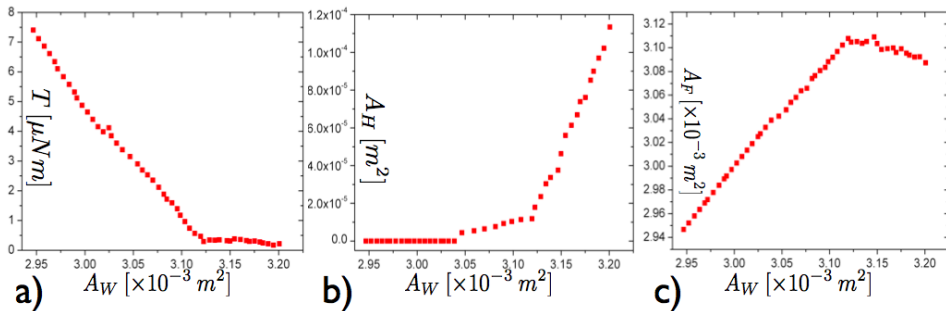


Figure 4.8 – a) Example of torque versus wedge area, A_W . The torque values plotted here are the equilibrium values $T(\tau_2)$ to which the signal relaxes after each compression step. b) The hole area versus the wedge area for the same data set as in a). c) The foam area versus A_W .

The plot of T versus A_W in Fig. 4.8 a) shows a distinct kink for $3.12 \times 10^{-3} \text{ m}^2$. For smaller wedge areas, the torque grows approximately linearly, while for larger wedge areas, the torque levels off at a small value.

This kink would lead one to believe that this is the point at which the hole closes and the system jams. However, as Fig. 4.8 b) shows, the hole in the foam does not close at the same value of A_W . The fact that the system is under finite compression ($T > 0$) whilst forming a hole is surprising. It can be argued that substantial holes are exceedingly rare in packings of frictionless particles; in simulations, such holes are never observed [13]. So what happens here?

A clear inspection of the dependence of the hole areas, A_H and A_F ($= A_W - A_H$), shown in Fig. 4.8 b) and Fig. 4.8 c), in the experimentally controlled wedge area, A_W , shows that one can distinguish three regimes. First, for small A_W (here, $A_W < 3.05 \times 10^{-3} \text{ m}^2$) the hole is fully closed, and the system is clearly compressed. We refer to this as the “boundary jammed” state, informally introduced in Sec. 3.2 above.

Secondly, for large A_W (here, $A_W > 3.12 \times 10^{-3} \text{ m}^2$), the hole area grows rapidly with A_W . In this regime the foam area, A_F , stays roughly constant, so that A_H grows proportional to A_W . The fact that the location of the hole is controlled by the unavoidable tilt of the set-up, we argue that the resultant residual gravitational forces here govern the motion of the bubbles to one side of the system, causing a hole on the opposite side, here close to the wiper. Based on submerged bubble chains in a tube under tilt [42], prepared in the same surfactant solution, we believe attraction between the bubbles (an alternate explanation for the hole formation) to be small. Hence, in this regime the system is not unjammed, but rather weakly jammed by gravitational forces. We refer to this as “gravity jammed”.

Thirdly, in between these two regimes we find a mixed regime. Here a hole has opened up, but it does not grow proportional to A_H . Hence, both gravity and boundaries serve to jam the system, and we refer to this as the “mixed state”. Indeed, we see in Fig. 4.8 a) that the torque is finite and varies with A_W in this regime. Typical hole sizes in this regime are small. We do not fully understand how the stresses are maintained near the hole area, but we suggest that arching plays an important role here.

Taken together, the data in Fig. 4.8 conclusively show that the kink in T does not correspond to the closing of the hole, and is not sufficient to conclude that the system undergoes a sharp transition.

In addition, for many runs, the kink in T is not as distinct as depicted in Fig. 4.8. In several cases, the kink is more “smeared out”, meaning the increase of the torque signal is more gradual and not discontinuous, as shown in Fig. 4.9.

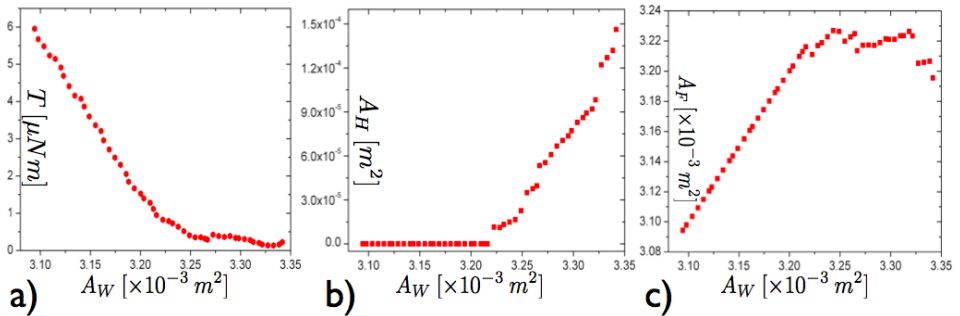


Figure 4.9 – a) The torque versus wedge area for a run with a “smeared out” kink. Compared to Fig. 4.8a), there is no discontinuous jump in the torque signal. b) The hole area as a function of the wedge area for the same data as in a). c) The foam area versus A_W .

4.3.1 Using A_F as Control Parameter

The data shown in the previous section suggest that instead of using A_W , we should use A_F to characterize the state of the foam. After all, the foam area tells us directly how much the packing is compressed.

Plotting T as a function of A_F , we get Fig. 4.10. This figure shows that the underlying physics in the mixed and boundary jammed regimes are similar: the torque simply increases because the foam area decreases. As the slope of T vs A_F appears constant in these regimes, it appears that the wedge modulus is approximately constant, all the way down to low values of T , i.e., close to the jamming point.

The figure also shows that in the gravity jammed regime, the foam area

stays essentially constant, while the torque approaches zero. The foam is still deformed here between steps, and due to the constant foam area, these deformations are shear-like. As the torque is very low, the shear modulus in this weakly jammed regime must be low too.

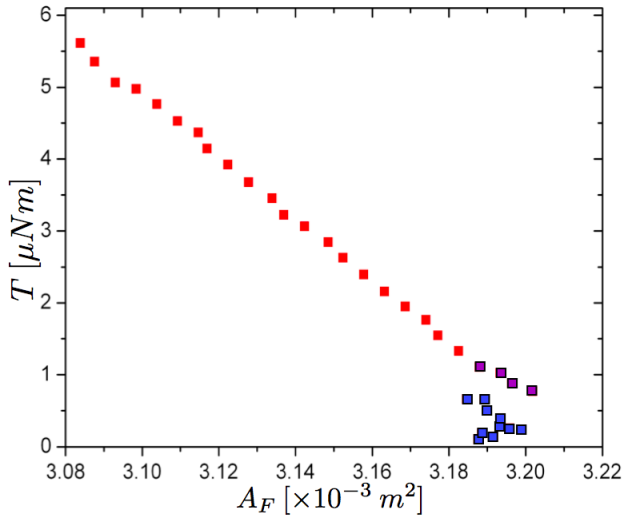


Figure 4.10 – The torque as a function of the foam area. The three regimes outlined in Sec. 3.2 become more apparent: the blue cluster of points at higher foam area correspond to the gravity jammed regime, the purple points are the mixed state and the red points the boundary jammed regime.

Plotting T versus A_F therefore marks a clear transition from a strongly jammed regime where torque increases when A_F is lowered, to a gravity jammed regime where A_F is approximately constant minimum, and $T \approx 0$.

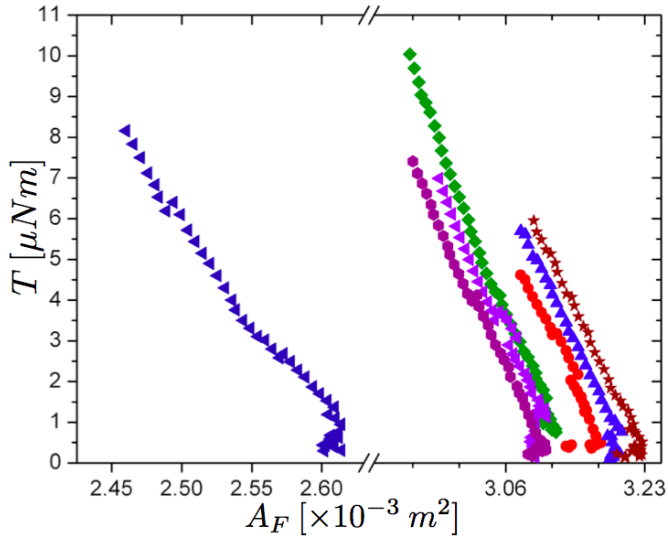


Figure 4.11 – The torque as a function of the foam area for seven runs. Each run has a different range of torque and foam area, yet is performed with the same tilt and t_s and t_c .

In Fig 4.11 we plot T versus A_F for seven experimental runs. We notice that each run has a different range of foam areas and torque, yet all torques rise similarly with A_F . To gain insight on all data sets, we need to rescale the data in a useful manner to collapse all curves.

To obtain a non-dimensional measure of the foam area, we define first, for each run, the maximum foam area A_F^{Max} , and secondly, the ratio $\frac{\phi}{\phi_c} = \frac{A_F^{Max}}{A_F}$, where ϕ and ϕ_c are the packing fraction and critical packing fraction of the foam.

The “traditional” measure of compression, $\Delta\phi$ (see Chapter 2), can be rewritten as follows:

$$\Delta\phi = \phi - \phi_c = \phi_c \left(\frac{A_F^{Max}}{A_F} - 1 \right) \approx 0.842 \times \left(\frac{A_F^{Max}}{A_F} - 1 \right) \quad (4.10)$$

Note that the prefactor ϕ_c is not crucial, but makes comparison to numerics easier.

Even though our values for A_F^{Max} do not vary more than $\sim 10\%$, we rescale the torque by A_F^{Max} . T/A_F^{Max} has dimensions of force per unit length, which is the correct dimensions for a two-dimensional elastic constant.

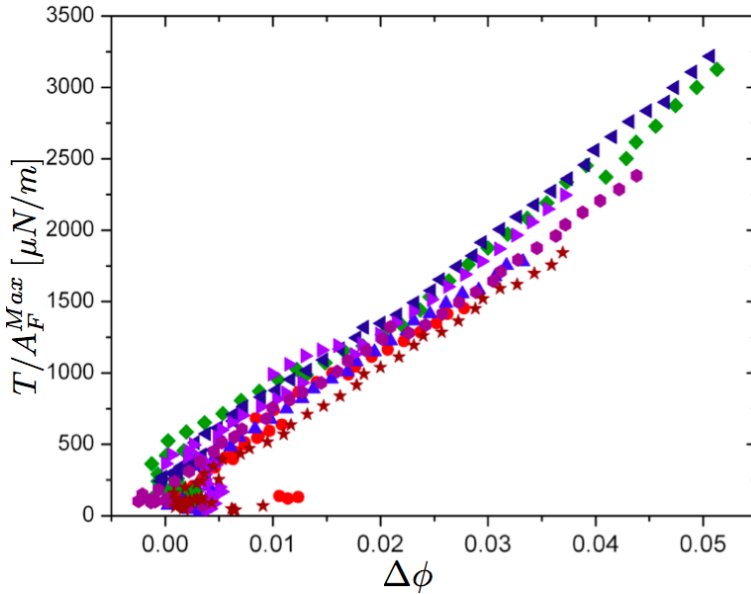


Figure 4.12 – The rescaled torque and rescaled foam area of all runs normalized by their maximum area, A_F^{Max} .

In Fig. 4.12, the same experimental runs as above are plotted using the rescaled quantities. The curves now all collapse. At the origin, there is the typical cluster of points corresponding to the gravity jammed regime. More importantly, however, is how the rescaled torque rises with a similar slope in the boundary jammed regime for all runs. The similarity of the slope indicates that each packing responds to the wiper’s step-wise compression in a similar way.

All data can be fitted with a polynomial function like

$$\frac{T}{A_F^{Max}} = \lambda(\Delta\phi) + \frac{\mu}{2}(\Delta\phi)^2 + T_0, \quad (4.11)$$

where A_F^{Max} is the maximum foam area per run, λ and μ are fitting parameters to be extracted and T_0 is the y-axis offset per run. Fig. 4.13 displays a single best fit to all the data using Eq. 4.11, where we see that a single fit captures the data well.

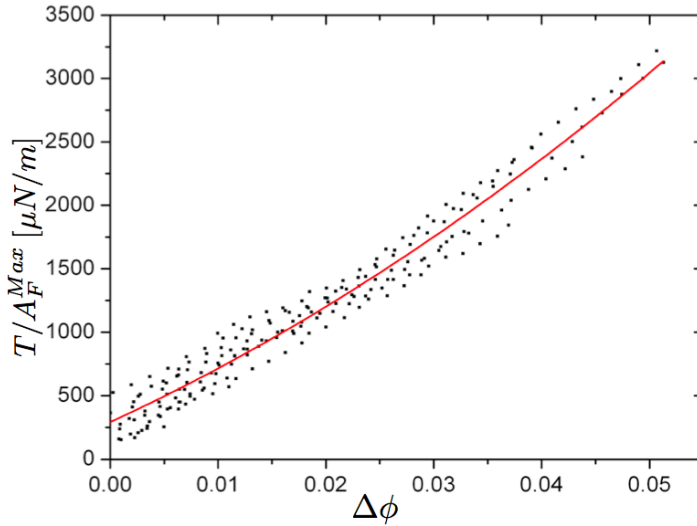


Figure 4.13 – A polynomial fit like Eq. 4.11 on all data without the cluster points at the origin. Here $T_0 = 296 \mu N/m$, $\lambda \approx 0.032 N/m$, $\mu \approx 0.3 N/m$.

With Eq. 4.11 we make a simple estimation of the scaling of $G + K$ by using

$$G + K = \frac{d\left(\frac{T}{A_F^{Max}}\right)}{d(\Delta\phi)} \sim \lambda + \mu(\Delta\phi) \quad (4.12)$$

We see that the slope, λ , from Eq. 4.11 is the value of $G + K$ near jamming. The jump in the data points from the cluster to the increasing signal in torque seen in Fig. 4.10 highlights the most important feature from our data: we are actually observing the discontinuity of the jamming transition in the compression signal going from the gravity to the boundary jammed regime.

4.3.2 $G + K$: A Comparison

In this section, we compare our measurements for the wedge modulus for the slice hole data presented in Sec. 4.3.1 with simulations of two-dimensional foam packings at different pressures. We find that the experimental data shows a remarkable similarity to the simulations, and in particular, both experiments and simulations capture the same discontinuity of the wedge modulus at the jamming transition.

Since the entire foam is under compression in the boundary jammed regime, we are interested in the scaling of the wedge modulus there. We

start by rewriting Eq. 4.9 in Sec. 4.1 and use the foam area A_F to determine the strain. Therefore, the equation now becomes

$$W = G + K = \frac{2\Delta T A_F}{\Delta A_F (r_o^2 - r_i^2)}. \quad (4.13)$$

Fig. 4.14 shows W versus $\Delta\phi$ for all experimental runs using the slice hole protocol. We see that the wedge modulus increases with $\Delta\phi$ and also exhibits a finite intercept at $\Delta\phi = 0$, in agreement with what we found from Eq. 4.12.

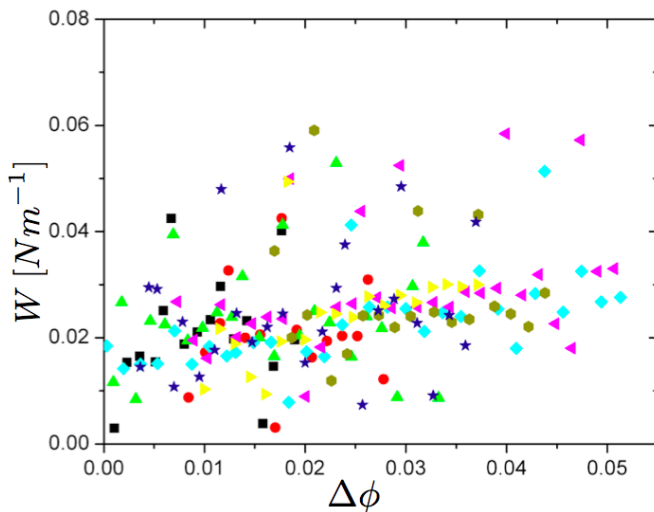


Figure 4.14 – Wedge modulus versus $\Delta\phi$ for all experimental runs.

We now compare our results to simulations of 512 shear stabilized, two-dimensional bubbles in a periodic boundary cell at different pressures, ranging from 10^{-7} to 10^{-1} performed by [53]. The packing fraction is calculated as the area of the bubbles divided by the area of the cell. This is slightly different to our definition of the packing fraction determined in Eq. 4.10, since in the simulations the overlaps in the bubble contacts is included in ϕ [4]. The excess packing fraction is then $\Delta\phi = \phi - \phi_c$, where $\phi_c = 0.842$ as in Eq. 4.10. We choose 512 bubbles in order to compare system sizes as much as possible between our experiments and the simulations. Like in many simulations, the interaction potential of the bubbles is normalized in such a way so that the spring constant, as in Eq. 2.2, is one. To give the pressure and elastic moduli of the packings the same dimensions as our experimental parameters, we change the effective spring constant in the simulations to match the range of those found by Miedema for a chain of

bubbles under compression [42], that is, $k_{eff} = 6 \times 10^{-2} Nm^{-1}$.

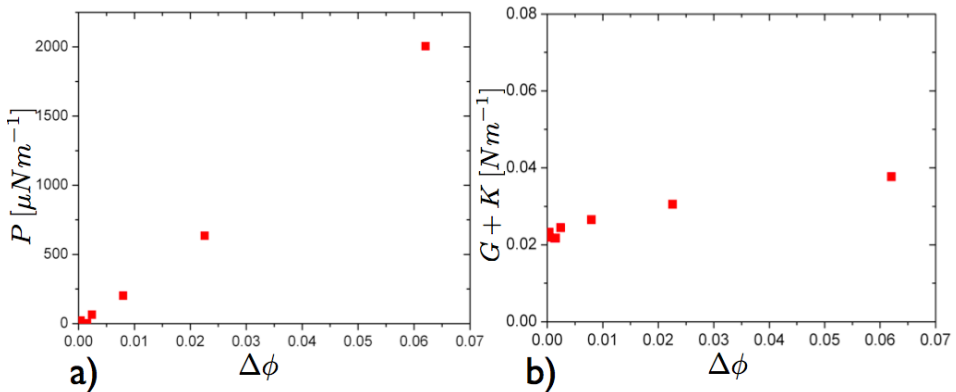


Figure 4.15 – a) P vs $\Delta\phi$ for a simulated bubble packing with $k_{eff} = 6 \times 10^{-2} Nm^{-1}$. b) $G + K$ vs $\Delta\phi$. The intercept and range of $G + K$ and $\Delta\phi$ is similar to that seen in Fig. 4.14 for the experimental data.

Fig. 4.15 a) shows the pressure versus $\Delta\phi$ for a simulated packing. The range of P and $\Delta\phi$ is consistent with Fig. 4.13 for the slice hole experiments.

In Fig. 4.15 b) we show $G + K$ versus $\Delta\phi$. The data clearly shows a finite intercept with a similar value as we found in Fig. 4.14 of roughly $\sim 0.02 Nm^{-1}$, which is quite remarkable. Additionally, the simulation data indicates that as $\Delta\phi$ increases, so does $G + K$, in agreement with theory [13]. This is also observed in Fig. 4.14.

4.3.3 Residual Torque

We have seen in Fig. 4.8 a) and Fig. 4.9 a) that the torque has a finite value when the hole is clearly open, i.e. in the gravity jammed regime. In these two examples, the “kink” in the signal is also markedly different, one being very sharp, the other being “smeared out”. In both cases, the finite value of the torque in the gravity jammed regime, which we call the “residual torque”, comes from the buoyancy of the foams still in contact with the wiper. For all experiments, the wiper will be in contact with at least a few bubbles at the fulcrum. The residual torque will be higher the more bubbles are in contact with the wiper at the start of a run.

We calculate the residual torque of the slice hole protocol and show that by estimating the pressure gradient in the foam packing due to the tilt of the glass plate, we capture the initial torque as measured by the rheometer.

In Fig. 4.16 we start by subtending our wedge geometry into slices of increasing pressure, going from P_0, P_1, \dots, P_4 , where $P_0 < P_1 < \dots < P_4$,

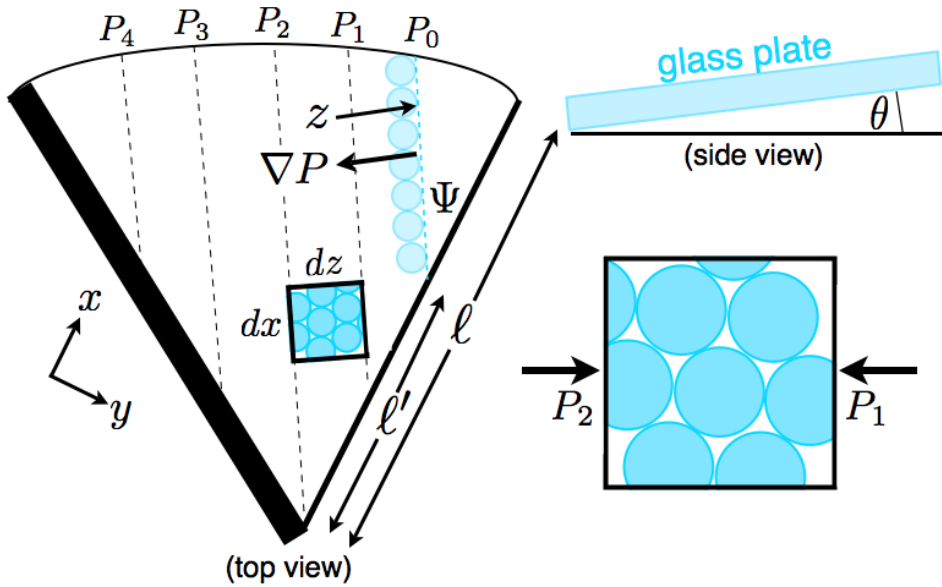


Figure 4.16 – A top view schematic of the wedge geometry to measure the residual torque felt by the wiper. The glass plate is tilted by an angle θ and the directional vector z points along the direction of the effective gravity.

with the assumption that due to hydrostatic pressure, the pressure at the free surface (i.e. at the hole) is $P_0 = 0$.

Our directional vector, z , is parallel to the effective gravity, and opposite in direction to the gradient of pressure ∇P , as seen in Fig. 4.16. The buoyancy of a single bubble under the glass plate, which is tilted by angle θ , is given by $F_{b,1} = \frac{4}{3}\pi r^3 \Delta\rho g \theta$, where r is the radius of a bubble, $\Delta\rho$ is the density of our soap solution given in Sec. 3.1.2 and g is the acceleration due to gravity. In a small rectangular area element $dx dz$, as shown in Fig. 4.16, we calculate the total buoyancy as

$$F_{b,tot} = F_{b,1} \frac{dx dz}{\pi r^2} \phi = \frac{4}{3} r \Delta\rho g \theta \phi dx dz,$$

where ϕ is the 2D packing fraction of $\phi \approx 0.84$. To measure the pressure across our element $dx dz$, we note that the rectangular element is bounded by slices at different pressures, P_1 and P_2 , where $P_2 > P_1$. The force difference across the element is then

$$\begin{aligned}
 dx(P_2 - P_1) &= \frac{4}{3}r\Delta\rho g\theta\phi dx dz \Rightarrow \\
 \frac{P_2 - P_1}{dz} &= \frac{4}{3}r\Delta\rho g\theta\phi \Rightarrow \\
 \nabla P &= \frac{4}{3}r\Delta\rho g\theta\phi,
 \end{aligned} \tag{4.14}$$

which is a general expression for the pressure gradient in the bubble packing going from the hole to the static wall, as seen in Fig. 4.16.

To estimate the torque measured along the wiper, we note that the hole has an open angle between the bubbles and the wiper, Ψ , and that the wiper makes contact with the bubbles a distance ℓ' from the fulcrum, where $\ell' \leq \ell$. If $\Psi = 0$ or $\ell' = \ell$, then the hole is closed. The pressure change along the wiper axis, x , is given by

$$\frac{dP}{dx} = \nabla P \sin \Psi, \text{ where } \begin{cases} P(x = \ell') = 0, \\ P(x = 0) = \ell' \nabla P \sin \Psi, \\ P(x < \ell') = (\ell' - x) \nabla P \sin \Psi. \end{cases}$$

The torque along the wiper, where $x < \ell'$, is

$$\begin{aligned}
 T &= \int_0^{\ell'} dx (\ell' - x) x \nabla P \sin \Psi \\
 &= \frac{4}{3}r\Delta\rho g\theta\phi \sin \Psi \int_0^{\ell'} dx (\ell' - x) x
 \end{aligned} \tag{4.15}$$

Evaluating the integral and taking $\ell' = 0.08 \text{ m}$, $\theta = 0.66 \text{ mrad}$, $\Psi = 10^\circ$ for a typical slice hole experiment, the residual torque is $T \approx 0.25 \mu\text{Nm}$, which is a very good comparison to the torque measured in the gravity jammed regime in Fig. 4.8 a) and Fig. 4.9 a).

4.3.4 High Tilt Compressions

The data shown in the previous section were all taken at a tilt angle of 0.66 mrad . How sensitive are our results to this tilt angle? To probe this we have performed additional experiments for larger tilt angles of approximately $1.0, 1.3, 1.8, 2.9 \text{ mrad}$, corresponding to 3, 5, 10, 20 ticks, see Sec. 3.2.

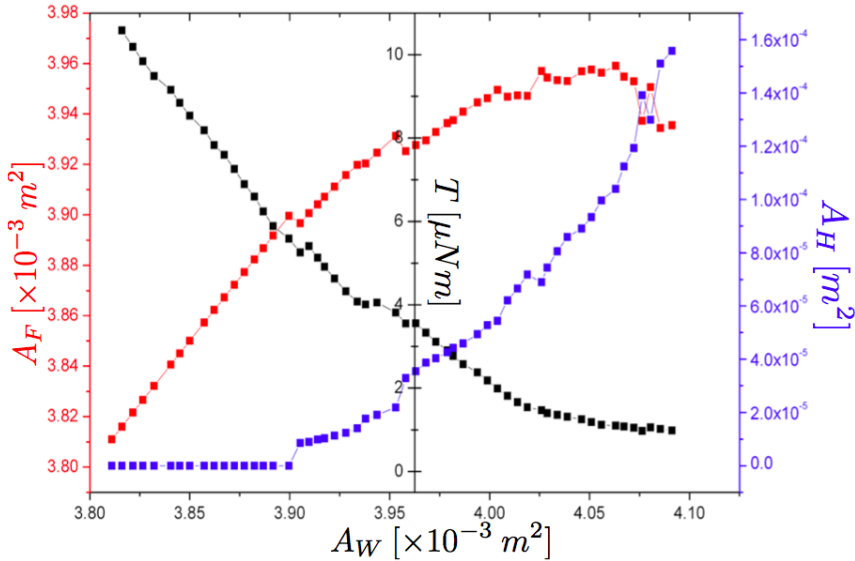


Figure 4.17 – The wedge area versus the foam area (red), the torque (black) and the hole area (blue) for a run with 2.9 mrad tilt.

For each tilt we perform two compression runs, keeping the same timing parameters as before ($t_c = 120$ seconds, $t_s = 1200$ seconds).

Fig.4.17 plots T , A_F , and A_H versus A_W for a run with a tilt of 2.9 mrad , the highest tilt probed. We see that the kink in the torque is strongly smeared out, implying that the mixed regime has grown in comparison to the low-tilt runs in the previous section. Additionally, Fig. 4.17 shows that the hole closes much later in these runs, compared to the low-tilt runs shown in Fig. 4.8 b). The system is only in the boundary jammed regime towards the end of the experiment (for $A_W < 3.9 \times 10^{-3} \text{ m}^2$).

To further investigate the smeared out kink of the torque signal and the late closing of the hole, we look at how the foam area changes as a function of tilt. We normalize A_F with the maximum wedge area, A_W^{Max} , for each run to collapse the data onto one graph. We expect that the buoyancy causes the late closure of the hole as the tilt is increased. For un-tilted runs in the previous section, we notice that A_F stays roughly constant before ultimately decreasing continuously, as can be seen in Fig. 4.8 c). In this case the bubbles are being pushed less due to buoyancy into the wedge and are therefore freer to fill the hole as A_W decreases.

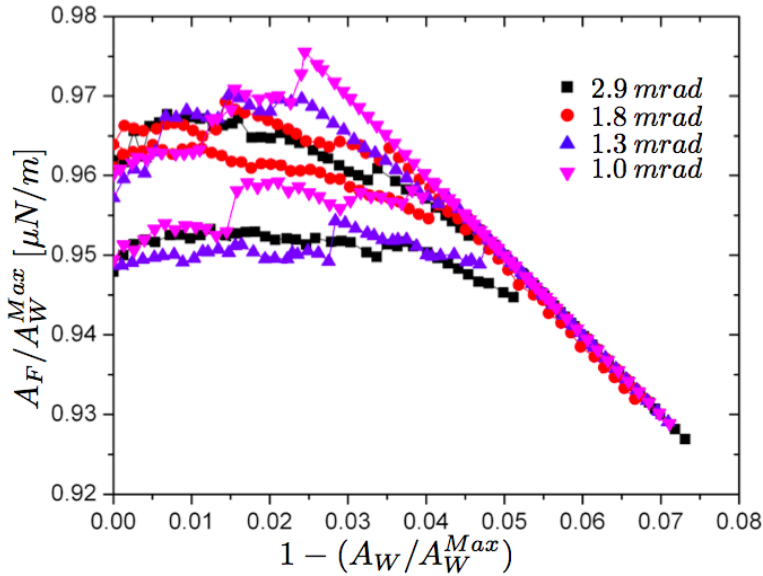


Figure 4.18 – The foam area and wedge area normalized for the four tilts probed. For low tilts (ticks), A_F/A_W^{Max} is constant at first, whereas for high tilts (ticks), A_F/A_W^{Max} decreases.

Fig. 4.18 shows that as we increase the tilt from 1.9 mrad to 2.9 mrad , the foam area goes from a roughly constant signal to a steadily decreasing one. These “plateaus” show that the tilt has an influence of how the hole is being closed: an increase in tilt means a higher buoyancy force on the bubbles. Where for un-tilted and small tilts we observe this A_F remains flat, meaning that the foam can readily accommodate the decreasing A_W , the data for higher tilts show that gravity prevents the bubbles from filling the hole.

How does the torque change as a function of the foam area? Like in Sec. 4.3.1, we rescale A_F by the maximum foam area of each run, A_F^{Max} to collapse the data, and also since T/A_F^{Max} has dimensions of force per unit length, which is the correct dimensions for a two-dimensional elastic constant.

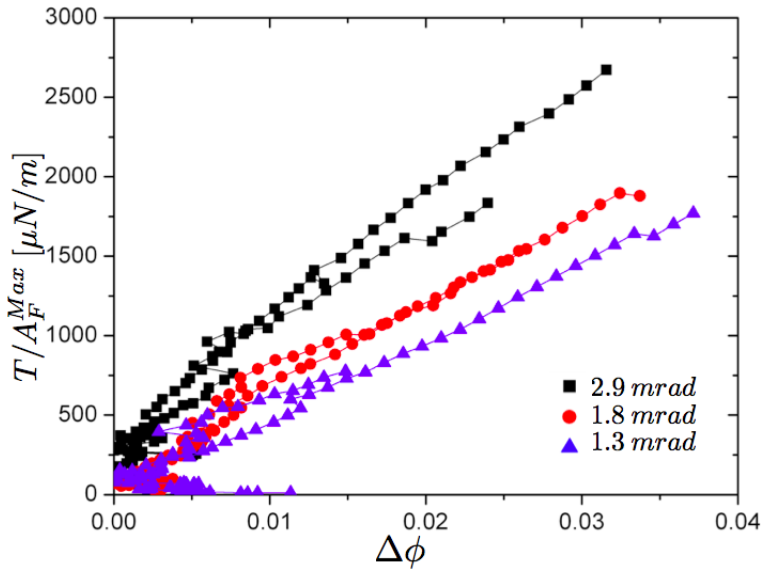


Figure 4.19 – The torque normalized by the maximum area, A_F^{Max} for the three highest tilts. As the tilt is increased, so does the slope.

In Fig. 4.19 the three highest tilts probed are shown. We see that as the tilt is increased, the slope increases, indicating that the torque grows more rapidly under compression for higher tilt. This makes sense, since there is a large initial stress in the system due to the tilt.

4.4 Nonaffinity Near Jamming

In the previous sections we have relied solely on the torque signal to provide information of the system's response to compression. The aim of this section is to highlight the changes in behavior as we close the hole, by analyzing changes in the spatial organization of the foam during and after a compression step. In order to do so we analyze the affine and nonaffine character of the foam bubbles through image analysis. We expect that close and far from the jamming point, the system will respond differently to the deformation imparted by the wiper's compression step. According to [21, 22], a simulated foam packing under compression exhibits much stronger nonaffine linear response close to the jamming transition than far from it. Do we also observe this in our experimental system, where we may be outside the regime of linear response? To probe the spatial organization, we compare the actual response to an affine prediction by subtracting the actual image from this prediction, squaring all resulting pixel differences

and averaging over the image area.

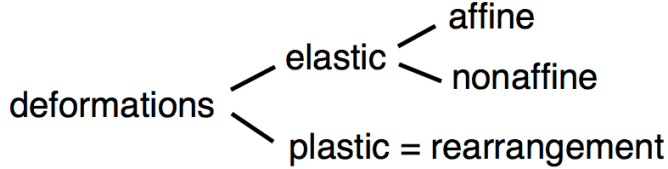


Figure 4.20 – Deformations in our system. Elastic events are best probed using images at early times in t_s , whereas rearrangements are best seen using images at later times in t_s .

The resulting variance gives a straightforward way to quantify changes in the spatial organization of the foam. We make such comparisons for each compression step during our runs. Here, we highlight two results. First, we show that the short time response of the foam does not show plastic behavior, and moreover, is more affine in the compressed, boundary jammed regime. Approaching the jamming point, the variance increases and becomes noisy, indicating more nonaffine motion close to jamming, in accordance with simulations [21, 22]. Secondly, the images show that there often are motions and rearrangements at late times during the sit time t_s , which are often not registered in the torque signal. In other words, even though the torque signal and this macroscopic response may appear rather clean, microscopically the system is plastic and driven outside of linear response, see Fig. 4.20.

Several image analysis steps need to be addressed before we can extract useful information, which will be outlined below. In Sec. 4.4.1 we outline how the images are warped to predict the affine of the foam. Sec. 4.4.2 explains how the variance is calculated and applied to the many compression steps which make up a run. In Sec. 4.4.3 the variance profile of a step is used as an indicator of motion in the system. Finally, in Sec. 4.4.4 we show that there is large nonaffine response in the gravity jammed region and the system responds increasingly affinely under large compression in the boundary jammed regime.

4.4.1 Nonaffine Deformation

In all runs presented here, over the course of the change time, t_c (see Fig. 3.23), the wiper moves 1 mrad in 120 seconds before sitting at the new, fixed angle for time $t_s = 1200$ seconds. The frame rate of the images is 0.033 Hz , meaning that during t_c four frames are captured and that during t_s , 40 frames are captured, see Fig. 4.21. We see that for any step, at

image I_0 , the wiper starts its compression and ends this at image I_4 , having moved $1/4 \text{ mrad}$ between each frame (recall the wiper moves at a constant rate to the new angle, see Sec. 3.3.2). The next 40 images recorded are the wiper fixed at its new position.

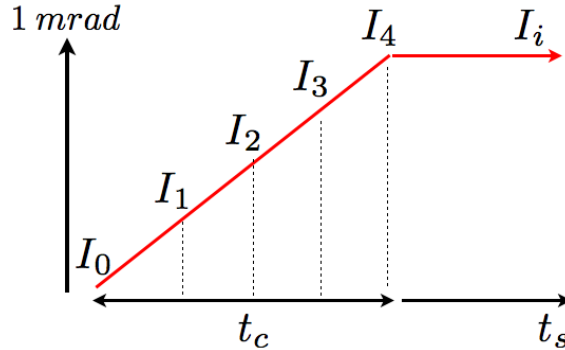


Figure 4.21 – The images captured during one compression step and subsequent relaxation: four images during t_c and 40 during t_s .

In order to examine the response of the foam packing between I_0 and subsequently right before the next t_c , at I_{43} , see Fig. 4.22, we compare the actual images to their respective affine predictions, based on affinely deforming image I_0 . We do this “affine correction”, since if we were to compare the two images without adjusting for wiper motion, we would measure how the foam responds to the compression, yet also be adding in the change in the position of the wiper between the two images to the variance signal. This would ensure that there is always a change happening between the two images, whereas the foam might not have rearranged at all under the compression step.

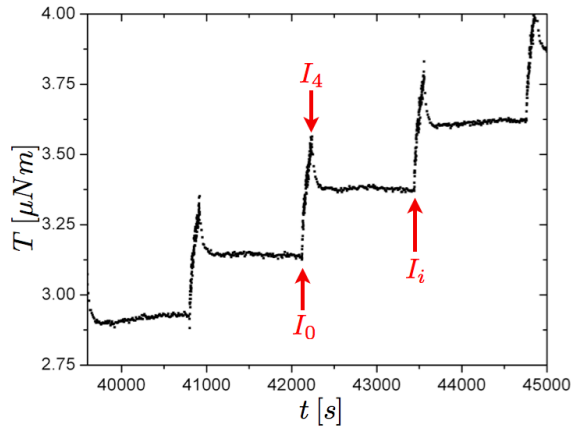


Figure 4.22 – A torque versus time plot indicating which images are used for comparison to calculate the variance over that compression step.

We use the two IDL routines, POLYWARP and POLY_2D, first encountered in Sec. 3.1.4, to affinely deform the image I_0 so as to determine the affine prediction for the deformation at a later time labeled with the integer i . To determine the affine deformation, we first determine a set of coordinates along the perimeter of the wedge geometry, which define the position of the fixed wall and moving wiper. From these positions we determine the origin (where the wall and wiper would intersect).

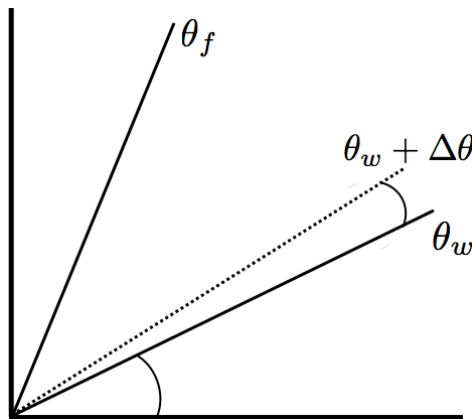


Figure 4.23 – Coordinates to determine the affine prediction for the deformation field.

In polar coordinates (r, θ) , the wiper is then determined by its angle θ_w and the fixed wall by a larger angle θ_f , and deformations arise if the

wiper moves over an angle $\Delta\theta$, see Fig. 4.23. The affine prediction for the deformation field is then given by a linear relation between θ' (the angular coordinate after deformation) and θ as:

$$\theta' = \theta_f + (\theta - \theta_f) \left[\frac{\theta_w - \theta_f}{\theta_w + \Delta\theta - \theta_f} \right]. \quad (4.16)$$

Since we know the angle $\Delta\theta$ as a function of i (see Fig. 4.21), we can thus determine the affine prediction of the foam configuration at each step i by appropriately deforming I_0 using the POLYWARP and POLY_2D routines in IDL; we refer to this affine prediction as \bar{I}_i .

Using this affine prediction allows us to focus on the nonaffine motion of the foam and suppress the trivial wiper motion. In Fig. 4.24, we compare $I_{43} - I_0$ and $I_{43} - \bar{I}_{43}$, and see that the compression step adds a visible signal in $I_{43} - I_0$, which is absent when using the affine prediction.

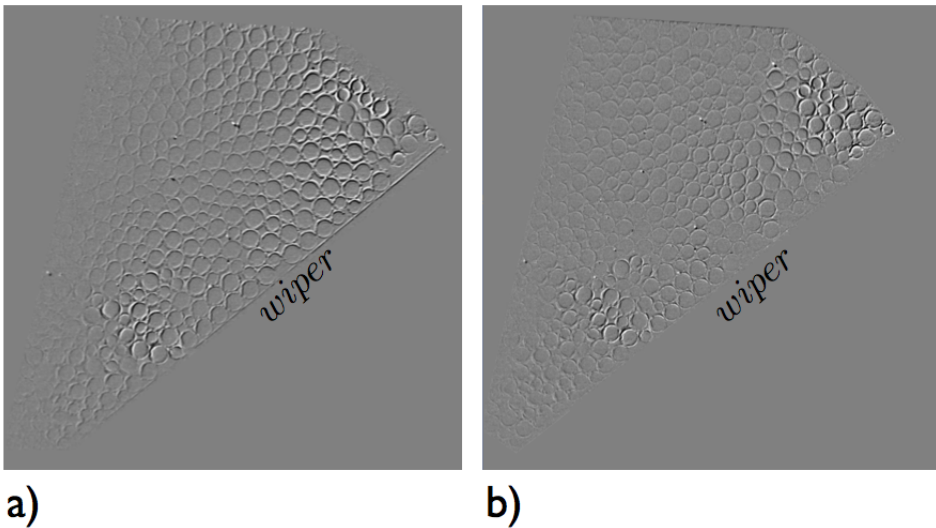


Figure 4.24 – Difference of images of bubbles and the wiper highlight the motion of the wiper after a compression step a) without correction and b) with correction. In a), we simply compare I_{43} with I_0 . Note that the wiper outline can be seen clearly without the affine correction. In b), we compare I_{43} to \bar{I}_{43} . The wiper outline is gone and the signal is smoother.

4.4.2 Variance in Compression Runs

Once we have affinely corrected the images in each step, the variance lets us characterize the changes in pixel values between the compared images.

By looking at the variance over the course of our runs, we observe the dynamics of the system in the gravity and the boundary jammed regime.

The variance is defined in the following way:

$$Var[i] := \frac{\sum [I_i - \bar{I}_i]^2}{\text{no. of pixels}}, \quad (4.17)$$

in arbitrary units. Since images are taken at regular time intervals, the variance compares how the system changes between two points in time. The change in the pixels between these two points will give information about whether the foam has undergone any nonaffine deformations.

4.4.3 Foam Motion Signal

For each step in the slice hole protocol, the torque signal measured by the rheometer can be compared to the variance signal extracted through the image analysis. We are interested in seeing whether the torque is sensitive to plastic events.

In Sec. 4.2.1 we encountered torque signals that were not well equilibrated in some steps, leading us to believe there was motion happening in the system, which we show now to be true. We also show, in addition, that in some cases, even for seemingly well equilibrated steps, there are rearrangements in the system. Note that although we can determine whether the bubbles are moving, we are not able to say from the variance alone how many bubbles or where in the wedge they are moving. For this we need to inspect the images. The magnitude of the variance signal offers insight into the magnitude of events: the higher value, the more motion. We can, however, tell from the variance if a rearrangement has stopped or is still occurring by the end of the step. Since we measure the variance for each \bar{I}_i in the step, an increasing signal means the motion is persisting; a constant variance signal means no more motion is happening.

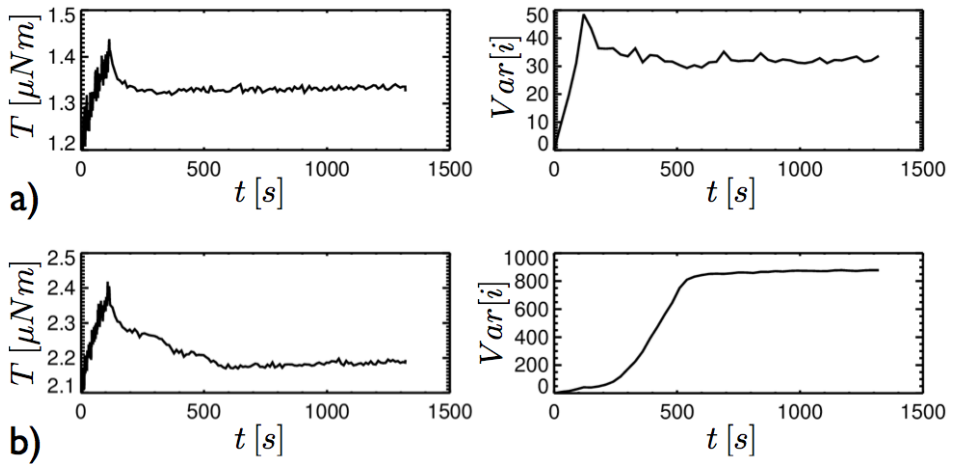


Figure 4.25 – T and $\text{Var}[i]$ vs time. a) A well equilibrated step in torque and corresponding variance signal. b) A step where for the first few hundred seconds a rearrangement is occurring, as can be seen in the variance signal. Note the change in scale with respect to a).

Fig. 4.25 shows T and $\text{Var}[i]$ versus time for two different steps in a run. In Fig. 4.25 a) the torque signal is well equilibrated, and so is the variance: the signal is constant, indicating no long time or large motion by the bubbles. However, in Fig. 4.25 b) the torque is not equilibrating for over 600 seconds, before finally reaching a steady state. The variance shows this initial unease: for the first 600 seconds the signal grows rapidly to a very high value, indicating a large rearrangement in the bulk (compare this large signal to that of Fig. 4.25 a)). Fig. 4.26 depicts the rearrangement that led to the high variance signal in Fig. 4.25 b).

By analyzing the variance signal for all images in a step, over the course of a run, we get an indication of when rearrangements start to happen during the sit time t_s , as well as over how many steps they occur. Comparing different $\text{Var}[i]$ in a step, the evolution of rearrangements in the boundary jammed regime and nonaffine behavior at the jamming transition becomes apparent. Fig. 4.27 shows the variance for a run with 40 steps, where the hole closes at step 17.

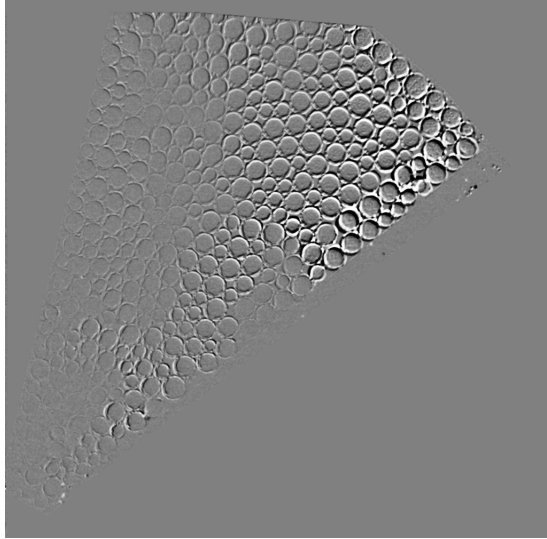


Figure 4.26 – A difference of images showing the rearrangement in the wedge from Fig. 4.25 b).

In Fig. 4.27 a), the evolution of elastic deformations in the system at five different images, $Var[2]$, $Var[4]$, $Var[6]$, $Var[8]$, $Var[10]$, in all 40 steps is plotted. We notice that the signal increases as $Var[i]$ increases, meaning that over time for a step, there is more motion apparent. This reinforces the notion from Fig. 4.20 that for long times (late images in a step), plastic events become more visible, as Fig. 4.27 b) shows. Note that in Fig. 4.27 a), at image $Var[2]$ (black), the variance is lowest since here the wiper has only just started to move and not much motion in the packing has been recorded. The overall variance signal for all images also decreases for higher steps, most markedly after step 17, when the hole closes. This feature underlines the transition from initially very nonaffine to more affine response as the system goes from the gravity to the boundary jammed regime. This decrease of the variance will be shown more in-depth in the following section.

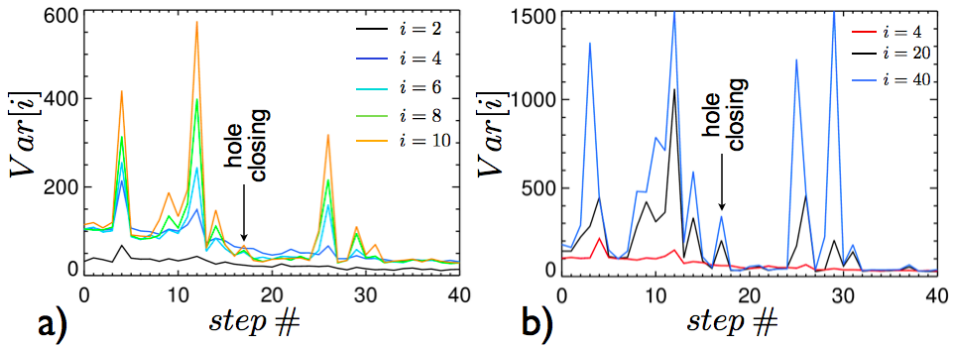


Figure 4.27 – The variance at different images for all steps in a run. The hole closes at step 17. a) The variance for a run at images $Var[2], Var[4], Var[6], Var[8], Var[10]$. The variance increases as \bar{I}_i increases. b) The variance for the same run at images $Var[4]$ (red), $Var[20]$ (black) and $Var[40]$ (blue).

We start to get an indication of the amount of plastic deformations in the packing using later images, like in Fig. 4.27 b). The black and blue variance curves of Fig. 4.27 b), images $Var[20]$ and $Var[40]$ respectively, highlight that in many cases there is persistent motion in the foam, long after the wiper motion has ceased.

In the run shown in Fig. 4.27, the hole is closed after step 17. We notice, first, that before the hole closes, i.e., in the weakly jammed, gravity jammed regime, the foam motion persists, in almost all cases, over long times, whereas the boundary jammed case shows a mix of “quiet” steps where the nonaffine deformations are small and do not grow with time. The boundary jammed regime also shows that rearrangements, where the nonaffine deformations are large, do grow with time. Notably, rearrangements seem to occur over several steps. Recalling from Sec. 3.3 that $t_s = 1200$ seconds, our data indicates that many rearrangements, like those at step 29, persist for over 40 minutes.

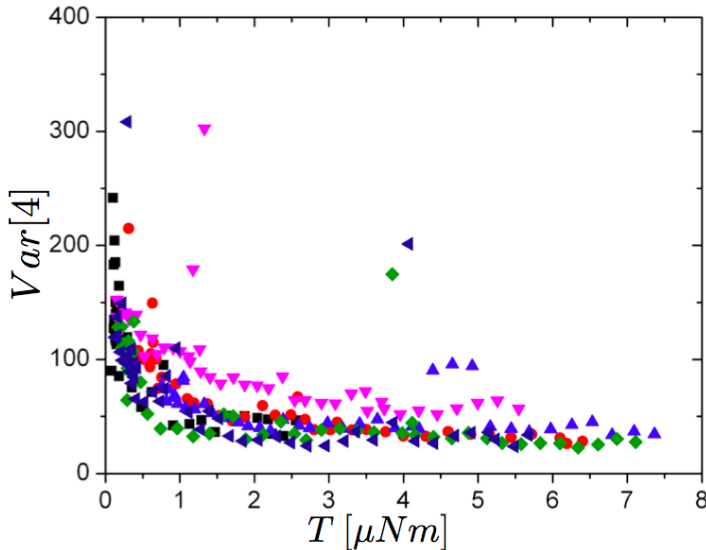


Figure 4.28 – $Var[4]$ versus T . The decrease of the variance with increased compression starts to highlight the affine response of the foam.

Our data thus suggest the following scenario, shown schematically in Fig. 4.20. The deformations can be elastic in nature (small deformations, short time relaxation) or plastic (larger nonaffine motion, long time behavior).

We now first turn our attention to the short time behavior of the foam, and in particular focus on $Var[4]$ (although $Var[i]$ for $i = 1, 2, 3$ shows very similar behavior). In Fig. 4.28 we plot $Var[4]$ versus the torque, T . Clearly, the early time variance exhibits a systematic trend with torque, decreasing with torque and apparently diverging as $T \rightarrow 0$. Identifying the early time behavior of the foam with the elastic linear response, this trend appears to be qualitatively consistent with previous numerical predictions [20, 21, 22].

4.4.4 Comparing Torque and Variance Signals

We already have shown before, in Fig. 4.28, that in several cases we can find a clear correlation between the time evolution of the torque and variance signals. How strong is this correlation? To get insight into this question, we characterize the torque signal by the drift at later times (see Fig. 4.5 in Sec. 4.2.1), as $\frac{\tau_2 - \tau_1}{\Delta t_{fit}}$, where Δt_{fit} is the time interval over which we make a fit in t_s . The closer the slope to 0, the more equilibrated the step. We characterize the nonaffine nature of the deformation field by $Var[43]$.

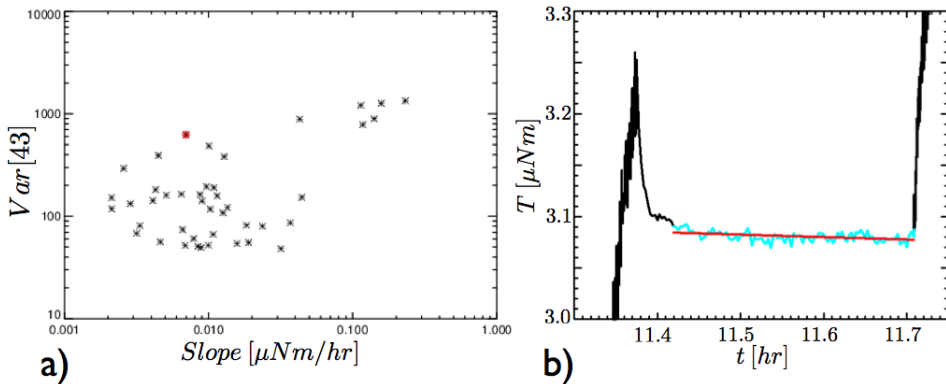


Figure 4.29 – a) $Var[43]$ versus the slope of a run. b) The step corresponding to the red point in a). The slope of the red line fit is $0.0069 \mu Nm/hr$. Some steps indicate that despite small slopes, rearrangements are still occurring.

Fig. 4.29 a) shows a scatter plot of $Var[43]$ versus the fitted slope to the measured T signal for all the steps in an entire run. We see that the late time variance and slope are correlated: when the slope is large, the variance is high. However, the correlation is not very strong; as the red point indicates in Fig. 4.29 a), there are also steps when the torque signal looks very well equilibrated, while there is significant motion in the foam as detected by $Var[43]$, and shown in Fig. 4.29 b).

We conclude that the torque signal itself is a poor indicator of whether or not the microscopic response is elastic; in the regime close to jamming that we probe here, plastic behavior is the norm, not the exception. The mechanical response, as probed by the torque signal, is rather insensitive to these rearrangements, allowing us to characterize the mechanics without too much attention to the microscopic rearrangements.

Rearrangement of Foams: Effects of Distance to Jamming

Under large deformations, any material will exhibit plastic behavior. In ordered systems, such plastic behavior is associated with the motion of defects, and defects are easily identified [7]. In contrast, for disordered systems, such as the foams we are studying here, but also emulsions, suspensions and granular media, there is no obvious local order, which means that the whole concept of defects does not apply. Nevertheless, these systems will undergo plastic deformations under large enough applied strains, as anyone who has ever used or played with shaving foam can attest. What happens microscopically during such plastic deformations, is that the constituent particles (grains, bubbles) experience rearrangements [21, 32, 33, 34, 35, 54, 55, 56, 57].

A wealth of work on plastic deformations in disordered media have revealed that in many cases, these rearrangements are build up from localized events, where one or more particles swap neighbors [56, 57]. For example, in the well-studied case of dry 2D foams, such localized events take the form of so-called T1 events, as shown in Fig. 5.1.

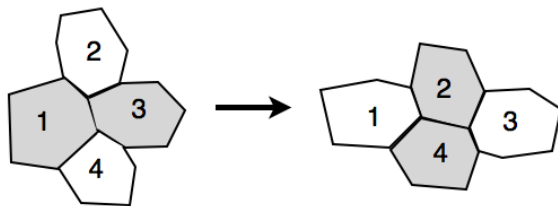


Figure 5.1 – An example of a T1 event in very dry foams. Bubbles in contact are shaded gray.

In that case, the T1 events cause most of the dissipation [57] and can organize spatially [33, 34, 55]. As a matter of fact, many other particulate systems also are believed to be dominated by T1 events (see Fig. 5.2), or by less well defined shear transformation zones [56] which are not completely localized but nevertheless have a similar quadrupolar nature.

Here we probe what happens with the nature of rearrangements in 2D foams when we start to approach the jamming point, i.e., go from the dry to the wet limit of foams. There are several reasons to expect the nature of the rearrangements to change. First, almost *any* property we probe seems to change dramatically when approaching jamming. In particular, the spatial organization of the elastic response changes from nearly affine in dry foams to strongly nonaffine in wet foams and the magnitude of the nonaffine bubble motion grows near jamming (see Sec. 5.3). In linear response, there are diverging length scales near jamming (see Sec. 2.3.1). A priori there is thus little reason to expect rearrangements to be insensitive to the distance to jamming.

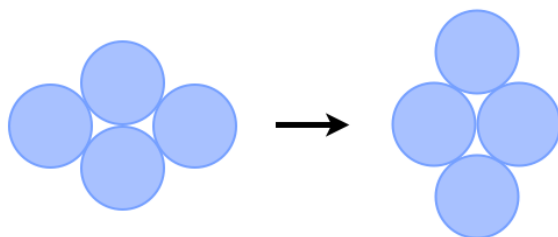


Figure 5.2 – An example of a T1 observed in many particulate systems: nearest neighbors become next-nearest neighbors.

To study rearrangements in 2D foams close and far from jamming, we will subject our foams to pure shear deformations in a so-called biaxial cell. The outline of this chapter is as follows. In Sec. 5.1 we briefly review previous work on deformations in (dry) foams. In Sec. 5.2 we describe

our experimental setup in detail. In Sec. 5.3 we describe our experiments, and show substantial qualitative trends in the nature of rearrangements as function of the J-point. We close this chapter in Sec. 5.4 with a brief discussion and suggestions for further work.

5.1 Previous Work

Studying the spatial organization (and later, rearrangements) of foams in 2D has a rich history. In 1947 Bragg et al. used bubbles floating on a free fluid surface, the so-called bubble raft, as a model for plastic failures in atomic crystalline structures such as metals [7]. By creating perfectly monodisperse bubble rafts, Bragg showed the types of dislocations and defects that arise in these structures of monodisperse bubbles. Feynman [58] noted that the slippage of a whole layer of these crystal structures in a plane does not happen in one fell swoop; rather one atom at a time moves along the slip plane. This is because it costs the system far less energy to move one particle at a time than the entire row. The same phenomenon was observed by Bragg for dislocation in the bubble rafts. Monodisperse bubble rafts thus form a simple model to probe plasticity in crystals. What about plasticity in amorphous materials?

To characterize the organization and subsequent rearrangement of bubbles in amorphous packings under small shear deformations, Argon et al. [54] used bidisperse bubble rafts. By labeling each bubble by hand, Argon could identify the number of bubbles partaking in a rearrangement and the free area change during this process. He found that dislocations due to the shear never moved the bubbles by more than 1-3 bubble diameters and that during rearrangements, these events were very localized, leaving the rest of the packing unaffected. Hence, the microscopics associated with plasticity are strongly influenced by disorder, and this work was the first indication of very localized behavior in two-dimensional foams for high packing fractions.

The 1990's saw an uptake of interest in dry foams under shear, [41, 57, 59]. An important goal was to connect the phenomenology of rearrangements to the mechanical response, i.e. stress, and to understand the role of simple shear, for instance in avalanches etc. In particular, by measuring the change in energy of their simulated bubble packing, Terwari et al. [57] observed that for dry foams there was a well-defined quasistatic limit at low enough shear rates where localized rearrangements, of T1-type, occurred at a constant rate per unit strain. Moreover, the stress response exhibited sharp downward steps whenever a rearrangement occurred. This was found to hold independent of system size. They also showed that for

wetter foams, the event size distribution broadened into a power-law that is limited by the system size. Terwari's work marked the distinctive notion that the type of rearrangements in wet and dry foams is inherently different in nature, with a more global motion occurring in wet foams and the already observed localized behavior as seen in the work of Argon being typical for dry foams [54]. [60] researched a model where the drops in stress due to a rearrangement for varying packing fractions are linked throughout a packing of bubbles, although the results are still inconclusive.

Past experimental work [32, 34, 35, 55] with bubble rafts focused on rearrangements in wet and dry foams under shear. Like the work of Terwari, Dennin's group found that the initial response of the foam is elastic and above the yield stress, it would flow. The flow in all cases consisted of irregular intervals of a build-up of stress before a sudden stress drop due to rearrangements. Simulations of these stress drops due to rearrangements in bubble rafts [61] were found to be in good agreement with the predictions of the bubble model of [55]. Furthermore, [33] found a clear correlation between the rate of T1 events and the strain rate.

5.2 Biaxial Set-up

In this section we describe the setup that we constructed in order to probe the nature of rearrangements in two-dimensional foams as function of the distance to jamming. The central part of the experiment is a biaxial cell, illustrated in Fig. 5.3. We keep our two-dimensional bidisperse foam in the central rectangular area of this cell, and an arrangement of three sliding and one fixed walls allows us to set the two dimensions, L_x and L_y , of this cell independently. Such a biaxial setup allows for a wide range of deformation experiments to be performed. In particular, by enlarging or shrinking L_x and L_y simultaneously, we can (de)compress the foam, controlling its distance to the (un)jamming point, whereas by increasing L_x whilst decreasing L_y (or vice-versa) such that the area $L_x L_y$ stays constant, we can apply a pure shear to the foam. We note here that we will only probe the spatial structure of the bubble displacements and rearrangements that take place in the foam under pure shear by imaging, and in contrast to previous chapters, will not measure the stresses arising in the foam.

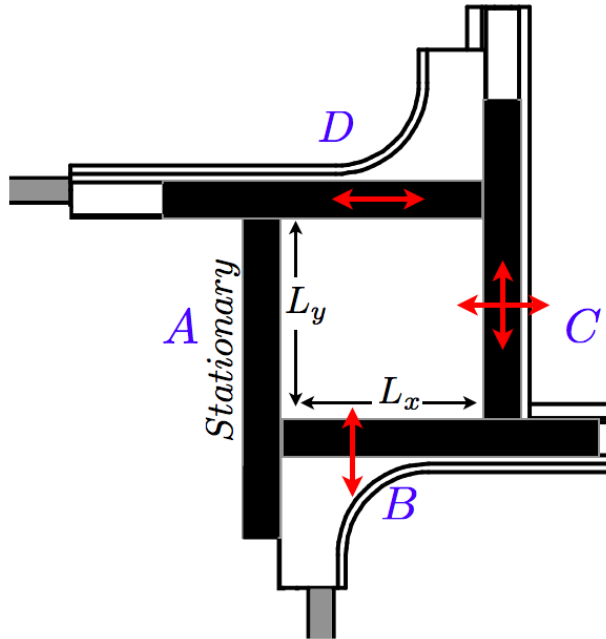


Figure 5.3 – A top view schematic of the shear cell that contains the foam packing. Wall (A) is stationary; wall (B) moves only up and down on a track connected to (A); wall (C) is connected by tracks to wall (B) and (D) and can move up/down and left/right; wall (D) can only move left and right on a track connected to (A). Walls (B) and (D) are driven by motors.

We first describe the set-up's main components and how they are put together to create the biaxial cell in Sec. 5.2.1. Sec. 5.2.2 discusses how we move the walls in order to apply a pure shear. In Sec. 5.2.3 we describe our experimental protocols, and in Sec. 5.2.4 and Sec. 5.2.5 we detail our image analysis technique.

5.2.1 Set-up

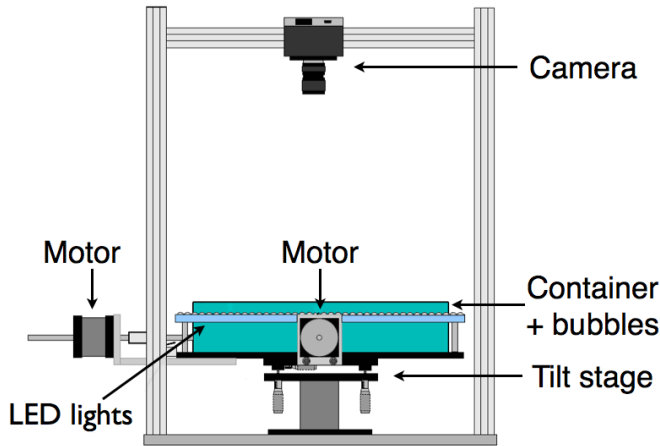


Figure 5.4 – A side view of the biaxial set-up. Two motors control the movement of the walls of a rectangular cell inside the container. The walls sit under a glass plate and bound a packing of foam bubbles confined to the cell.

Fig.5.4 and 5.5 show side and top views of our experiment. The main square container ($220\text{ mm} \times 220\text{ mm} \times 65\text{ mm}$) houses the soap solution and the bubbles. As before, our foam consists of a single layer of bubbles floating on a surfactant solution and trapped below a glass plate, and the main container is partially covered by a glass plate (8 mm thick plain window glass, square of $100\text{ mm} \times 100\text{ mm}$ in dimension).

For the foam we use the same soap solutions as before (glycerol, SLES and CAPB, for details see Sec. 3.1.2). To reduce excessive use of soap solution, PMMA blocks are placed in “unused” parts of the main container, as shown in gray in Fig. 5.5. These blocks also act as barriers to decrease the thermally driven circulation of fluid in the container that is driven by heating from the lighting. We prevent evaporation of the solution by covering the top of the container not covered by the glass plate with a clear plastic square.

The shearing walls inside the container slide under the glass plate. The gap between the walls and the plate is 0.5 mm to allow the smooth motion of the walls yet still keep the packing trapped in the rectangular cell. The container sits atop a Newport M-37 Tilt and Rotation platform, which is used for leveling the system, similar as described in Sec. 3.2. The whole set-up sits on a metal framed table on which a camera is mounted. The frame is enshrouded in black cardboard to keep out the ambient light of

the room.

The lighting of the foam is crucial, since the light must strike the Plateau borders at an angle to obtain optimal contrast. The walls of the main container are made of 5 mm thick, transparent PMMA, allowing light to enter the main box, and a flexible LED light-strip (Silikon LED Flexstrip from SLV Elektronik GmbH) is placed around the outside of the main container to illuminate the bubble packing inside, as shown in Fig. 5.4. The container has an anodized, black aluminum bottom plate to optimize contrast in the images.

To observe the rearrangements in the biaxial set-up, we image the foam from above with a CCD camera (Basler A101f camera with 1300×1030 pixel resolution) hung above the cell, equipped with a Cosmicar/Pentax TV lens. As the camera is straight above the center of the shear cell, we do not need to correct for skew. The camera is triggered and the images are stored using a LabVIEW code. The frame rate is fixed at 0.5 Hz . Distances in the image, for example to extract bubble diameters, are calibrated using 1 mm spaced markings etched into the top of the shear walls as a reference length, as seen in Fig. 5.13.

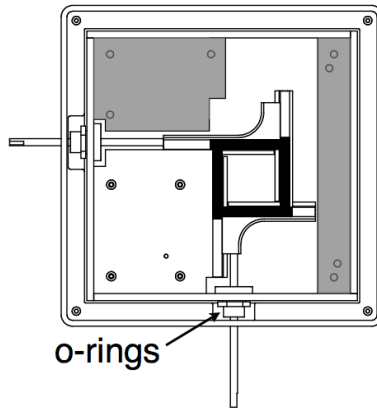


Figure 5.5 – A top view schematic of the biaxial set-up. The motor shafts are sticking out of the container.

The center of our setup are a set of moveable walls on the inside of the container that enclose the foam packing and form a biaxial cell. These walls are made of elongated, transparent PMMA rectangles, 8 mm by 100 mm long, which themselves are mounted on hard black, PMMA frames. These hard black frames slide perpendicular to each other by way of interlocking, swallow-tail slides and are driven by motors. A detailed view of the frames and their tracks can be seen in Fig. 5.6. Of the four bounding walls, two are

driven by the motors and three actually move. This is shown in Fig. 5.7 a). Two of the PMMA walls have cut-outs in them to allow access to the biaxial cell containing the bubbles with syringe needles, shown in Fig. 5.7 b).

The motion of the walls is controlled by stepper motors, placed outside the fluid container, that are connected to the movable wall via rods that slide through two holes in the side walls of the container (Fig. 5.4). These holes are sealed with two rubber o-rings, one on the inside and one on the outside of the container, shown in Fig. 5.5. The o-rings create a tight fit around the motor shafts and ensure that no solution leaks out. Some tuning is in order to optimize the tightness of the fit: a too-tight fit creates stick-slip motion when the motors are driving the shafts, causing the inside walls to vibrate, while too loose fits lead to leakage. We have been able to machine the o-rings such that the container remains sealed whilst allowing the shafts to move smoothly when driven. In addition, we have carefully aligned the motor shafts so as to avoid stick slip motion to occur.

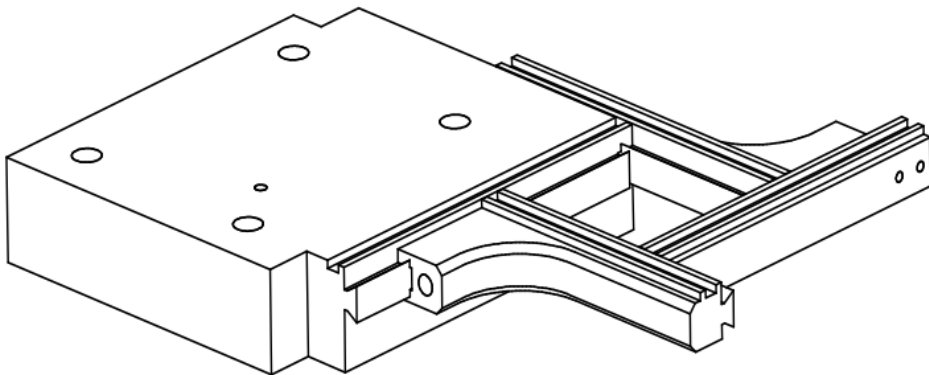


Figure 5.6 – A detailed schematic of the frames that are driven by the motors. The four foam-bounding, clear PMMA walls are mounted on these frames, which slide on swallow-tail tracks.

The motors that drive the frames (and therefore the walls) are stepper motors from Haydon Switch & Instrument Inc. A threaded shaft is translated by the rotation of the internal rotors, where each full rotation translates the shaft 0.6mm . The actual control is done using a “Step Motor Ministep Driver” (model SMD41B3 by JVL Industri Elektronik) driver. This driver enables us to subtend each step into 3200 ministeps every time it receives a signal greater than 5V . One step in this mode corresponds to a 186nm shift in the walls. Each motor is controlled separately by its own driver, which is provided by a 5V square wave signal made with a function generator (TTi TG1010A). The function generator is connected by GPIB

cable to a computer running a LabVIEW code from which we set the drive frequency of the signal and thus adjust the step-rate and amount by which the walls move.

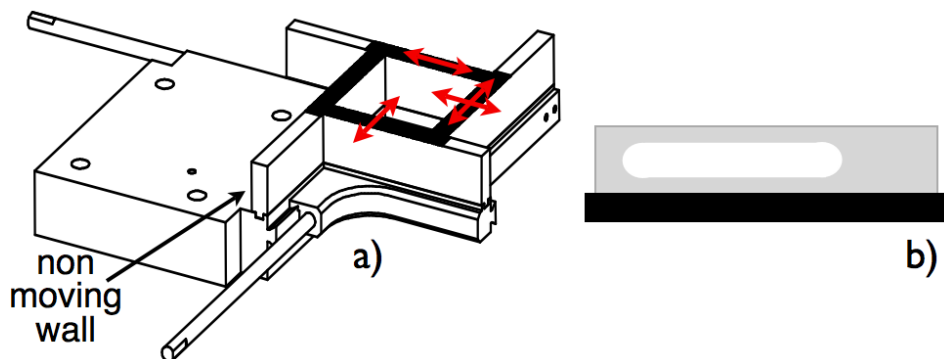


Figure 5.7 – a) A schematic of the walls and their motion, indicated by the red arrows. The walls are mounted on black, PMMA frames which are connected to the motor shafts. Only one of the four walls does not move at all. b) A side view schematic of one of the two walls and the hole through which the syringe needle to make the foam packing is placed.

The foam is made directly in the cell by placing a syringe needle through one of the cut-outs in the moveable walls. We blow N_2 gas at a constant rate through a needle submerged 2 cm deep in the solution. The base pressure of the gas is 3.5 bar , but decreased and tuned to useable levels using valves. To control the two different bubble sizes, we use two different gauge needles, 25G and 30G (0.26 mm and 0.16 mm inner diameters, respectively). We create about 50% big bubbles and 50% smaller bubbles by number. The foam bubbles we use are between $1.8 - 2.7\text{ mm}$ in diameter, determined by image analysis. Using a bent syringe needle, as described in Sec. 3.1.2, we remove the satellite bubbles and mix the packing to ensure the bidisperse foam does not have significant crystalline patches.

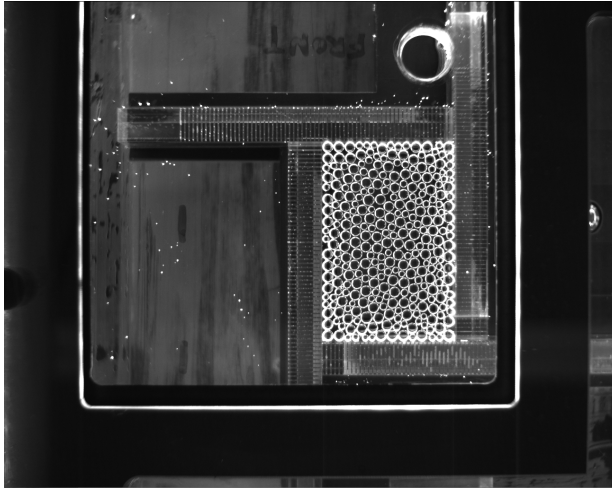


Figure 5.8 – Top view of the shear cell. The black frame holds the glass plate under which the bubbles are trapped. The motor shafts, which can not be seen, enter the set-up from the top and the right in the image. The three screws holding the frame in place are just out of the image.

5.2.2 Shear and Strain

Under shear deformations, the foam area is conserved and the foam thus remains at a similar distance to the jamming point, making shear deformations ideally suited for studies of rearrangements at controlled packing fraction. In simple shear, a single wall moves in parallel to its opposite wall, but it is hard to change or control the packing fraction. We therefore opt for using a biaxial cell. To shear foams in such a cell, we need to apply pure shear, where two boundaries move, compressing and expanding the foams in perpendicular directions as illustrated in Fig. 5.9.

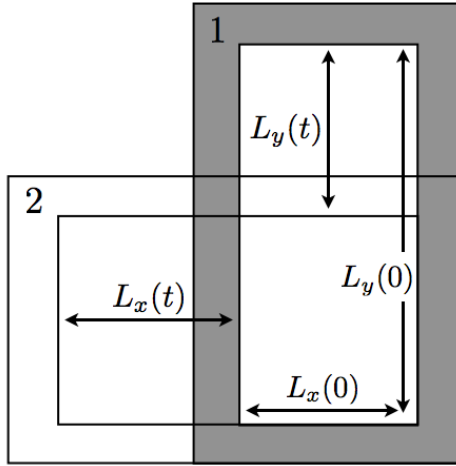


Figure 5.9 – Pure shear of a rectangle. The area under this type of shear is conserved. The rectangle starts the shear at 1 and ends in a configuration like in 2.

An experimental difficulty is that this necessitates one sidewall getting shorter, while a perpendicular wall gets longer. We resolve this by having sliding walls. Recall that in our experiment the motion of the sidewalls, and hence L_x and L_y , are controlled by the frequency of the pulse signal sent to the stepper motors. In order to keep the area $L_x L_y$ constant, we have to continuously update these driving frequencies. We will now derive the equations that dictate the speed at which the motors must move, starting from some initial position.

Consider the starting length of our X and Y walls to be $L_x(0)$ and $L_y(0)$, respectively, like in Fig. 5.9. In our experiment we drive the Y wall at a constant frequency, f_y , leading to a constant speed of the Y wall, v_y : $L_y(t) = L_y(0) + v_y t$. Now, requiring that the area remains constant implies

$$L_x(t) = \frac{L_x(0)L_y(0)}{L_y(0) + v_y t}. \quad (5.1)$$

which upon differentiating, using $L_x(t) = L_x(0) + v_x(t)$ (we thus define outward motion for v_x as positive) and $v_{x,y} = a f_{x,y}$, where $a = 186 \text{ nm}$, yields that

$$f_x(t) = \frac{L_x(0)L_y(0)f_y}{(L_y(0) + a f_y t)^2} \quad (5.2)$$

We use LabVIEW to send this continuously varying drive frequency to the stepper motor which controls the X wall. An example of the updating signal is shown in Fig. 5.10

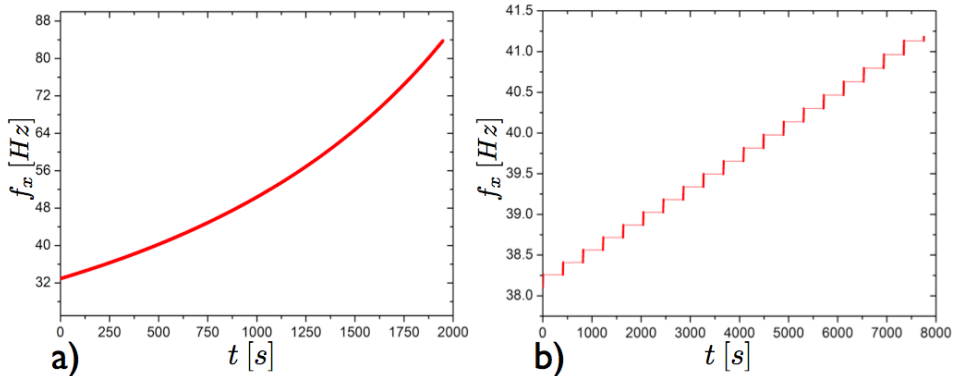


Figure 5.10 – The change of the X wall frequency, f_x , over the course of the a) continuous shear protocol and b) the “start/stop” shear protocol, where $t_c = 8$ seconds and $t_s = 400$ seconds.

We have checked that with this protocol the area under shear is indeed constant. We use ImageJ to calculate the area of the cell every 125 seconds over the course of an experiment. In Fig. 5.11 we note that even over long periods of time, the area remains constant, with very little fluctuation. The motors are thus correctly driving the system. Small deviations from a uniform area signal over the course of a run in Fig. 5.11 come from the way we manually measure the area using ImageJ.

The strain under pure shear in the biax set-up is determined by first defining a deformation $e = \frac{L_x(t) - L_x(0)}{L_x(0)}$. The lengths of the walls are therefore

$$L_x(t) = (1 + e)L_x(0)$$

and

$$L_y(t) = \left(\frac{1}{1 + e}\right)L_y(0),$$

which guarantees that $L_x(t)L_y(t) = L_x(0)L_y(0)$. We describe the initial configuration of the rectangle with the vectors $\vec{L}_1 = (L_x(0), 0)$ and $\vec{L}_2 = (0, L_y(0))$. After a deformation e , the new values of \vec{L}_1 and \vec{L}_2 are given by $\vec{L}_i = \overleftrightarrow{F}\vec{L}_i$, where $i = 1, 2$ and \overleftrightarrow{F} is the “deformation gradient”,

$$\overleftrightarrow{F} = \begin{pmatrix} 1 + e & 0 \\ 0 & \frac{1}{1 + e} \end{pmatrix}.$$

We use the Green strain tensor [62]

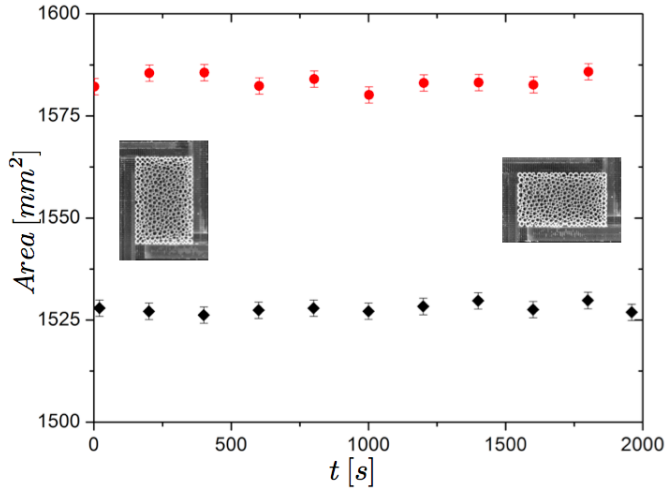


Figure 5.11 – The area of the cell as a function of time for two continuous shear runs, outlined in Sec. 5.2.3. The area remains constant over long periods of time, which is the essence of pure shear. The inset figures show how the cell looks like at $t = 0$ and $t = 2000$ seconds.

$$\overleftrightarrow{E} = \frac{1}{2}(\overleftrightarrow{F}^T \overleftrightarrow{F} - \vec{1}),$$

where $\vec{1}$ is the identity matrix. Expanding and keeping only leading order terms in e , the strain, γ , becomes

$$\gamma = \begin{pmatrix} e & 0 \\ 0 & -e \end{pmatrix},$$

which is the familiar expression for a simple pure shear strain in linear response.

5.2.3 Protocols

In this section we describe the pure shear protocols we use to probe the motion and rearrangements of bubbles in our two-dimensional foam packing. The main idea is to shear the foam either continuously or by using a start/stop-type shear. The packing fraction of the foam can be set by adjusting the dimensions of the cell, and a wet or a dry foam is created by making the cell larger or smaller, respectively. Experiments can be repeated many times, since the walls can be driven back to the same initial position after each run.

Packing Fraction – Since we shear at constant area, the foam will be completely bounded at all times in the biaxial set-up, counter to what we saw in Chapter 3. We estimate the packing fraction in our system by slowly driving one wall outwards while keeping the other three fixed until the packing falls apart.. Taking Fig. 5.9 as a reference, we drive only the X wall at a very low speeds, typically around $4.65 \times 10^{-6} \text{ ms}^{-1}$. The low drive speed is needed to ensure the system responds quasi-statically to the change in area and that the bubbles keep up with the movement of the wall, since they are retarded by the drag with the glass plate. We make an estimate as to how far from the jamming point our foam packings are. The area of the undeformed bubbles is A_0 . If the packing in the rectangle has a starting area A , then its packing fraction is $\phi = A_0/A$. We say the bubble packing falls apart at area A' , so its packing fraction is $\phi' = A_0/A' = \phi_c$, the critical packing fraction. Putting these two equalities together, we get the starting packing fraction of the foam as $\phi = \phi_c \frac{A'}{A}$. The distance to the jamming point is thus found to be

$$\Delta\phi = \phi - \phi_c = \phi_c \left(\frac{A'}{A} - 1 \right). \quad (5.3)$$

Additionally, it must be noted that there is a non-trivial upper limit to the packing fraction we can achieve in the shear set-up. Starting at packing fractions of around $\Delta\phi \gtrsim 0.55$, the bubbles buckle out of plain and start creating bilayer patches of bubbles, as seen in Fig. 5.12. This happens to mainly smaller bubbles in the packing, when they are forced downward by two neighboring larger bubbles.

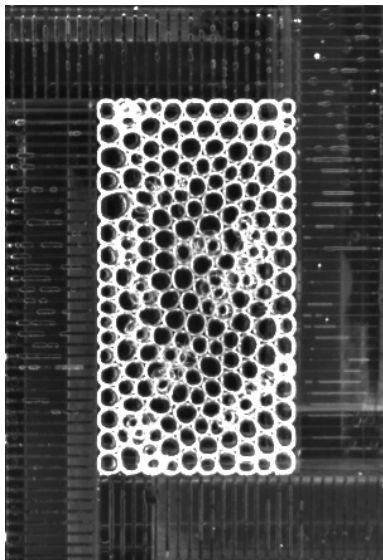


Figure 5.12 – An top view example of a highly compressed foam with bubbles that have buckled out of plane, creating a bilayer in some areas.

This upper limit of $\Delta\phi$ is therefore the driest possible achievable foam packing.

5.2.3.1 Continuous Shear Protocol

We shear the foam continuously from some initial configuration to a final position, like in Fig. 5.13. For these runs we set $v_y = 9.3 \times 10^{-6} \text{ m s}^{-1}$ (“fast”) or at $v_y = 9.3 \times 10^{-7} \text{ m s}^{-1}$ (“slow”) and the packing fraction for every run. We only shear the system in one direction. These continuous shear protocols take around 30 minutes to 4 hours to perform, which means they can be repeated many times if necessary.

5.2.3.2 Start/Stop Protocol

The second protocol is similar to the continuous protocol in that we set v_y and $\Delta\phi$ for each run. However, instead of shearing continuously, we start and stop the shear. We call this the “start/stop” protocol. By changing the output signal the motors receive, we drive the walls for a time t_c at $v_y = 9.3 \times 10^{-6} \text{ m s}^{-1}$ and then stop them, allowing the system to sit still for time t_s . Fig. 5.10 b) highlights how f_x changes over the course of a start/stop protocol. The change in the start value of f_x seen in Fig. 5.10 comparing the continuous and start/stop protocol, or between any run for

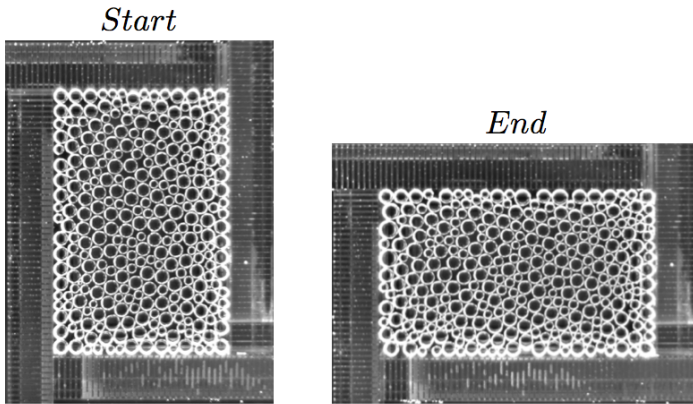


Figure 5.13 – A top view of the start and end images of a packing using the continuous shear protocol. The millimeter markings on the walls are clearly seen.

that matter, comes from the fact that there is a size dependence of the initial size of the cell in Eq. 5.2.

This cycle of starting and stopping the walls is repeated more than 50 times. The most commonly used change times were $t_c = 2, 8, 20$ seconds and sit times of $t_s = 200, 400$ seconds. The sit times are obviously a lot longer than the change time to let the foam relax after the shear and allow us to capture the motion. For wet foams, the rearrangement times are longer than for dry foams, necessitating these long sit periods. For a $t_c = 20$ seconds, $t_s = 400$ seconds is needed to ensure the system is fully relaxed. For the majority of experiments we used the combination of $t_c = 8$ s and $t_s = 200$ s.

5.2.4 Affine Deformation and Variance

In order to understand what type of rearrangement is present in the packing, we analyze the images of the packing taken from above. By comparing sets of images to each other, we get a variance signal whose features tells us the changes taking place in the packing with pixel accuracy. To extract a variance signal from the images in the continuous protocol case, we first need to subtract the affine motion of the moving walls between frames, similar to what was done in Sec. 4.4.1 with the compression experiment. The bubbles at the boundary of the cell are the ones that feel the continuous motion of the walls the most and will thus show a greater change in motion between images. The rearrangements which occur in the packing will also be washed out by the motion of the walls when comparing two images. We

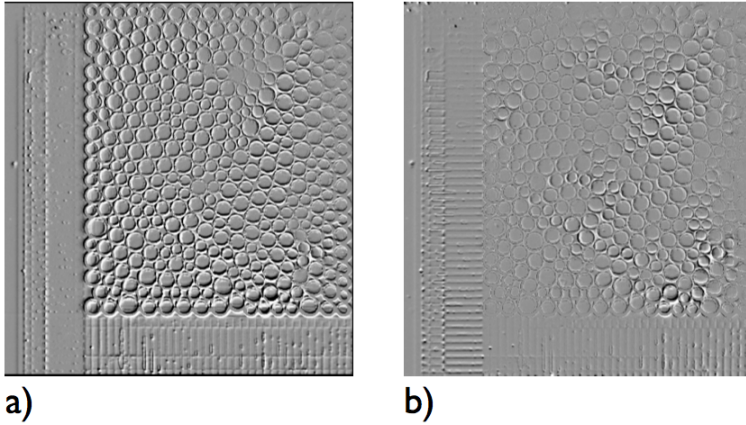


Figure 5.14 – a) In the uncorrected image, the motion of the wall’s influence on the bubbles can clearly be seen during the shearing between two frames. b) The affine corrected image suppresses the motion of the walls, allowing to clearly observe details from affine motion.

correct for this in this section.

This correction process will not have to be done with the “start/stop” protocol, as we observe the rearrangements in the packing during time t_s as a response to the the walls having just sheared the packing for time t_c . In t_s we are observing how the system relaxes and accommodates the induced shear.

To remove the motion of the walls, we use the same IDL routines from Sec. 3.1.4 and Sec. 4.4.1, POLYWARP and POLY_2D. For the biaxial set-up, we first define the four coordinates of the vertices in the first image (x_j, y_j) , where $j = 1, 2, 3, 4$, of the cell containing the foam. We image the pure shear of the cell with a fixed frame rate of $0.5 Hz$, and knowing the velocity of the Y and that the X wall speed goes like $v_x = a \times f_x$, where f_x is given by Eq. 5.2, this gives us the new coordinates (x'_j, y'_j) of the cell for each frame in the recording. The original coordinates are input into POLYWARP to extract warping coefficients. The routine POLY_2D then affinely deforms an image I_i to the affine predicted deformation at a shifted time I_{i+sh} . We refer to this affine prediction as \bar{I}_i .

The rearrangements are more exposed in this manner, as can be seen in Fig. 5.14 a), where we compare two images, one corrected for the affine motion of the walls, the other not.

The variance is defined similarly to Eq. 4.17, so

$$Var[sh] := \frac{\sum_i [I_i - \bar{I}_i]^2}{\text{no. of pixels}},$$

in arbitrary units, and where a value of zero means no change has happened between images, and the larger the value, the more has changed. Because we have the coordinates of the vertices of the cell in each frame, we measure the variance only within these coordinates for each frame. Recall that the area of the cell does not change over the course of the experiment (as can be seen in Fig. 5.11), so the variance signal will not grow due to change in area of the cell, only due to the rearrangements. When comparing the corrected to the uncorrected image in Fig. 5.14, the variance signal will overall be less noisy and therefore lower with the corrected image.

5.2.5 Stick-slip in the Set-up

In the biaxial set-up, the walls of the cell exhibit stick-slip motion due to friction between the motor shafts passing through the o-rings (seen in Fig. 5.5). As the shafts are pushed/pulled during a run, the stick-slip causes the walls to periodically jump forward or backward, following the overall direction of the wall's motion.

In difference images such as Fig. 5.15 a), this jump is noticeable at the boundaries of the cell. Fig. 5.15 b) shows the next difference image, directly after the jump, where no motion at the boundaries is seen. Note that both images are “corrected” for the affine, continuous motion of the walls; the sudden jumps can not be accounted for, as their occurrence is not controlled.

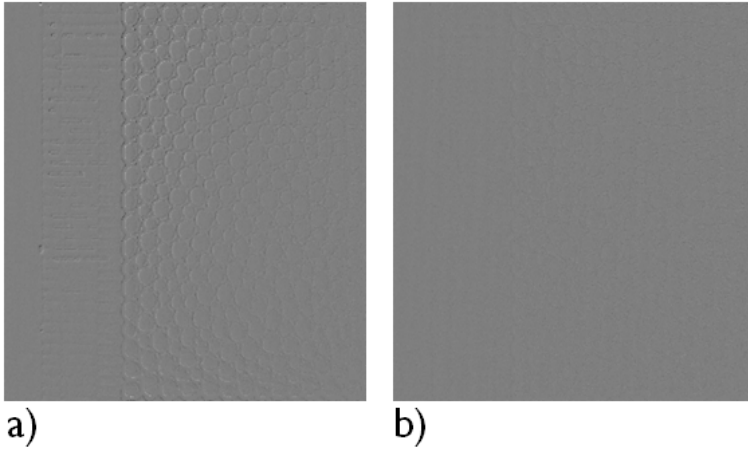


Figure 5.15 – a) The stick-slip motion of the walls causes a noticeable signal at the boundaries of the cell. b) One image later than a), the jump is not seen anymore. The stick-slip is periodic.

Because of these periodic kicks registered at the boundaries in the image analysis, the variance signal exhibits small, periodic peaks, as seen by the black data points in Fig.5.16. These peaks mask the underlying motion and phenomenology of the variance signal and need to be corrected for. The algorithm that we use to detect unwanted peaks in the signal is illustrated in Fig. 5.17. For simplicity, let’s denote the data by $Var[i]$. We then define a “smoothed” signal sm , as

$$sm[i] := \frac{Var[i - 1] + Var[i + 1]}{2}.$$

As we sample the data at a high rate, we do not expect very rapid, and isolated, changes in the data. However, the stick-slip motion precisely leads to signal points being systematically larger than their neighbors, i.e. $Var[i] \gg sm[i]$.

To identify the peaks only due to the walls’ jumping (and spare the rest of the peaks corresponding to actual rearrangements from the averaging), we say that if $Var[i] > 1.2 \times sm[i]$, we have detected “bad” points, indicated by the blue vertical lines in Fig. 5.16. The factor 1.2 is chosen so as to suppress “real peaks” as little as possible while detecting the “false” peaks. With the “bad” point due to the wall jump identified, we replace $Var[i]$ by its neighbors average $sm[i]$, see Fig. 5.17 b). The result is the red curve in Fig. 5.16, which captures the data very well, removes the periodic stick-slip motion and shows that rearrangements (at frame 220 and 280, for example) have not been removed by this procedure.

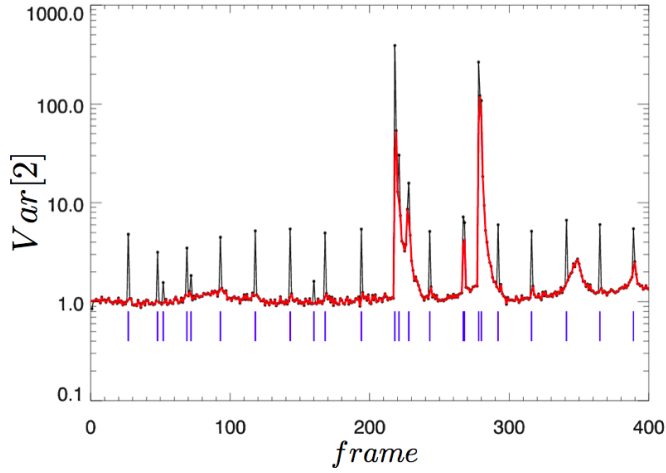


Figure 5.16 – A plot of $Var[2]$ versus frame for a run with $\Delta\phi = 0.118$. The black points are the original data, with the periodic jumps due to the wall motion. The red curve is a processed data set using a peak detection technique. The blue vertical lines indicate where peaks were detected and data points have been replaced by the average of their neighbors.

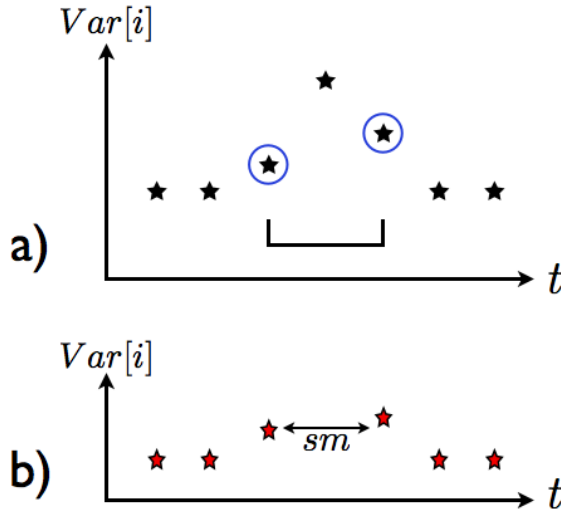


Figure 5.17 – a) Schematic of the variance signal with a high valued, “bad” point due to the stick-slip of the wall motion. The signal is averaged over three consecutive points at a time, resulting in a smoother signal as in b).

5.3 Results

Employing both continuous and start/stop protocols (with emphasis on the former), we will characterize the spatial structure of the rearrangements in our two-dimensional foams as a function of the packing fraction ϕ . In particular, we will employ the variance signal (see Eq. 4.17), spatial snapshots as well as the *inverse partition ratio* to capture the trends with ϕ . We find that in dry foam, rearrangements tend to be relatively short and intense. These are classical T1 events, marked by the quadrupolar nature of the deformation field during rearrangements, see Fig. 5.18. Such T1 events become less well-defined when we move away from the very dry limit. Below $\Delta\phi \approx 0.1$ they are almost irrelevant. In that regime, rearrangements are more smeared out in both space and time. In addition, for wet foams we observe that during shear “rattlers” are generated – loose particles, that with little interaction with their neighbors move in their cage.

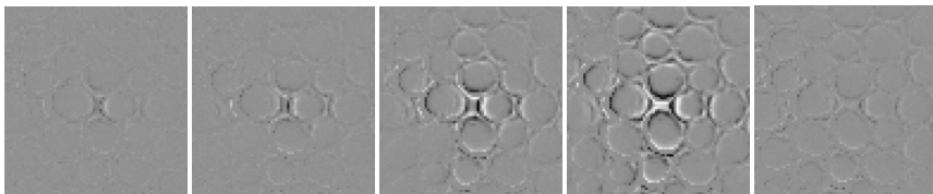


Figure 5.18 – A zoom-in of T1 event as seen in difference of images. The time between frames is 2 seconds. Note the quadrupolar nature of the deformation field.

In Sec. 5.3.1 and Sec. 5.3.2 we show the behavior of dry and wet foams under continuous and start/stop shear, respectively.

5.3.1 Continuous Shear

Using continuous driving, we shear the foam at $v_y = 9.3 \times 10^{-7} \text{ms}^{-1}$ for five different packing fractions of $\Delta\phi = 0.025, 0.12, 0.30, 0.54, 0.59$. In Fig. 5.20 we show the traces of the variance (where we now denote $Var := Var[1]$) of these runs, after filtering out the stick-slip motion and performing the affine corrections described in Sec. 5.2.4. The dry foams show short and sharp bursts of motion, the wetter foams at $\Delta\phi \lesssim 0.3$ show increasingly smeared out behavior. Hand in hand with this, the maximal values of the variance decrease for wetter foams. Snapshots of the deformation fields shown in Fig. 5.19 show that the rearrangements for wet foams become more spread out, but also much slower; this explains the lowering of the peaks in Var .

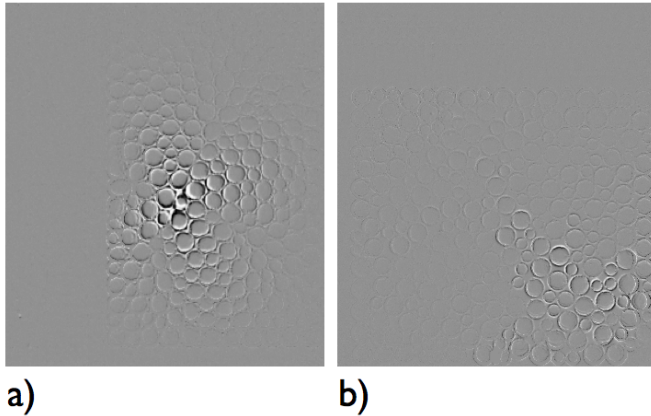


Figure 5.19 – a) A dry foam, mid T1 rearrangement with $\Delta\phi = 0.594$. b) A global rearrangement in a wet foam with $\Delta\phi = 0.025$.

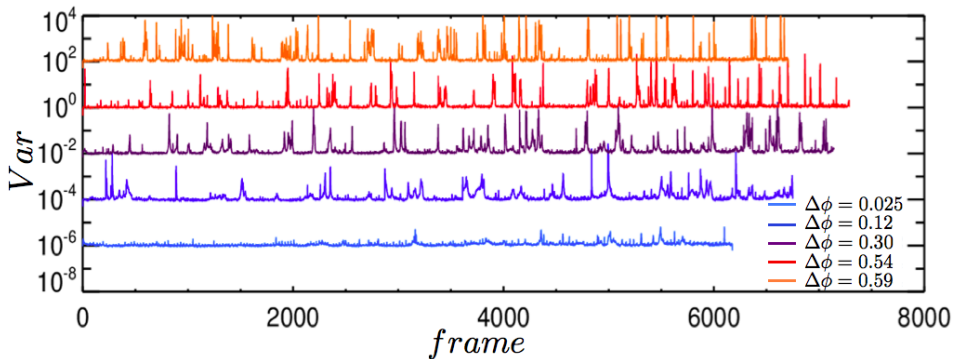


Figure 5.20 – Var versus frame number for five runs, each offset by 10^2 from one another.

A zoom of this data shown in Fig.5.21 clarifies the remarkable differences as we go from a dry to a wet foam. Clearly, runs at low $\Delta\phi$ (blue and light blue) show a low variance signal and deformation events that are drawn out over hundreds of frames. There are fewer sharp peaks in the signal and the system is rarely quiet. This is reminiscent of the nonaffine response seen for systems close to jamming under shear [21, 22]. Increasing the packing fraction to a medium wet foam ($\Delta\phi = 0.30$ (purple)), the behavior starts to change somewhat, with the data showing a mix of sharp peaks and broad ones. The narrowing of the peaks are an indication of the onset of localized rearrangements in the packing, occurring over shorter periods of time. There are still a few global events marked by broad, drawn out rearrangements over tens of frames. The dry foams (red and orange curves

in Fig. 5.21) show only sharp peaks which happen over short periods of time paired with long periods where the system shows no deviations from an affine response.

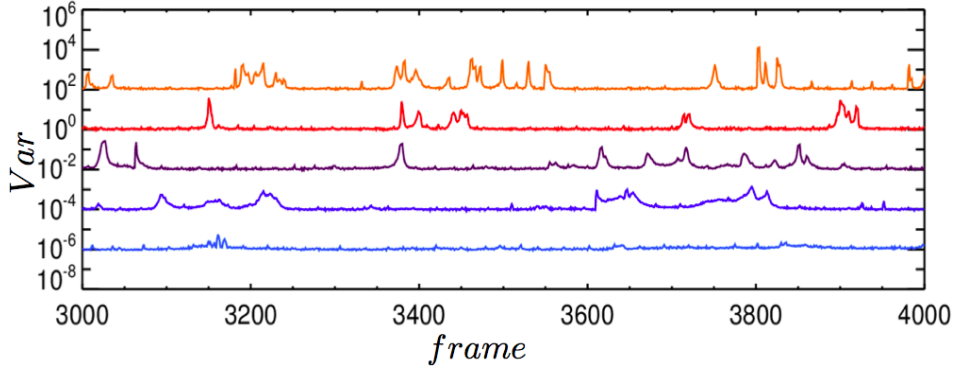


Figure 5.21 – A zoom of the same data in Fig. 5.20, where the packing fractions are $\Delta\phi = 0.59$ (orange), $\Delta\phi = 0.54$ (red), $\Delta\phi = 0.30$ (purple), $\Delta\phi = 0.12$ (blue) and $\Delta\phi = 0.025$ (light blue).

As Fig. 5.21 suggests, a clear distinction between wet and dry foams can be made by looking at the timescales in the variance. To probe this timescale, we have calculated the autocorrelation signal of Var . As the variance, when plotted on a linear scale, is dominated by huge peaks, we focus on the autocorrelation of the log of Var , which we define as:

$$A(\Delta f) := \langle (\log A(i + \Delta f) - \langle \log A \rangle)(\log A(i) - \langle \log A \rangle) \rangle \quad (5.4)$$

where the average runs over the frame number i and Δf is the change in frame. The result is shown in Fig. 5.22. The autocorrelation thus reveals a systematic lengthening of a characteristic timescale when $\Delta\phi \rightarrow 0$. Whether this scale is a strain-scale (i.e. independent of the deformation rate) or is rate dependent is left for further work.

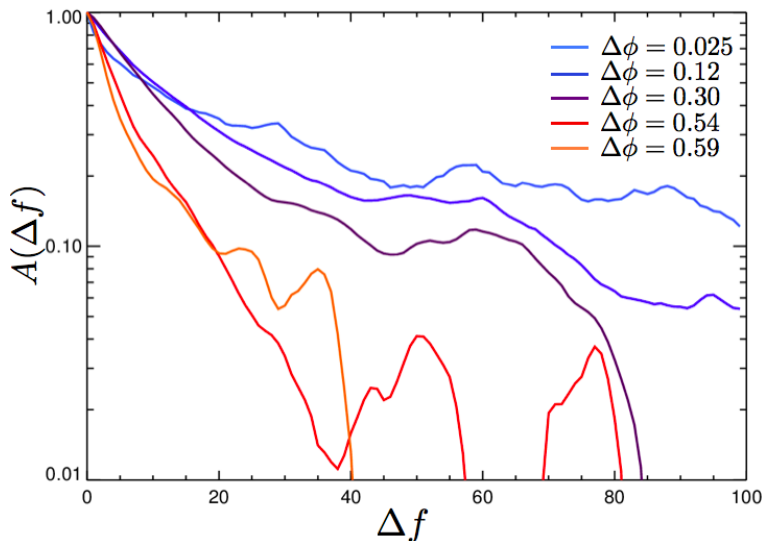


Figure 5.22 – Autocorrelation of $\log(\text{Var})$ versus the change in frame, Δf , for the same five packing fractions shown in Fig. 5.20 and Fig. 5.21.

More quantitative information can be obtained by characterizing the spatial extent of the deformations. To do so, we start from the spatial distribution of the square of the image differences, A^2 , see Fig. 5.23.

We then perform some coarse-graining to obtain a 25×25 grid that represents the sum of A^2 over rectangular boxes of a size similar to the bubble size (see right-most image in Fig. 5.23). Denoting these sums as B_{ij} , we define the inverse participation ratio, I_{ipr} , as

$$I_{ipr} := \frac{N \sum_{ij} B_{ij}^2}{\left(\sum_{ij} B_{ij}\right)^2}, \quad (5.5)$$

in arbitrary units, where N is the number of boxes (here 625). To interpret the inverse participation ratio, notice that for a homogeneous field where all B_{ij} have the same value, I_{ipr} approaches 1. For an extremely inhomogeneous field, where all but one B_{ij} is zero, $I_{ipr} = N$. Hence, I_{ipr} gives a quantitative measure of the spatial spread of events.

In Fig. 5.24, we show traces and a zoom of I_{ipr} for the five continuous runs we have performed. Similar to the variance signal in Fig. 5.20 and Fig. 5.21, there are more sharp peaks for dry foams than for wet foams, although somewhat surprisingly, the maximal inverse participation ratios in both cases are of order 100.

To clearly distinguish these signals, we now focus on all the local max-

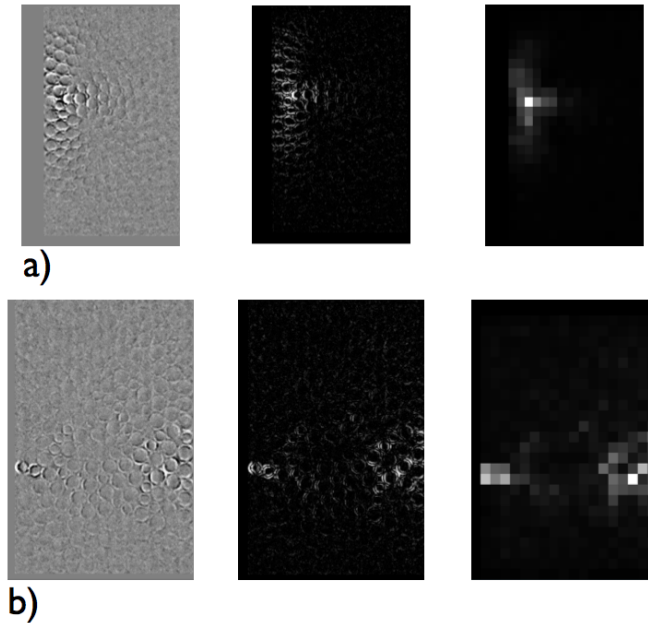


Figure 5.23 – a) Dry foam with $\Delta\phi = 0.54$. From left to right: difference of images, A^2 and sum of A^2 divided over 625 boxes. b) Wet foam with $\Delta\phi = 0.12$.

imum of I_{ipr} . These represent the most localized deformation scales that arise during a deformation.

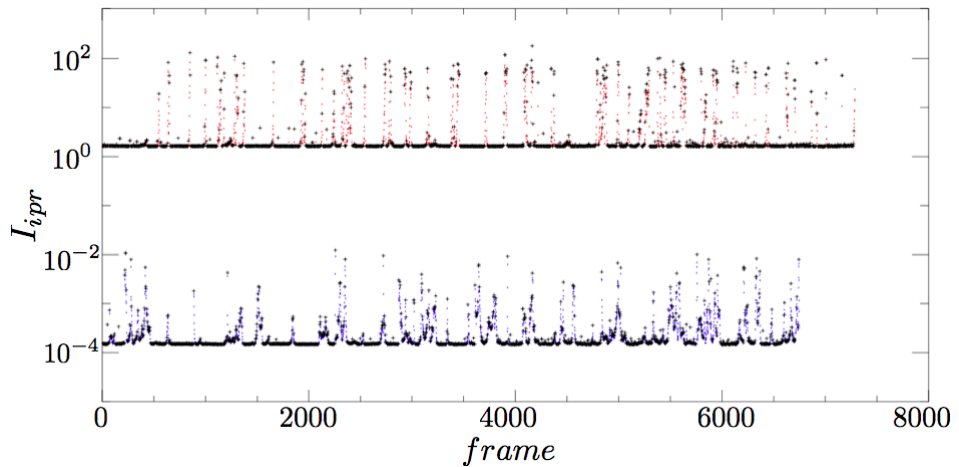


Figure 5.25 – The local maxima of I_{ipr} for two foams with $\Delta\phi = 0.54$ (red) and $\Delta\phi = 0.12$ (blue).

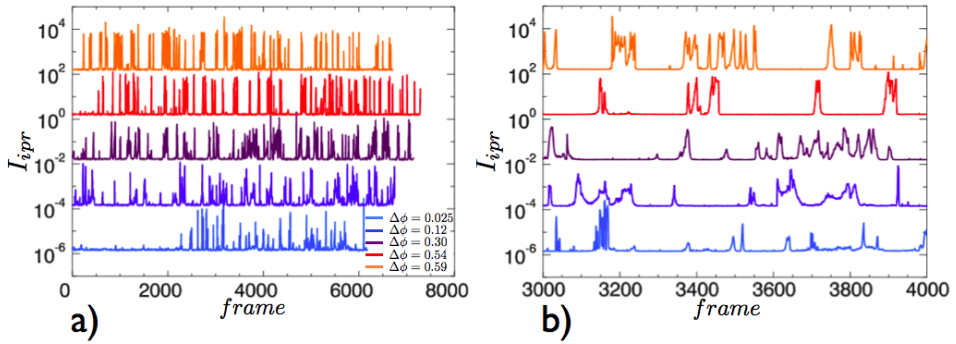


Figure 5.24 – a) I_{ipr} versus frame number for five runs, each offset by 10^2 from one another. b) A zoom of the same data.

Fig.5.25 shows the traces of I_{ipr} for a wet and dry case, with the maxima marked. A close inspection reveals a qualitative difference between the two: for the dry case, there is an abundance of peaks in I_{ipr} close to the maximum, whereas for the wet case, a wide distribution of local maxima of I_{ipr} can be observed.

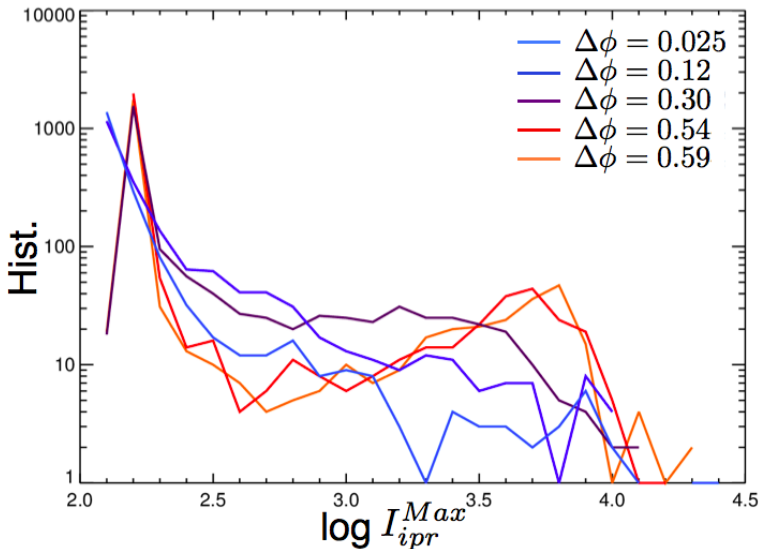


Figure 5.26 – Histogram of $\log I_{ipr}^{Max}$, where I_{ipr}^{Max} are the maxima points identified in Fig. 5.25.

In Fig. 5.26, we show the histogram of the maxima of I_{ipr} , which shows the systematic change from a single to a double-humped distribution as the packing fraction $\Delta\phi$ is increased. We interpret the second peak for the

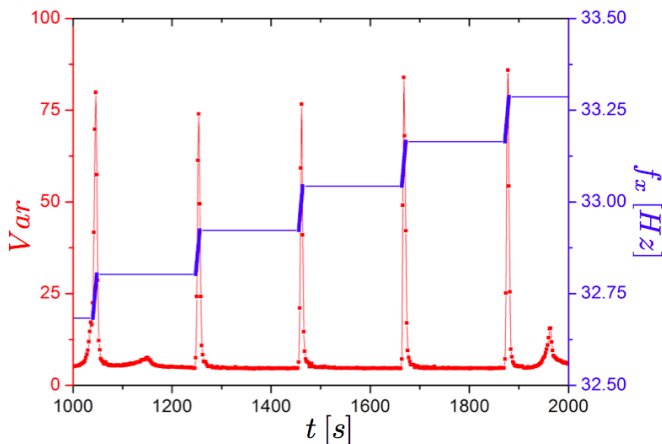


Figure 5.27 – Var (red) and f_x (blue) versus time for a start/stop run with $\Delta\phi \approx 0.25$ and $t_c = 8\text{ s}$, $t_s = 200\text{ s}$. The peaks in the variance show that the walls are moving.

dry foams as corresponding to T1 events, and the loss of this peak again illustrates the loss of relevance of such localized rearrangements closer to jamming.

5.3.2 Start/stop Shear

Using the start/stop protocol, we have explored the variance in order to probe the temporal evolution of the system during the sit time, t_s . In particular, we are interested in how the system relaxes the internal stress by rearrangement due to the shear.

Fig. 5.27 shows Var and driving rate f_x versus time for a medium wet foam of $\Delta\phi \approx 0.25$ for a start/stop run with $t_c = 8\text{ s}$, $t_s = 200\text{ s}$. The walls move only a short time, yet enough for a noticeable variance signal to be detected. The steps in f_x as seen in Fig.5.27 thus create periodically-spaced peaks.

In Fig. 5.28, Var versus time for three different packing fractions of $\Delta\phi \approx 0.15, 0.25, 0.45$ is shown over $t_s = 200\text{ s}$. In all three examples, deformations are taking place during the sit time. For the dry case in Fig. 5.28 a), rearrangement events occurs over a relatively short period of time, as expected, yet the variance signal is not as strongly peaked, in contrast to Fig.5.21 in Sec.5.3.1, where T1 events in a dry foam were marked by sharp peaks. We note that in the continuous shear case, T1 events were of much shorter duration, which partially explains this difference. As we approach the wet foam in Fig. 5.28 b) and c), Var increases in magnitude

and the events take longer to subside. The larger variance signal indicates more bubbles partaking in motion. This larger variance is, however, in contrast to the wet foam behavior seen in continuous shear, where the wet foams exhibited low variance signals (see Fig. 5.21).

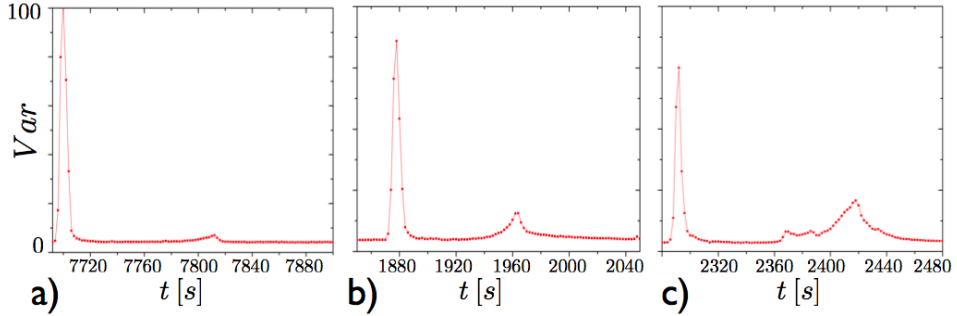


Figure 5.28 – Var versus time for a) $\Delta\phi \approx 0.45$, b) $\Delta\phi \approx 0.25$, and c) $\Delta\phi \approx 0.15$ with $t_c = 8$ s, $t_s = 200$ s.

Var in Fig. 5.28 c) also highlights the continuity of motion in wet foams in that separate rearrangement events seemed to be linked. Between 2360 and 2400 seconds, the motion starts with only a few bubbles partaking, as shown by the low variance. The variance signal then grows rapidly, before eventually relaxing completely. This behavior is an indicator of avalanches in wet foams, meaning one event can “trigger” a further deformation in the packing.

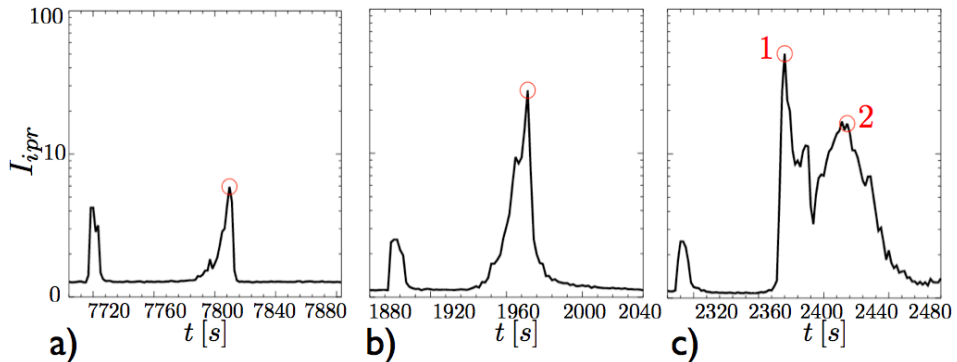


Figure 5.29 – I_{ipr} versus time for a) $\Delta\phi \approx 0.45$, b) $\Delta\phi \approx 0.25$, and c) $\Delta\phi \approx 0.15$ with $t_c = 8$ s, $t_s = 200$ s.

To understand the change in behavior between continuous and start/stop shear, we show the I_{ipr} versus time for the three packing fractions in Fig. 5.29. The T1 event identified in Fig. 5.28 a) for the dry foam shows a

relatively low value in the inverse participation ratio in Fig. 5.29 a) compared to the wetter foams. This is due in part to the signal noise from the periods when the foam is not deforming overwhelming the T1 signal in I_{ipr} , see Fig. 5.30 a). As $\Delta\phi \rightarrow 0$ in Fig. 5.29 b) and c), the I_{ipr} signals broaden similar to Fig. 5.26, indicating a departure from localized behavior to more global deformations in the foam. This is further illustrated in Fig. 5.30, where the difference of images correspond to the circled peaks in Fig. 5.29.

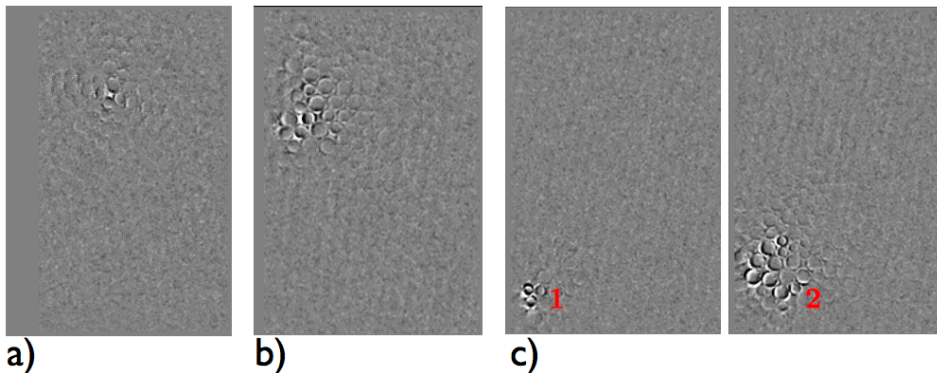


Figure 5.30 – Difference of images of the red-circled peaks from Fig. 5.29 with a) $\Delta\phi \approx 0.45$, b) $\Delta\phi \approx 0.25$, and c) $\Delta\phi \approx 0.15$. The two peaks in c) show at first localized behavior and then more broad, global deformations.

5.4 Conclusions and Outlook

We have shown that a two-dimensional foam under pure shear exhibits markedly different behavior in the wet and dry case, both spatially and temporally. First, the autocorrelation shown in Fig. 5.22 reveals a systematic lengthening of a characteristic timescale when $\Delta\phi \rightarrow 0$. Secondly, histograms of the inverse participation ratio (Fig. 5.26) show that only very dry foams show localized T1 events via a peak in the histogram for large values of I_{ipr} . The loss of this peak when $\Delta\phi \rightarrow 0$ illustrates the loss of localized behavior as we approach jamming.

What remains to be investigated is what is driving the rearrangements in the foam. Does one rearrangement necessarily trigger another? What is the role of coalescence events and coarsening? What causes rearrangements long after driving has ceased?

Moreover, the lengthening of the timescale observed as a foam becomes wetter in Fig. 5.22 remains to be investigated further. The question of whether there is a rate (in)dependence of the rearrangements on the shear

rate was touched upon briefly in [33, 63]. If the shear rate is decreased (increased), it is yet unclear whether the rate of rearrangement will also slow (speed up). For fast events, as in dry foams, we expect the shear rate to be inconsequential; we believe events to appear similarly for fast and slow shear rates. For intrinsically slow deformations, as in wet foams where the motion is more global, we expect the shear rate to play an important role for the rearrangement.

Summary

Many materials we encounter on a daily basis behave very strangely when we poke, tap, squeeze or rub them. The majority of these are so-called amorphous materials, composed of many deformable particles, bubbles or droplets, interacting together in some way. Once we compress or shear these materials, a whole host of interesting and often counter-intuitive phenomena come to light, such as plastic and elastic deformations.

Many materials behave predictably under compression and shear. Stand on a hard table and it will support you (hopefully); rub your hand over its top and you will feel its rough surface. Stand on the beach, and the sand will support you. But watch how the wind carries those same sand particles even with the slightest gust. Systems composed of many hard particles exhibit this strange behavior where they can transition from a solid state to one that is fluid-like. It all depends on how you interact with them.

This transition from solid to fluid-like becomes even more complicated and less predictable the moment we deal with deformable particles, instead of hard ones. Foams are a prime example of a many-bodied system of soft, deformable particles.

Compressing wet foams should be a relatively simple process: collect the foam bubbles into a confining container and then squeeze the walls. If we limit ourselves to two dimensions, we can observe the bubbles in the system and are not hampered by their opaqueness encountered if we were to look at a three-dimensional foam, like beer froth or shaving foam. To place foams into the “jamming” context, we can observe the transition from freely flowing to rigid phases of a wide range of soft materials, when we wedge the foam bubbles in between a soap solution and a glass plate. This way we can control the amount of bubbles in our container before we compress.

Extracting useful information about a foam’s behavior under these circumstance should be straightforward: just by observing the foam, a lot of trivial properties should become clear very fast. For example, to compensate for the change in area under squeezing, the bubbles will deform and rearrange.

This all sounds simple enough to achieve, yet this ideal system of bubbles in a container is a far cry from a real experimental system. Just like the air bubble in

a bottle of water, the foam trapped under the glass is subject to buoyancy forces. If the plate is not perfectly leveled, the foam will drift into some corner of our container. Also, performing this experiment in a room with large temperature fluctuations will cause the foam to go through the jamming point under compression: since foam is a gas, it will expand and contract depending on the ambient temperature.

The challenge when working with foam is being able to control the system enough, in a predictable manner, to drive it through the jamming point by compression.

In Chapter 1, we give a brief overview of topics and issues encountered in this Thesis. We start by introducing the reader to the concepts of jamming in Chapter 2 and ask two fundamental questions: what is the nature of the jammed state and what is the nature of the jamming transition? We present an idealized picture, illustrating the current understanding, by introducing a simple model. We further highlight that materials in a jammed state do not behave like ordinary solids. Many models do not account for this and therefore fail to describe soft systems. The chapter also shows that there is a difference in the scaling of the bulk and the shear modulus as a function of the distance to the jamming point. We end this review chapter by examining past experimental work, as well as introducing some basic concepts of nonaffine motion in jammed systems, which will play a central role in Chapters 4 and 5.

In this thesis, we have experimentally explored the behavior and scaling of a foam under compression and shear by confining it in two dimensions. In Chapter 3, we describe a new experimental set-up, whose complete manipulation and control allows us to probe how a foam packing behaves under compression. We trap a single disordered, horizontal layer of foam between the surface of a soap solution and a glass plate; the sidewalls confine this quasi two-dimensional foam in a wedge geometry. Realizing that even by trapping the foam under a ground and polished flat glass plate will not allow us to probe the jamming transition precisely, we control the tilt of the set-up to bias the positions of the bubbles that sit in the wedge. By using a rheometer in strain controlled mode, we can delicately compress the foam and measure its stress response. We film the set-up from above and have to apply image correction techniques to make the images useful for further analysis.

The foams' response to compression is investigated in detail in Chapter 4. We establish that with the system under tilt, there are two regimes: the gravity and the boundary jammed regime. In the gravity jammed regime, there is a gap in the foam between the moving sidewall that compresses the foam – the wiper – and the foam packing. By incrementally closing the gap, we go into the regime where the foam is fully bounded by its sidewalls. As the gap is closed, the torque that the foam exerts on the wiper starts to increase. Surprisingly, the onset of a finite torque and the closing of the gap do not always coincide, due to residual gravitational forces. This leads us to distinguish between a weakly “gravity jammed” regime, and a strongly “boundary jammed” regime. This allows us to obtain the elastic moduli in the boundary jammed regime, while in the gravity jammed region we find that even though the system is still weakly jammed, it exhibits no elastic response to deformation, indicating that the shear modulus is zero.

In addition, we find a strong increase in the nonaffine fluctuations if we approach the (un)jamming point.

In Chapter 5 we again trap a bidisperse foam layer between a soap solution and a glass plate, yet let the system undergo a controlled pure shear. We confine the foam in a rectangular cell (under the glass plate) that keeps its area constant as the walls are sheared. By imaging from above and determining the difference between images, we can characterize the motion occurring in the system. We can match the variance and inverse participation ratio to the type of rearrangements that occur in the system, and find that if the foam is very compressed (dry foam), there is only one type of rearrangement, known as the T1 rearrangement. This rearrangement is spatially localized and occurs over a relatively short time scale. If we decrease the packing fraction even only slightly, the T1 rearrangement is no longer the sole type, and the system now starts to exhibit more global motion, with many bubbles taking part. The time scale of the motion also increases. As we approach the jamming transition, the motion in the system is completely extended.

Samenvatting

Het is opmerkelijk hoe veel materialen die we in ons dagelijkse leven tegenkomen, zich heel vreemd gedragen als we ze indrukken, knijpen of wrijven. De meeste ervan zijn zogenaamde amorfe materialen, samengesteld uit vele deeltjes, bellen of druppeltjes, die met elkaar samen op de een of andere bijzondere manier wisselwerken. Zodra we deze materialen samendrukken of verschuiven, komt allerlei interessant en vaak tegen-intuïtief gedrag aan het licht.

Veel materialen gedragen zich voorspelbaar onder compressie en verschuiving. Als je op een tafel staat zal deze je (hopelijk) houden. Sta op het strand, en het zand zal je ondersteunen. Maar kijk hoe de geringste windvlaag diezelfde zanddeeltjes wegblaast. Systemen opgebouwd uit een groot aantal van dergelijke deeltjes vertonen dit bijzondere gedrag waar ze kunnen overgaan van een vaste naar een vloeibare toestand. Het hangt er allemaal van af hoe je met ze omgaat. Deze overgang van vast naar vloeibaar wordt nog ingewikkelder op het moment dat we te maken hebben met vervormbare deeltjes in plaats van met harde deeltjes. Schuimen zijn een goed voorbeeld van een veel-deeltjes systeem van zachte, vervormbare deeltjes.

Het samendrukken van nat schuim lijkt een relatief eenvoudig proces: verzamel de schuimbellen in een container, en druk dan de wanden samen. Als we ons beperken tot een twee-dimensionaal systeem van bellen kunnen we de bellen in het systeem direct waarnemen; de ondoorzichtigheid die optreedt wanneer we kijken naar een drie-dimensionaal schuim, zoals bierschuim of scheerschuim, speelt ons dan geen parten. Om schuim te plaatsen in de “jamming” context - de overgang van een vrij-stromende naar een starre fase van een grote reeks zachte materialen - plaatsen we de schuimbelletjes tussen een zeepoplossing en een glasplaat. Op deze manier kunnen we de hoeveelheid belletjes in onze container controleren voordat we comprimeren. Onder deze omstandigheden is het vrij eenvoudig nuttige informatie over het gedrag van een schuim te verkrijgen: door te kijken naar het schuim worden veel belangrijke eigenschappen snel duidelijk. Bijvoorbeeld, onder druk zullen de belletjes vervormen en zich opnieuw ordenen.

Toch is dit ideale systeem van belletjes in een container iets heel anders dan een echt experimenteel systeem. Net als een luchtbel in water is schuim, gevan-

gen onder een glasplaat, onderhevig aan opwaartse krachten. Als de plaat niet perfect waterpas staat, drijft het schuim naar een hoek van onze container. Ook ontstaan er problemen als de temperatuur schommelt. Omdat schuimbellen uit gas bestaan, zullen zij uitzetten en krimpen, afhankelijk van de omgevingstemperatuur. De uitdaging bij het werken met schuim is dus om het systeem voldoende te controleren, om het door het jamming punt te laten gaan.

In dit proefschrift geven we een kort overzicht van de onderwerpen die worden behandeld in hoofdstuk 1. We beginnen met de invoering van jamming concepten in hoofdstuk 2 en stellen twee fundamentele vragen: wat is de aard van de “jammed” toestand, en wat is de aard van de jamming overgang? We presenteren een geïdealiseerd beeld, met behulp van een eenvoudig model. Verder benadrukken we dat materialen in een gejammede toestand zich niet als gewone, vaste stoffen gedragen. In het hoofdstuk wordt ook besproken dat het schaalgedrag van de bulk en shear moduli als functie van de afstand tot het jamming punt verschillend is. We eindigen dit hoofdstuk met een bespreking van eerder experimenteel werk, alsmede de introductie van een aantal basisbegrippen van nonaffine beweging in “jammed” systemen, die een centrale rol in de hoofdstukken 4 en 5 zullen spelen.

In hoofdstuk 3 beschrijven we een nieuw experiment, waar volledige manipulatie en controle ons in staat stelt om te meten hoe een schuim zich onder compressie gedraagt. We houden een enkele laag schuimbellen tussen de oppervlakte van een zeepoplossing en een glasplaat, in een wigvormige geometrie. Maar zelfs wanneer schuim onder een geslepen en gepolijste vlakke glazen plaat gevangen is, kunnen wij de jamming overgang niet precies bepalen, omdat de glasplaat nooit perfect horizontaal ligt. We kantelen de experimentele opstelling een beetje, en zo beïnvloeden wij de positie van de belletjes die in de wig zitten. Door het gebruik van een rheometer in strain gecontroleerde modus kunnen we het schuim subtiel comprimeren en de stress respons ervan meten. We filmen de opstelling van boven en gebruiken beeldcorrectie technieken om de opnamen bruikbaar te maken voor verdere analyse.

De reactie van het schuim op compressie wordt in hoofdstuk 4 in detail onderzocht. Ten gevolge van de kanteling van het systeem zijn er twee regimes: een regime gedomineerd door zwaartekracht en een regime gedomineerd door de zijwanden. In het zwaartekracht gedomineerde regime is er tussen het schuim en de compressie genererende wisser een kloof. Door het stapsgewijs sluiten van de kloof gaan we naar het regime waar het schuim volledig wordt begrensd door de zijwanden. Het sluiten van de kloof valt niet altijd samen met het toenemen van het torsie signaal. Door een onderscheid tussen “boundary jammed” en “gravity jammed” in te voeren, kunnen we de elastische moduli toch bepalen. In het zwaartekracht gedomineerde regime vinden we dat, hoewel het systeem nog steeds zwak “gejammed” is, het geen elastische reactie op vervorming vertoont, wat aangeeft dat de afschuifmodulus (shear) nul is. Tenslotte zien we een sterk nonaffine reactie van het schuim dicht bij het jamming punt.

In hoofdstuk 5 sluiten we een bidisperse schuimlaag tussen een zeepoplossing en een glasplaat in, maar onderwerpen het systeem aan een gecontroleerde, zuivere afschuif spanning. We sluiten het schuim in een rechthoekige container op (onder een glasplaat), waardoor het oppervlak constant blijft terwijl de wanden worden

geschoven. We filmen het systeem van boven en door het berekenen van het verschil tussen de opnamen kunnen we de bewegingen die in het systeem optreden karakteriseren. We vinden dat wanneer het schuim sterk gecompriëerd (droog schuim) is, er slechts een type herschikking is, de T1 herschikking. Deze herschikking is ruimtelijk gelokaliseerd en treedt op gedurende een relatief korte tijdsperiode. Als we de dichtheid slechts in geringe mate verlagen is de T1 herschikking niet langer de enige soort en het systeem begint nu meer globale beweging te vertonen, met vele bellen die bewegen. De tijdsperiode van de beweging neemt ook toe. Als we bij de jamming overgang aankomen, is de beweging in het systeem volledig geglobaliseerd.

Publication List

1. Clusel, M., Corwin, E.I., Siemens, A.O.N., Brujic, J., *A “granocentric” model for random packing of jammed emulsions*, Nature **460**, 611-615 (2009).
2. Corwin, E.I., Clusel, M., Siemens, A.O.N., Brujic, J., *Model for random packing of polydisperse frictionless spheres*, Soft Matter **6**, 2949-2959 (2010).
3. Siemens, A.O.N., van Hecke, M., *Jamming: A Simple Introduction*, Physica A **389**, 4255 (2010).
4. Siemens, A.O.N., van Hecke, M., *Jamming transition in a two-dimensional foam*, in preparation.
5. Siemens, A.O.N., van Hecke, M., *Rearrangements in two-dimensional foams: role of wetness*, in preparation.

Curriculum Vitae

I was born on June 20, 1985 in Washington, D.C., USA. After finishing high school at the Frankfurt International School in Frankfurt, Germany, I began my undergraduate studies at The Johns Hopkins University in Baltimore, Maryland, USA. I worked each summer in a different lab, notably on back-scattering of strongly scattering powders in the lab of Prof. Georg Maret at Universität Konstanz, Germany, and on the Edwards entropy hypothesis in the lab of Prof. Robert Behringer at Duke University, North Carolina, USA. My senior thesis, *Edwards Entropy of a Binary Mixture in Granular Materials*, was completed under the supervision of Prof. Robert Behringer and Prof. Robert Leheny and I received my B.Sc. in Physics with a minor in Mathematics in 2007.

I moved to New York City, New York, USA, to join the newly-formed research group of Prof. Jasna Brujic at New York University. I was lead experimentalist on creating polydisperse micro emulsions and analyzing them, using confocal microscopy. This research led to two research papers, notably A “*granocentric*” model for random packing of jammed emulsions in Nature Magazine.

In 2009, I began a Ph.D. project in the Granular and Disordered Media group of Prof. Martin van Hecke at Leiden University on elasticity and plasticity in disordered foams. The results of this research are collected in this Thesis. At Leiden University I worked as a teachers assistant for courses in LabVIEW and Experimental Physics. I attended conferences and presented papers in Amsterdam, Wageningen, Twente, Delft, Lisbon (Portugal), Cargese (France), Edinburgh (Scotland), Dublin (Ireland), New York, Baltimore, Dallas and Portland (USA).

Acknowledgments

This Thesis is the product of four years of work done at the Universiteit Leiden, in the Kamerlingh Onnes Laboratorium. This work could only have been completed with the help of many people. I would like to take the time to thank them here. I would like to thank Jeroen Mesman for all the set-ups and technical assistance. There is no finer craftsman. In the secretariat I have to thank Daniëlle Duijn for her good humor and for booking all my travels and filling in forms I could never attempt myself. I truly appreciate her logistical expertise. When the rheometer would break or when I needed to optimize my workbooks, Joop van den Ouweland at Anton Paar was a great help. Thank you, Brian Tighe, for being a genuine and patient person who never hesitated to take the time to walk me through the questions I had on Soft Matter. Thank you to my colleagues at the lab for all the help with my experiments and the “gezelligheid”: Gijs, Elie, Simon, Corentine, Daniel M., Bastiaan, Geert, Merlijn, Daniel G., Kiri, Erik, Siet. I gratefully remember the late Zlatko Tesanovic, my old physics mentor at Johns Hopkins. Special thanks to Daniel Miedema and Geert Wortel for being my paranimfen. Also, I would like to thank my brother and sister for never knowing what I was doing besides “foam”, which helped me keeping up-to-date with non-physics related things, my mother for listening to all my problems while doing this research and my father for talking me through many every-day life situations I encountered while writing this thesis.

Bibliography

- [1] A.J. Liu and S.R. Nagel. *Nature*, 396:21, 1998.
- [2] A. O. N. Siemens and M. van Hecke. *Physica*, 389:4255, 2010.
- [3] N. Isert, G. Maret, and C. M. Aegerter. *arXiv:1211.0473 [cond-mat.soft]*, 2012.
- [4] G. Katgert and M. van Hecke. *EPL*, 92, 2010.
- [5] G. Katgert, B. P. Tighe, M. E. Möbius, and M. van Hecke. *EPL*, 90, 2010.
- [6] G. Katgert. *Flow of Foams*. PhD thesis, Universiteit Leiden, 2008.
- [7] L. Bragg and J.F. Nye. *Proc. R. Soc. Lond. A*, 190:474, 1947.
- [8] G. Debrégeas, H. Tabuteau, and J.-M di Meglio. *Phys. Rev. Lett.*, 87:178305, 2001.
- [9] M. Fatima Vaz and M.A. Fortes. *J. Phys. Condensed Matter*, 9:8921, 1997.
- [10] C. Stanley Smith. *Metal Interfaces*, 65, 1952.
- [11] W. van Saarloos A. J. Liu, M. Wyart and S. R. Nagel. *The jamming scenario – an introduction and outlook*. Oxford University Press, Oxford, 2011.
- [12] M. van Hecke. *Journal of Physics: Condensed Matter*, 22:033101, 2010.
- [13] C. S. O’Hern, L. E. Silbert, A. J. Liu, and S. R. Nagel. *Phys. Rev. E*, 68:011306, 2003.
- [14] M. Clusel, E. I. Corwin, A. O. N. Siemens, and J. Brujić. *Nature*, 460:611–615, 2009.
- [15] X. Cheng. *Phys. Rev. E*, 81:031301, 2010.

- [16] C. F. Moukarzel. *Phys. Rev. Lett.*, 81:1634–1637, Aug 1998.
- [17] A. V. Tkachenko and T. A. Witten. *Phys. Rev. E*, 60:687–696, Jul 1999.
- [18] D.J. Durian. *Phys. Rev. Lett.*, 75:4780, 1997.
- [19] H. A. Makse, N. Gland, D. L. Johnson, and L. M. Schwartz. *Phys. Rev. Lett.*, 83:5070–5073, 1999.
- [20] W. G. Ellenbroek, E. Somfai, M. van Hecke, and W. van Saarloos. *Phys. Rev. Lett.*, 97:258001, 2006.
- [21] W.G. Ellenbroek, Z. Zeravcic, W. van Saarloos, and M. van Hecke. *EPL*, 87:34004, 2009.
- [22] W. G. Ellenbroek, M. van Hecke, and W. van Saarloos. *Phys. Rev. E*, 80:061307, 2009.
- [23] H. M. Princen. *J. Colloid Interface Sci.*, 91(1):160–175, 1983.
- [24] S.A. Khan, C.A. Schnepper, and R.C. Armstrong. *J. Rheology*, 32:69–92, 1988.
- [25] A.D. Gopal and D.J. Durian. *Phys. Rev. Lett.*, 91, 2003.
- [26] T.G. Mason, J. Bibette, and D.A. Weitz. *J. Colloid Interface Sci.*, 179:439–448, 1996.
- [27] H. M. Princen. *J. Colloid Interface Sci.*, 105(1):150–171, 1985.
- [28] H. M. Princen and A.D. Kiss. *J. Colloid Interface Sci.*, 112(2):427–437, AUG 1986.
- [29] H. M. Princen and A.D. Kiss. *J. Colloid Interface Sci.*, 128(1):176–187, MAR 1 1989.
- [30] T.G. Mason, J. Bibette, and D.A. Weitz. *Phys. Rev. L*, 75:2051–2054, 1995.
- [31] D. Weaire and S. Hutzler. *The Physics of Foams*. Clarendon Press, Oxford, 1999.
- [32] E. Pratt and M. Dennin. *Phys. Rev. E*, 67, 2003.
- [33] Y. Wang, K. Krishan, and M. Dennin. *Phil. Mag. Lett.*, 87(2):125–133, FEB 2007.
- [34] Y. Wang, K. Krishan, and M. Dennin. *Phys. Rev. E*, 74(4, Part 1), OCT 2006.
- [35] M. Dennin. *Phys. Rev. E*, 70, 2004.

- [36] D.J. Durian, D.A. Weitz, and D.J. Pine. *Science*, 252:686, 1991.
- [37] J. Lambert, I. Cantat, R. Delannay, R. Mokso, P. Cloetens, J. A. Glazier, and F. Graner. *Phys. Rev. Lett.*, 99:058304, 2007.
- [38] J. Brujić, S. F. Edwards, I. Hopkinson, and H. A. Makse. *Physica A: Statistical Mechanics and its Applications*, 327:201–212, 2003.
- [39] J. Zhou, S. Long, Q. Wang, and A.D. Dinsmore. *Science*, 312:1631, 2006.
- [40] Bolton F. and D. Weaire. *Phys. Rev. Lett.*, 65:3449, 1990.
- [41] S. Hutzler and D. Weaire. *J. Phys. Condensed Matter*, 7:L657–L662, 1995.
- [42] D. Miedema. The deformation of a foam bubble. Master’s thesis, Universiteit Leiden, The Netherlands, 2010.
- [43] K. Golemanov, N. D. Denkov, S. Tcholakova, M. Vethamuthu, and A. Lips. *Langmuir*, 24:9956–9961, 2008.
- [44] M. D. Misak. *J. Colloid and Interface Sci.*, 27:141–142, 1968.
- [45] F. P. Bretherton. *J. Fluid Mech.*, 10:166, 1961.
- [46] P. Ausillous and D. Quéré. *Europhys. Lett.*, 59:370, 2002.
- [47] N. D. Denkov, V. Subraminian, D. Gurovich, and A. Lips. *Coll. Surf. A*, 263:129, 2005.
- [48] N.D. Denkov, S. Tcholakova, K. Golemanov, V. Subramanian, and A. Lips. *Coll. Surf. A*, 282-283:329, 2006.
- [49] C. F. Schreck, T. Bertrand, C. S. O’Hern, and M. D. Shattuck. *Phys. Rev. Lett.*, 107:078301, Aug 2011.
- [50] L. R. Gómez, A. M. Turner, M. van Hecke, and V. Vitelli. *Phys. Rev. Lett.*, 108:058001, 2012.
- [51] R.-J. Slager. From elasticity to equations. Master’s thesis, Universiteit Leiden, 2009.
- [52] B. Lautrup. *Physics of Continuous Matter: Exotic and Everyday Phenomena in the Macroscopic World*. IOP Publishing Ltd, 2005.
- [53] S. Dagois-Bohy, B.P. Tighe, J. Simon, S. Henkes, and M. van Hecke. *Phys. Rev. Lett.*, 109:095703, 2012.
- [54] A.S. Argon and H.Y. Kuo. *Material Science and Engineering*, 39:101–109, 1979.
- [55] J. Lauridsen, M. Twardos, and M. Dennin. *Phys. Rev. Lett.*, 89:098303, 2002.

- [56] M.L. Falk and J.S. Langer. *Phy*, 57:7192, 1998.
- [57] S. Tewari, D. Schiemann, D. J. Durian, C. M. Knobler, S. A. Langer, and A. J. Liu. *Phys. Rev. E*, 60:4385–4396, 1999.
- [58] R.P. Feynman, R.B. Leighton, and M. Sands. *The Feynman Lectures on Physics, Vol. 2*. Addison-Wesley, 1964.
- [59] M. Dennin and C.M. Knobler. *Phys. Rev. Lett.*, 78:2485–2488, 1997.
- [60] L. Bocquet, A. Colin, and A. Ajdari. *Phys. Rev. Lett.*, 103:036001, 2009.
- [61] C. Raufaste, B. Dollet, Jiang Y. Cox, S., and Graner. *Eur. Phys. J. E*, 23:217, 2007.
- [62] Y.B. Fu and R.W. Ogden, editors. *Nonlinear Elasticity: Theory and Application*. Cambridge University Press, 2001.
- [63] D. Geelen. Rearrangements in two-dimensional foams. Master’s thesis, Universiteit Leiden, 2012.